

Atom lithography of iron

Citation for published version (APA):

Sligte, te, E. (2005). *Atom lithography of iron*. [Phd Thesis 1 (Research TU/e / Graduation TU/e), Applied Physics and Science Education]. Technische Universiteit Eindhoven. <https://doi.org/10.6100/IR590725>

DOI:

[10.6100/IR590725](https://doi.org/10.6100/IR590725)

Document status and date:

Published: 01/01/2005

Document Version:

Publisher's PDF, also known as Version of Record (includes final page, issue and volume numbers)

Please check the document version of this publication:

- A submitted manuscript is the version of the article upon submission and before peer-review. There can be important differences between the submitted version and the official published version of record. People interested in the research are advised to contact the author for the final version of the publication, or visit the DOI to the publisher's website.
- The final author version and the galley proof are versions of the publication after peer review.
- The final published version features the final layout of the paper including the volume, issue and page numbers.

[Link to publication](#)

General rights

Copyright and moral rights for the publications made accessible in the public portal are retained by the authors and/or other copyright owners and it is a condition of accessing publications that users recognise and abide by the legal requirements associated with these rights.

- Users may download and print one copy of any publication from the public portal for the purpose of private study or research.
- You may not further distribute the material or use it for any profit-making activity or commercial gain
- You may freely distribute the URL identifying the publication in the public portal.

If the publication is distributed under the terms of Article 25fa of the Dutch Copyright Act, indicated by the "Taverne" license above, please follow below link for the End User Agreement:

www.tue.nl/taverne

Take down policy

If you believe that this document breaches copyright please contact us at:

openaccess@tue.nl

providing details and we will investigate your claim.

Atom Lithography of Iron

PROEFSCHRIFT

TER VERKRIJGING VAN DE GRAAD VAN DOCTOR AAN DE
TECHNISCHE UNIVERSITEIT EINDHOVEN, OP GEZAG VAN
DE RECTOR MAGNIFICUS, PROF.DR.IR. C.J. VAN DUIJN,
VOOR EEN COMMISSIE AANGEWEEZEN DOOR HET COLLEGE
VOOR PROMOTIES IN HET OPENBAAR TE VERDEDIGEN OP
MAANDAG 9 MEI 2005 OM 16.00 UUR

DOOR

EDWIN TE SLIGTE

GEBOREN TE GOUDA

DIT PROEFSCHRIFT IS GOEDGEKEURD DOOR DE PROMOTOREN:

PROF.DR. K.A.H. VAN LEEUWEN
EN
PROF.DR. H.C.W. BEIJERINCK

Druk: Universiteitsdrukkerij Technische Universiteit Eindhoven
Ontwerp omslag: Jan-Willem Luijten

CIP-DATA LIBRARY TECHNISCHE UNIVERSITEIT EINDHOVEN

Sligte, Edwin te

Atom Lithography of Iron / door Edwin te Sligte. -
Eindhoven : Technische Universiteit Eindhoven, 2005 . - Proefschrift.
ISBN 90-386-2201-5
NUR 926

Trefw.: atomaire bundels / deeltjesoptica / lithografie / nanotechnologie /
magnetische dunne lagen / oppervlaktefysica

Subject headings: atomic beams / lithography / magnetic thin films / nan-
otechnology / particle optics / surface physics

Contents

1	Introduction	3
1	Atom lithography	4
2	Laser cooling	7
3	This thesis	8
2	The choice for iron and its consequences	11
1	Choice of element	11
2	Fe source	13
3	Samples	17
4	Corrosion protection	17
5	Conclusions	18
3	Atoms in standing waves	21
1	Theory	21
2	Numerical model	25
3	Results	28
4	Experimental apparatus	31
1	Vacuum system	31
2	Fe source	33
3	Deposition	36
4	Effusive Ag source	38
5	Optical system	39
6	Conclusion	44
5	Deposition experiments	47
1	Procedure	47
2	Fe nanolines	48
3	Magnetism of thin films	52
6	Magnetism of periodic nanostructures	55
1	Demagnetizing field	56
2	Energy of ferromagnetic nanostructures	57
3	Magnetic anisotropy model	59

CONTENTS

4	Calculated demagnetizing field	63
5	Calculated anisotropy field	66
6	Concluding remarks	71
A	Appendix	74
7	Quantum Features in Atomic Nanofabrication using Exactly Resonant Standing Waves	77
8	Barrier-limited surface diffusion in atom lithography	85
1	Introduction	85
2	Numerical model	87
3	Simulation parameters	89
4	Pollutant limited surface diffusion	90
5	ES-barrier limited surface diffusion	96
6	Conclusions	99
	Summary	101
	Samenvatting	102
	Dankwoord	103
	Curriculum Vitae	104

Chapter 1

Introduction

Optical lithography has enabled the microelectronics industry to achieve phenomenal growth and innovation rates over the past half century. The main cause for this tremendous growth rate has been the relative ease with which the technique can be applied to make ever smaller structures. At the turn of the 21st century, however, it has come close to some of its fundamental limits. The most noteworthy of these limits is the size of the features that can be manufactured, a very important characteristic in a field where smaller is often considered the definition of better.

In optical lithography, a pattern is most commonly transferred into a hard material by coating it with a light-sensitive film - known as resist - and then selectively illuminating the desired parts of the resist. This selective illumination is achieved by placing a mechanical mask - called the reticle - in the light beam. The patterned light beam is then projected on the sample. A selective chemical etchant then removes either the unexposed or the exposed areas of the resist. The exposed underlying material can then be removed in a plasma reactor, where the remaining areas of resist act as an etch mask. After removing the remainder of the film, the patterned layer remains. This technique can create arbitrary shapes, but with sizes limited roughly to the wavelength of the light used to illuminate the mask film. The current industry standard is 193 nm light; the attainable feature size is around 70 nm [1]. The industry road-map projects a shift to 14 nm extreme UV light in the next ten years [2].

In atom lithography, on the other hand, light and matter change places. Now, a spatial distribution of nearly-resonant light (called a light mask) modifies the profile of a matter flux (in practice, an atomic beam). The atoms in the beam can then either react with a suitable masking layer on a surface, developing it, or be deposited directly onto the surface. The first case directly parallels conventional lithography; the latter, called direct write atom lithography, has no equivalent in optical lithography. It is a simple, one-step nanostructuring process, in which the diffraction limit hardly plays a role due to the small De Broglie wavelength of the atoms. Furthermore, the process can be combined with the deposition of a second material, resulting in a material with a structured doping on the nanoscale.

As optical lithography was used to create ever smaller ferromagnetic nanostructures, a fascinating physical properties came to light, such as quantized spin wave

INTRODUCTION

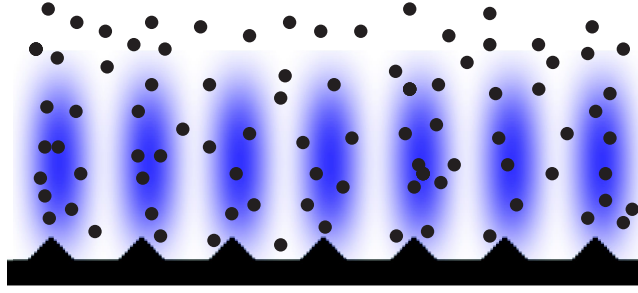


Figure 1.1: Principle of atom lithography. Atoms are focused by the induced dipole interaction with a standing wave. We intend to use this scheme to create arrays of 1D or 0D ferromagnetic nanostructures.

spectra [3]. Atom lithography offers the possibility to create structures on the order of 20 nm wide, with periods below 100 nm. Hence, the focus of this thesis is on the application of direct write atom lithography to create ferromagnetic nanostructures.

1 Atom lithography

Atom lithography is usually practiced by focusing of atoms in the periodic potential created by a standing laser light wave, as depicted in Fig. 1.1. Atoms exposed to a light field experience a dipole force as a result of the electric field of the standing wave. This results in a sinusoidal potential. The atoms are drawn towards the potential minima; by placing a substrate in or behind the standing wave, one obtains an array of nanolines. The following will be a simplified description of the principle underlying the interaction of atoms and light masks. A more detailed description of some of the physics of the atom-standing wave interaction will be given in Chapters 3 and 7.

1.1 Principle

The interaction of an atom with a light mask may in some cases be understood classically. An electric field will induce a dipole moment in an atom. This dipole moment will interact with the electric field it is in. The energy of this interaction is:

$$U_{dip} = -\vec{p} \cdot \vec{E}, \quad (1.1)$$

where \vec{p} is the induced dipole moment and \vec{E} is the applied field. For moderate values of $|\vec{E}|$, the induced dipole moment is linear with respect to the applied field. For an electric field that is caused by laser radiation, the potential may thus be written in terms of the intensity I :

$$U_{dip} = -\alpha \vec{E} \cdot \vec{E} = -\frac{2\alpha}{\epsilon_0 c} I. \quad (1.2)$$

Usually, the polarizability α of the atoms is very small, and the effect is negligible. However, near an atomic resonance, its value increases by orders of magnitude. Hence, we use nearly resonant laser light to control the atoms.

The simplest form of light mask conceivable is a one-dimensional standing wave. In a Gaussian standing wave of beam radius w , the intensity profile $I(\vec{r})$ is given by:

$$I(\vec{r}) = \frac{8P}{\pi w^2} \sin^2(kx) \exp\left[-\frac{2(y^2 + z^2)}{w^2}\right]. \quad (1.3)$$

Here the wave propagates in the x direction with wave number k . The sign of the potential is determined by the sign of the polarizability α . For an excitation frequency below the resonance frequency, the induced dipole will be in phase with the field and $\alpha > 0$. This means that the atoms will be drawn towards the areas of maximum intensity. Conversely, they will be pushed away from the intensity maxima for light at higher frequencies than the atomic resonance.

For an exactly resonant light mask, the induced dipole moment will be phase shifted by $\pi/2$ with respect to the electric field. Hence, its interaction energy with the field will be zero. At this point, the classical description fails; quantum mechanics predicts a rich interaction. The atom flux distribution is affected by all properties of the standing wave. Chapter 7 presents an in-depth study of these phenomena.

1.2 Aberrations

Figure 1.2 displays the intensity profile of a standing wave (left) and the resulting potential landscape (center) for the case of positive detuning. Around the potential minima, a parabolic approximation can be made (shown in the Figure as the dashed line). In this region, the potential is that of a harmonic oscillator, in which the period of an oscillation is independent of its amplitude. Atoms that start in a stationary state will all converge on the potential minimum after a quarter oscillation time. This focusing effect means that the standing wave acts as an infinite array of lenses. The interaction of an atom beam with this lens array can be considered very similarly to the classical focusing of a light beam using a normal lens array. An even more accurate analogy in classical optics is an array of Gradient Index (GrIn) lenses.

The errors in the focusing can also be considered similarly to classical optical aberrations. Foremost, the size of a projected image scales linearly with the size of the original [5]. In atom optical terms, the largest contribution to the feature size results from the finite (x, p_x) phase space area of the atom beam source. Laser cooling is commonly used to reduce this error by non-conservative beam collimation. Other significant errors in classical optics include chromatic aberration, and spherical aberration.

In conventional optics, the chromatic aberration is caused by a wavelength dependence of the refractive index of the lens. The resulting variation of focus length with wavelength causes part of a non-monochromatic light beam to be out of focus, leading to a blurred image. The wavelength of light is directly related to the momentum of the photons that comprise it. Thus, the analogy of the spread in wavelength of a non-monochromatic light source is the spread in longitudinal velocity of an

INTRODUCTION

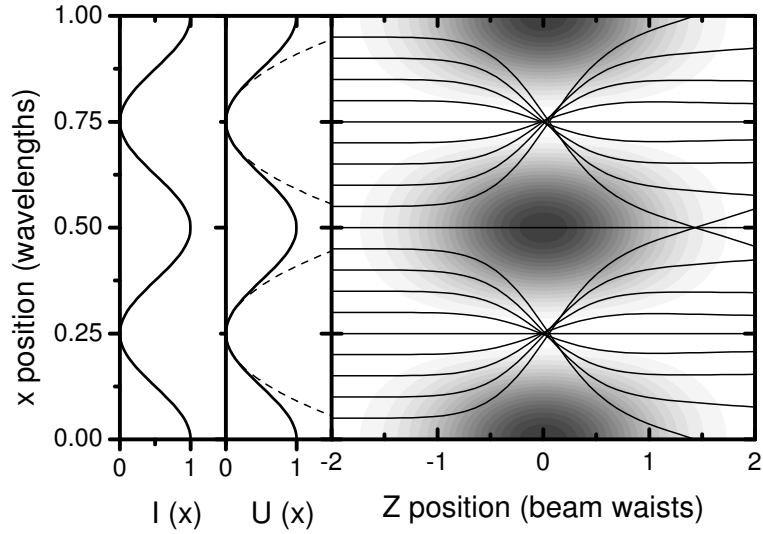


Figure 1.2: Simulated trajectories (lines) of atoms focused by a standing light wave (color represents intensity). Frequency of the light is above that of the atomic resonance. Top: intensity profile of a standing light wave. Bottom: resulting potential landscape. Around the nodes and antinodes, a parabolic approximation may describe the potential.

atom beam. The chromatic aberrations in atom optics result from the finite width of the longitudinal velocity distribution of the atom beam. This may be resolved by using a supersonic atom source, which reduces the longitudinal velocity spread of the atoms, and thus the chromatic aberrations in atom focusing.

Ordinary lenses are machined to be spherical, and the difference between the spherical lens contour and the ideal Cartesian shape gives rise to spherical aberrations. The sinusoidal potential landscape generated by the standing wave also gives rise to such aberrations. In Fig. 1.2, these can be seen by the small, but finite, spread in the trajectories at the focus. These sinusoidal aberrations may be resolved by using more ingenious light masks, or suppressed by using mechanical masks to block off the anharmonic parts of the lens.

Finally, when focusing a parallel light beam with a conventional lens, the focused beam comprises a certain range of angles. The sine of the largest angle in the range is referred to as the numerical aperture. For an atom lens, the numerical aperture is usually very small, as the size of the lens is that of a single potential minimum. The focus length of the lens is typically of the order of the beam waist w . Thus, the numerical aperture of the atom lens array can be estimated by $NA \approx \lambda/4w$. Typically, this is of the order 10^{-3} . Conventional lenses can have numerical apertures of more than one. For atom lithography, it means that the diffraction limit on feature size increases by a factor 10^3 from the de Broglie wavelength of the atom to several nanometers.

As in conventional optics, the amount of hindrance resulting from chromatic and sinusoidal aberrations depends on the accuracy required of the imaging system. There is still one source of resolution loss left in direct-write atom lithography -

surface diffusion. After the atoms have been deposited in the correct place by the light mask, they may still move around on the surface. The effects of this motion have been observed in atom lithography experiments [4], and Chapter 8 provides an in-depth study of this phenomenon.

1.3 Experiments

The first experiments in atom lithography were of the direct-write type, and date from the early 1990's. Timp *et al.* deposited a periodic grid of Na lines onto a Si substrate and investigated it *in situ* using an AFM [6]. Soon after, the first experiments using Cr were performed [7]. These produced the first structures that survived exposure to atmosphere. Around the same time, the first experiments using metastable argon atoms to expose a self-assembled monolayer were performed at NIST [8]. Since then, the technique has been applied to Al [9], Yb [10] (direct write), metastable He [11] and Ne [12], and Cs [13] (expose-and-develop). For the electric dipole forces to be sufficiently strong, light with a frequency close to an atomic resonance must be used. The range of materials to which atom lithography can be applied is limited mainly by the availability of lasers at suitable wavelengths. This especially holds if laser cooling is to be applied to collimate the beam.

There has also been considerable development in the light masks used. The initial experiments all used the simple one-dimensional standing wave. Since then, two-dimensional nanostructure grids have also been made, both square [14] and hexagonal [11]. In addition, the technique has been applied to holographic light masks [15], demonstrating its applicability to create arbitrary structures. Finally, its unique capacity for creating a spatially structured doping at large scale and low cost has been demonstrated [16]. The aim of this thesis is to demonstrate the extension of the technique to ferromagnetic materials.

2 Laser cooling

The phase space area of an atom beam can be reduced by two techniques: placing narrow slits in the beam, or laser cooling the atom beam. The disadvantage of using slits is the inherent loss of atom flux. Laser cooling, however, is a dissipative atom optical technique, which may drastically increase the intensity of an atom beam. The description given here is rudimentary; more information can be found in [17].

A two-level atom that is irradiated by a collimated laser beam will absorb and spontaneously re-emit photons from that laser beam. The momentum of the photons in the laser beam is $\vec{p} = \hbar\vec{k}$. On absorbing a photon, the recoil changes the atom's momentum by $\hbar\vec{k}$. As the spontaneously emitted photons have a symmetrical directional distribution, their average momentum is zero. This means that the atom's momentum will change by, on average, $\hbar\vec{k}$ per scattered photon. In other words, the laser beam exercises a force on the atom of $\langle \vec{F} \rangle = \dot{N}\hbar\vec{k}$ if the atom scatters photons at rate \dot{N} .

INTRODUCTION

The photon scattering rate of a stationary atom is determined by the line width Γ and saturation intensity I_s of the resonance and the detuning Δ and intensity I of the laser:

$$\dot{N} = \frac{\Gamma}{2} \frac{I/I_s}{1 + I/I_s + (2\Delta/\Gamma)^2} \quad (1.4)$$

If we apply two counterpropagating laser beams to a stationary atom, the forces caused by the two laser beams are equal but oppositely directed and therefore cancel.

For an atom moving with velocity \vec{v} , the Doppler shift must be taken into account by using an effective detuning $\Delta - \vec{k} \cdot \vec{v}$. If we apply two counter-propagating red-detuned ($\Delta < 0$) laser beams to a slowly moving atom ($|\vec{k} \cdot \vec{v}| < |\Delta|$), the magnitude of the two radiation forces is no longer the same. An atom moving in the reverse direction of a laser beam detuned to the red will experience a frequency that is apparently closer to resonance, and therefore scatter more photons. The frequency of the other laser beam will appear further from resonance. The atom will thus scatter fewer photons from the copropagating laser beam. The two contributions to the resulting force no longer cancel, and a net force arises that opposes the motion of the atom, regardless of its direction. Therefore, the atom's velocity component along \vec{k} is reduced.

Due to the momentum diffusion caused by the random 'kicks' that an atom receives during the cooling, the velocity distribution of the atoms will retain a finite width. The width of a velocity distribution in dimension i can be related to a temperature by: $\frac{1}{2}k_B T_i = \frac{1}{2}m\langle v_i^2 \rangle$. Thermodynamically, this temperature is determined by an equilibrium between recoil heating and laser cooling. It can be calculated analytically for low laser intensities to equal [17]:

$$T_D = \frac{\hbar\Gamma}{2k_B}, \quad (1.5)$$

also known as the Doppler temperature.

Due to its dissipative nature, laser cooling can reduce the divergence of an atom beam when applied in the direction perpendicular to the atom beam. The process occurs without reducing the atom beam flux, resulting in a net intensity gain. It also selects atoms of one particular isotope and in one particular state. Hence, it is common practice to use laser cooling to collimate the atomic beam before applying the light mask to it.

For the radiation forces to have any significant effect, many photons must be scattered by the atom. This means that the atom must return to the ground state of the transition after every decay. This requirement severely limits the number of elements to which laser cooling can be applied.

3 This thesis

The first part of the remainder of this thesis will describe the atom lithography experiment in Eindhoven; the second part will describe the results and analysis of experiments done elsewhere.

THIS THESIS

We begin by choosing an element to apply atom lithography to in Chapter 2. This choice will have far-reaching consequences for many aspects of the experiment, which will also be discussed.

Chapter 3 will describe a more rigorous theory of the atom-light interaction. Also, it will describe the numerical model used to understand the experiments done in this thesis.

We proceed to describe the Eindhoven atom lithography experiment in Chapter 4. A reliable setup for generating and laser cooling an Fe atom beam was constructed. The light mask and deposition setup are described in detail. Also, an effusive metal beam source for a capping layer, and a sample storage chamber are characterized.

The nanostructures produced with this setup are characterized in Chapter 5. We begin by describing the deposition procedure, and continue by describing the topological analysis of the nanostructures using an Atomic Force Microscope. We conclude by a comparison between the expected and observed features of the deposition process.

First steps of theoretical research into the magnetic properties of these nanostructures are presented in Chapter 6. We survey some of their interesting magnetic features. Some considerations on the shape anisotropy of the nanostructures are presented.

Chapter 7 describes an atom lithography experiment done at the University of Konstanz [18]. We present a study of the effects of an exactly resonant light mask on the atomic focusing. It was found that this light mask could produce structures with a period of $\lambda/4$, a factor 2 improvement over the $\lambda/2$ period achieved using off-resonant light masks. The author of this thesis contributed mainly to the theoretical part of this work; a more extensive report may be found in the PhD thesis of Jürgens [19].

In Chapter 8, we describe an analysis of the effect of surface diffusion after deposition on the width and resolution of Cr nanostructures. Starting from literature, we numerically investigate surface diffusion, and several diffusion-blocking mechanisms. One of the effects we consider has been investigated independently at around the same time [20]; their findings are largely similar to ours. We obtained better results using a second hypothesis, and show that small amounts of pollutants can have large effects on the surface diffusion of newly-deposited atoms, and that the vacuum conditions during deposition may be essential for the feature sizes that can be achieved.

References

- [1] Specifications for ASML TWINSCAN XT:1250i
- [2] P. J. Silverman, Intel Technology Journal **6**, 55-61 (2002)
- [3] Z. K. Wang, M. H. Kuok, S. C. Ng, D. J. Lockwood, M. G. Cottam, K. Nielsch, R. B. Wehrspohn, and U. Gsele, Phys. Rev. Lett. **89**, 027201 (2002)

INTRODUCTION

- [4] W. R. Anderson, C. C. Bradley, J. J. McClelland, and R. J. Celotta, *Phys. Rev. A* **59**, 2476-2485 (1999)
- [5] F. L. Pedrotti and L. S. Pedrotti, *Introduction to Optics*, Prentice-Hall (1987)
- [6] G. Timp, R. E. Behringer, D. M. Tennant, J. E. Cunningham, M. Prentiss, and K. K. Berggren, *Phys. Rev. Lett.* **69**, 1636-1639 (1992)
- [7] J. J. McClelland, R. E. Scholten, E. C. Palm, and R. J. Celotta, *Science* **262**, 877-880 (1993)
- [8] K. K. Berggren, A. Bard, J. L. Wilbur, J. D. Gillaspay, A. G. Helg, J. J. McClelland, S. L. Rolston, W. D. Phillips, M. Prentiss, and G. M. Whitesides, *Science* **269**, 1255-1257 (1995)
- [9] R. W. McGowan, D. Giltner, and S. A. Lee, *Opt. Lett.* **20**, 2535-2537 (1995)
- [10] R. Ohmukai, S. Urabe, and M. Watanabe, *Appl. Phys.* **B 77**, 415-419 (2003)
- [11] B. Brezger, Th. Schulze, U. Drodofsky, J. Stuhler, S. Nowak, T. Pfau, and J. Mlynek, *J. Vac. Sci. Technol.* **B 15**, 2905-2911 (1997)
- [12] P. Engels, S. Salewski, H. Levsen, K. Sengstock, and W. Ertmer, *Appl. Phys.* **B 69**, 407 (1999)
- [13] F. Lison, H. J. Adams, P. Schuh, D. Haubrich, and D. Meschede, *Appl. Phys.* **B 65**, 419 (1997)
- [14] R. Gupta, J. J. McClelland, Z. J. Jabbour, and R. J. Celotta, *Appl. Phys. Lett.* **67**, 1378-1380 (1995)
- [15] M. Mützel, S. Tandler, D. Haubrich, D. Meschede, K. Peithmann, M. Flaspöhler, and K. Buse, *Phys. Rev. Lett.* **88**, 083601 (2002)
- [16] Th. Schulze, T. Müther, D. Jürgens, B. Brezger, M. K. Oberthaler, T. Pfau, and J. Mlynek, *Appl. Phys. Lett.* **78**, 1781-1783 (2001)
- [17] H. Metcalf and P. van der Straten, *Laser Cooling and Trapping*, Springer Verlag, Heidelberg (1999)
- [18] D. Jürgens, A. Greiner, R. Stütze, A. Habenicht, E. te Sligte, and M. K. Oberthaler, *Phys. Rev. Lett.* **93**, 237402 (2004)
- [19] D. Jürgens, PhD thesis, University of Konstanz (2004)
- [20] J. Zhong, J. C. Wells, and Y. Braiman, *J. Vac. Sci. Technol.* **B 20**, 2758-2762 (2002)

Chapter 2

The choice for iron and its consequences

This chapter will motivate the choice for the Fe atom for our atom lithography experiment. As this choice has far-reaching consequences for almost every aspect of the experiment, we will also describe the problems involved.

1 Choice of element

Ferromagnetic nanostructures can only be made from a single atomic species if a ferromagnetic element is used. The only elements that are consistently ferromagnetic at room temperature are iron, nickel, and cobalt.

Table I shows the relevant properties of the three ferromagnetic transition metals. Investigating the magnetic properties, we find that the magnetization of Ni is clearly smaller than that of the other two elements. Experiments investigating these magnetic nanostructures could suffer from this smaller magnetization. Hence, we prefer to use another element.

Looking at the atom optical properties of the candidate materials, we find that the all candidates have a dominant isotope with an abundance of at least 68 %. This implies that the majority of the atomic beam can be addressed by laser manipulation with a single laser.

However, the atom optical properties of Co are disastrous. The wavelength of its only transition suitable for laser cooling is deep in the UV, in a region that is only accessible with the use of *two* frequency doubling stages, or doubling a blue dye laser. In addition, laser cooling results in a very broad velocity distribution due to the large natural line width. And worst, it would require many repumping laser systems. The nuclear spin of the only stable isotope, ^{59}Co , is $7/2$, generating an complicated hyperfine spectrum that contains no less than eighty Zeeman states.

The other candidates Fe and Ni are better, though they still present problems. In the case of Ni, these are mainly inconveniences. Light at the wavelength of Ni can only be made in sufficient amounts by frequency doubling a dye laser. The dye laser

THE CHOICE FOR IRON AND ITS CONSEQUENCES

would then be required to have a frequency stability and line width of better than 500 kHz to stay within one natural line width.

The Fe atom presents a more fundamental problem, namely, the fact that it does *not* have a closed transition from the ground state. The 5F_5 excited state can decay to three intermediate states. These states have lifetimes of many milliseconds, which is effectively infinite in an atom lithography experiment. The Doppler temperature of Fe is 62 μ K, corresponding to a velocity spread of 96 mm/s. Simulations [1] of laser cooling using this leaky transition show that a suitably narrow-band laser system would be able to achieve a collimation close to this value.

In conclusion, we find that Fe is the most promising magnetic candidate material for atom lithography. Atom lithography is virtually impossible using Co. The choice between Fe and Ni is motivated mainly by the greater saturation magnetization and isotopic purity of Fe. The more cumbersome laser system that would be needed for Ni should be weighed against the complication of laser cooling with a leaky transition.

Table I: Properties of the ferromagnetic elements Fe, Co and Ni.

	Fe	Co	Ni
magnetic properties			
atomic magn. moment (μ_B)	4	3	2
bulk magn. moment (μ_B)	2.2	1.7	0.6
bulk phase crystal structure	bcc	hcp	fcc
magnetization $\mu_0 M_s$ (T)	2.16	1.72	0.61
Curie temperature (K)	1044	1393	628
isotopes			
Z	26	27	28
most abundant	${}^{56}\text{Fe}$ 92%	${}^{59}\text{Co}$ 100%	${}^{58}\text{Ni}$ 68%
other isotopes	${}^{54}\text{Fe}$ 6% ${}^{57}\text{Fe}$ 2%		${}^{60}\text{Ni}$ 26% ${}^{62}\text{Ni}$ 4% ${}^{61}\text{Ni}$ 1% ${}^{64}\text{Ni}$ 1%
atomic properties			
electron conf.	$3d^6 4s^2$	$3d^7 4s^2$	$3d^8 4s^2$
ground state conf.	5D_4	${}^4F_{9/2}$	3F_4
ground state J	4	9/2	4
nuclear spin I	0 (${}^{56}\text{Fe}$)	7/2 (${}^{59}\text{Co}$)	0 (${}^{58}\text{Ni}$)
ground state pop. @ 2000 K	50%	12%	70%
atomic transitions from ground state			
transition	${}^5D_4 \rightarrow {}^5F_5$	${}^4F_{9/2} \rightarrow {}^4G_{11/2}$	${}^3F_4 \rightarrow {}^3G_5$
wavelength (nm)	372.0	240.5	323.4
Γ upper state (MHz)	2.58	57.3	1.16
saturation intens. I_s (W/m^2)	62	5156	43
leak rate	1:243	0	0

FE SOURCE

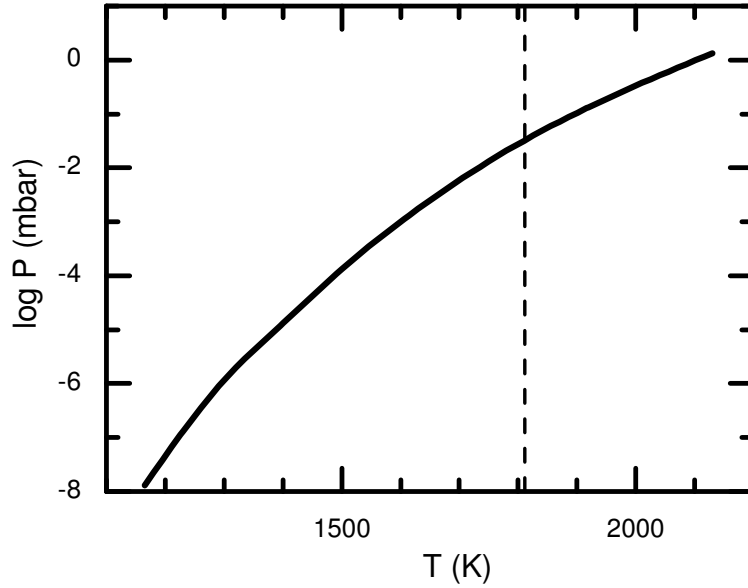


Figure 2.1: Vapor pressure of Fe. Data from Ref. [10]. Vertical line indicates melting point (1811 K).

2 Fe source

We need a source of iron atoms that will generate a sufficient flux of ground state Fe atoms. Therefore, we must heat Fe to a temperature at which its vapor pressure is sufficient for our demands. Figure 2.1 shows the vapor pressure of Fe as a function of temperature.

Ideally, we aim for a supersonic beam source to minimize the longitudinal velocity spread of the Fe beam. For an expansion to become supersonic at zero background pressure, the Knudsen number in the orifice must be much smaller than one. The Knudsen number Kn is defined as the mean free path λ divided by the orifice diameter d :

$$\text{Kn} \equiv \frac{\lambda}{d} = \frac{1}{n\sqrt{2}\sigma d}. \quad (2.1)$$

The collision cross-section for Fe-Fe collisions is estimated at $\sigma = 0.5 \text{ nm}^2$, and the atom density n can be derived from the ideal gas law. Around 2000 K, Kn is one for a vapor pressure of 0.4 mbar. Although this temperature and pressure might be feasible, a properly supersonic expansion would require a much higher pressure, which is impossible to achieve by Fe vapor pressure alone.

This consideration led us to investigate the possibility of a *seeded* supersonic expansion [2]. Letting the iron vapor mix with a high-pressure inert gas that subsequently undergoes a supersonic expansion means that the velocity distribution of the Fe will become similar to that of the Ar [3]. The other option is using an effusive Fe source.

THE CHOICE FOR IRON AND ITS CONSEQUENCES

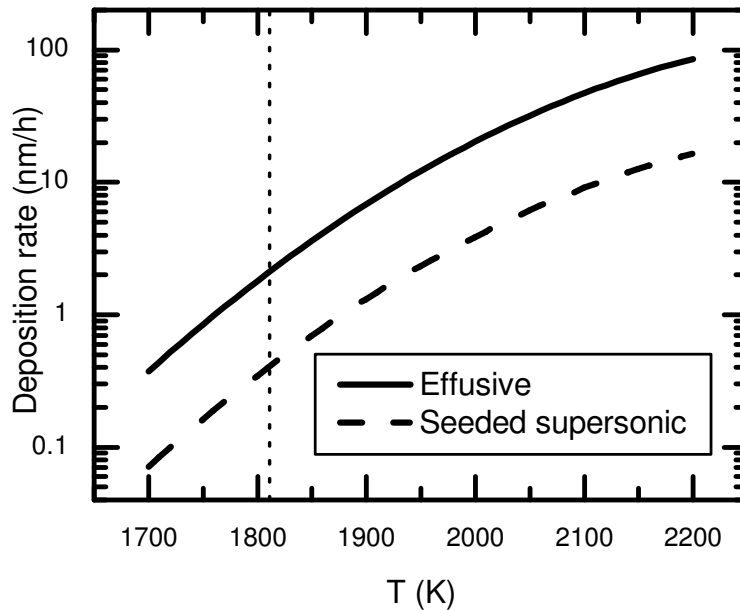


Figure 2.2: Fe deposition rate vs. temperature for effusive (drawn line) and seeded supersonic (dashed line) sources. Dashed vertical line indicates melting point of Fe.

2.1 Reactivity

Iron is a highly reactive material at the temperatures under consideration here. This must be taken into account when selecting materials for the crucible that the Fe vapor will expand from.

Materials that are capable of withstanding high temperatures and are easily machined are graphite and boron nitride (BN). Unfortunately, iron will readily react with graphite to form iron carbide (Fe_3C), effectively disqualifying it as a crucible material. At temperatures above 2000 K, iron also reacts with BN, forming iron boride and releasing large quantities of nitrogen into the vacuum system.

A suitable material that does not react with iron at any temperature is highly purified alumina (Al_2O_3). This will resist corrosion by iron until it begins to melt and dissociate at 2200 K. A downside to alumina is the difficulty of machining it. We accept this hindrance, and use alumina to make our crucibles.

Looking for a reliable supersonic source design, we copied the basic design of Hagen [4]. This design featured a graphite heating spiral and crucible. As mentioned before, we replaced the graphite crucible by one made of alumina. Unfortunately, the combination of alumina and graphite also proved to be reactive at high temperature. The reaction produced a gas that was detected in the vacuum system as a sudden increase in vacuum background pressure above a certain temperature. The reaction that occurs here is possibly dissociation of the alumina, followed by the oxygen reacting with graphite to give CO_x . This reaction may have been mediated by the Fe vapor in the source oven.

2.2 Crucible design

As the Fe is liquid at typical operating temperatures, it is free to move through the crucible. This problem does not occur for Cr. As the droplet usually lies on a horizontal surface, it will generally not flow, but it may creep. This creep is apparently induced by temperature gradients, and was found always to go in the direction of lowest temperature.

We performed experiments using two different alumina crucible designs. The top design in Fig. 2.3 is that of the supersonic crucible that was also used in Ref. [3]. The crucible consists of two concentric tubes, and is open at the rear, where the Ar gas inlet is. The supersonic expansion occurs through a small nozzle at the right of the crucible. Backward creep of the Fe was halted by the Ar flow through the crucible. This balance of forces proved to be quite unstable, and we observed frequent clogging of the nozzle by an Fe droplet. The only way to clear the nozzle was to increase the Ar pressure at high temperature until the Fe droplet was expelled from the Fe source.

The supersonic source can be switched to thermal operation simply by shutting down the Ar flow. However, this only works briefly, as the iron droplet in the crucible will creep away from the point of highest temperature. The resulting creep was usually towards the Ar inlet, resulting in a dramatic flux loss as it progressed until the Fe solidifies at 1811 K [5].

In an effort to create a more stable effusive source, we tested the crucible design at the bottom of Fig. 2.3. With a special nook-and-rim around the orifice insert (indicated in the Figure), it was far less sensitive to clogging. Additionally, the orifice was protected against clogging by placing the crucible further inside the oven, where the temperature is more uniform and higher. This design is closed at one end, halting the backward creep of the Fe droplet at a relatively high temperature. It proved unstable, as the Fe crept into the bottom left corner of the crucible. During heating and cooling of the source, the thermal stresses at this point proved to be too great for the alumina, and the crucible broke. After this trial-and-error learning, we chose to operate the effusive Fe source in a supersonic crucible with an enlarged nozzle.

2.3 Source mode

For a seeded supersonic expansion of Fe in Ar, the atomic Fe beam flux \dot{N}_{ss} (expressed in atoms/s) through a nozzle of area A is given by [6]:

$$\dot{N}_{ss} = 0.455 n_0 \langle v_{Ar} \rangle A, \quad (2.2)$$

where n_0 is the density of Fe atoms in the crucible and $\langle v_{Ar} \rangle$ is the mean thermal velocity of the Ar atoms in the crucible. The center line intensity I_{ss} of the expansion is given (in atoms/s/sr) by:

$$I_{ss} = \frac{2.08}{\pi} \dot{N}_{ss}. \quad (2.3)$$

THE CHOICE FOR IRON AND ITS CONSEQUENCES

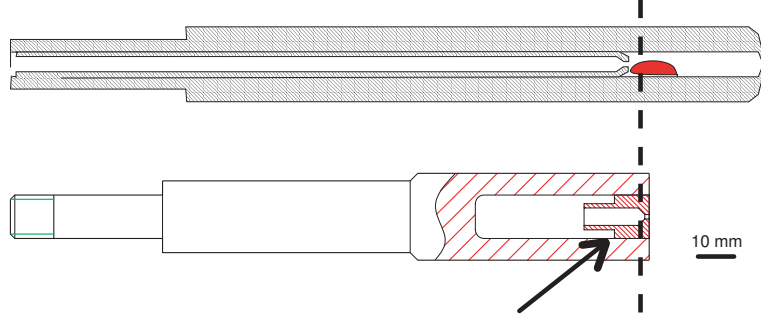


Figure 2.3: Seeded supersonic mode crucible (top) and effusive mode crucible (bottom). Dashed line indicates position of temperature maximum. Arrow points to anti-clogging rim around orifice.

Expressed in terms of the properties of the Fe atoms in the crucible for comparison with an effusive source, this expression reads:

$$I_{ss} = \frac{4.31}{4\pi} n_0 \langle v_{Fe} \rangle A. \quad (2.4)$$

Here, $\langle v_{Fe} \rangle = \sqrt{8kT/\pi m_{Fe}}$ is the mean thermal velocity of the Fe atoms in the crucible. To achieve a satisfactory velocity distribution ($\sigma_v/\langle v \rangle < 0.1$), the expansion must to operate at an Ar pressure over 100 mbar. Such an expansion imposes a huge gas load on the vacuum system; we found that it was necessary to limit the nozzle diameter to 0.23 mm. The calculated deposition rate at a sample located 0.6 m from the nozzle from such a source is shown in Fig. 2.2 (dashed line). The velocity spread $\sigma_v/\langle v \rangle$ is typically around 0.07 for this supersonic expansion [3].

The Fe flux from the orifice of an effusive source can be estimated by assuming that the Fe vapor inside the crucible is in thermal equilibrium. The total atom flux \dot{N}_{th} is given by:

$$\dot{N}_{th} = \frac{1}{4} n_0 \langle v_{Fe} \rangle A. \quad (2.5)$$

The intensity of the thermal beam I_{th} is then given by:

$$I_{th} = \frac{1}{\pi} \dot{N}_{th} = \frac{1}{4\pi} n_0 \langle v_{Fe} \rangle A. \quad (2.6)$$

The non-supersonic expansion of the Fe in the vacuum system has two effects. First, the difference between a supersonic expansion and effusive flow results a factor 4.31 flux loss. However, the orifice diameter can be increased to 1 mm, as determined by the acceptance of the rest of the setup. This leads to a factor 20 gain in flux. The net effect is that the thermal effusive source yields 4.5 times more flux than the seeded supersonic source. A theoretical calculation of this flux at 0.6 m from the nozzle is shown in Fig. 2.2 (drawn line). For a purely effusive source, the longitudinal velocity distribution is of the shape:

$$P(v/\alpha) = 2 * (v/\alpha)^3 \exp -(v/\alpha)^2, \quad (2.7)$$

SAMPLES

$\alpha = \sqrt{2kT/m}$ being the most probable velocity of the Fe atoms in the source. This distribution yields a velocity spread $\sigma_v/\langle v \rangle = 0.36$, a factor five more than the supersonic source.

It is clear that the supersonic source works well to suppress the longitudinal velocity spread of the Fe beam. However, the seeded supersonic expansion places a tremendous gas load on the vacuum system. In the source chamber, a 50 l/s roots blower had to be used instead of a turbomolecular pump, meaning far higher background pressures and much more contamination throughout the entire vacuum system. We conclude that the loss of beam intensity, the difficulty of making the supersonic source function reliably, and the tremendous gas load on the vacuum system clearly outweigh the benefits of the supersonic velocity distribution. For the remainder of this thesis, we will work with the effusive source exclusively.

3 Samples

For the experiments described in this thesis, the sample was simply a piece of Si[100] wafer, with the native oxide layer still intact. However, for better study of the substrate dependence of the deposition experiments, we have also included the option of using monocrystalline samples. The crystals to be used are W[110] crystals, as these were shown to have a high activation energy for surface diffusion of atomic Fe [7].

The $4 \times 4 \times 1$ mm samples were prepared in the MMN group of Janssen by annealing a monocrystalline piece of W in an oxygen environment at 1600 °C for five hours [8]. After cutting and polishing, the samples were ready for use. A quick isotropic NaOH electrolytic etch was used to remove any metallic and organic residues on the sample, and the clean sample was placed into the vacuum system. A final cleaning stage takes place *in vacuo*, by annealing at 500 °C for several minutes. This treatment ensures a clean W surface, ready for deposition [8].

For the annealing phase, an electron gun was used that was integrated into the sample assembly. In the sample holder, the sample rests on a Macor slab that serves was used to electrically isolate the W sample from the rest of the vacuum system. A ~ 1 kV bias voltage can thus be applied to the sample to extract an electron current of up to several mA from a nearby W filament. This current can heat the sample up to 500 °C.

4 Corrosion protection

As the deposition setup does not include the possibility of *in situ* sample diagnostics, we need to remove the samples from the vacuum system. Once outside, the iron we have deposited will rapidly corrode. As the corrosion product - most likely rust (Fe_2O_3) - is not ferromagnetic, this is highly undesirable. We protect the magnetic nanostructures by covering them with a capping layer. This layer seals the nanostructures from the atmosphere, preventing oxidation and preserving their magnetic

THE CHOICE FOR IRON AND ITS CONSEQUENCES

Element	T(°C)	Surface energy (mJ/m ²)	Alloys with Fe
Ag	832	1205	none
Al	972	1140	FeAl ₃ , Fe ₂ Al
Au	1132	1410	Au ₃ Fe
Cu	1027	1520	none
Fe	1227	2000	-
Pb	547	560	none
Zn	247	868	Fe ₅ Zn ₂₁ , FeZn ₁₃

Table II: Relevant properties of several candidate capping materials. The temperatures listed are the temperatures at which the materials have vapor pressures of 10^{-4} mbar [10]. Surface energies from Ref. [11]

properties. The capping material has to meet several demands.

The first demand is that the material must be suitable for *in vacuo* deposition. This means that all of its components must have equal vapor pressure. This demand can be effectively met by restricting the materials search to pure elements. As an issue of experimental comfort, we will prefer elements that have sufficient vapor pressure at a moderate temperature. Assuming a sample located 100 mm away from a thermal effusive source with a 2 mm diameter nozzle, a quick estimate (Eq. 2.6) yields a $\sim 10^{-2}$ ML/s flux for vapor pressures around 10^{-4} mbar. Also, the material must preferably be a solid with negligible vapor pressure at room temperature. For obvious reasons, we prefer non-toxic elements.

Secondly, the capping layer must have a lower surface energy than the iron it is to cover. Adatoms with higher surface energy than iron will tend to burrow into the iron or form islands rather than cover it.

A last requirement of the material is that it must form a stable, sharply defined layer on top of the iron. The nature of the interface between iron and capping layer depends on thermodynamic as well as kinetic aspects [9]. This complicated interplay is impossible to judge at a glance. However, an indication of clean segregation can be found in the possibility of alloying the element with iron. We therefore prefer elements that do not alloy easily with iron. A stable layer also means one that does not corrode.

Table II shows the required source temperature, the surface energy and the alloying properties [12] of the more likely capping materials. Of these materials, silver is the non-toxic, non-alloying material that can be handled most easily. We thus choose Ag to use for corrosion protection of the Fe nanostructures.

5 Conclusions

Out of the three ferromagnetic elements, Fe is the most promising. Atom lithography with Ni is also possible, but would be more difficult and, most likely, less rewarding. Cobalt is totally unsuitable for any atom atom optical manipulation due mainly to

CONCLUSIONS

its complex hyperfine structure.

Constructing a source for an intense Fe beam is a very difficult task, especially if the beam line is to be aligned horizontally. However, it is possible. Using a seeded supersonic beam to reduce the longitudinal velocity spread of the Fe beam is also possible, but only at the expense of Fe flux and source reliability.

Taking an interest in nanostructure broadening through surface diffusion, we have the option of using W [110] samples for substrates.

As the Fe nanostructures need to be protected from corrosion, a capping layer must be applied *in situ*. A suitable material for this capping layer is Ag.

References

- [1] B. Smeets, R. W. Herfst, P. van der Straten, E. te Sligte, H. C. W. Beijerinck, and K. A. H. van Leeuwen, manuscript in preparation
- [2] R. C. M. Bosch, PhD thesis, TU/e (2002)
- [3] R. C. M. Bosch, H. C. W. Beijerinck, P. van der Straten, and K. A. H. van Leeuwen, *Eur. Phys. J. A. P.* **18**, 221-227 (2002)
- [4] O. F. Hagen, *Z. Phys.* **D 20**, 425 (1991)
- [5] *CRC Handbook of Chemistry and Physics*, 84th Ed. (CRC Press, Boca Raton, 2003)
- [6] H. C. W. Beijerinck and N. Verster, *Physica* **111 C**, 327-352 (1981)
- [7] D. Spišák and J. Hafner, *Phys. Rev.* **B 70**, 195426 (2004)
- [8] R. Cortenraad, S. N. Ermolov, V. N. Semenov, A. W. Denier van der Gon, V. G. Glebovsky, S. I. Bozhko, and H. H. Brongersma, *J. Crystal Growth* **222**, 154-162 (2001)
- [9] H. Lüth, *Surfaces and Interfaces of Solid Materials*, 3rd ed., Springer (1997)
- [10] R. E. Honig and D. A. Kramer, *RCA Review* **30**, 285-305 (1969)
- [11] V. K. Kumikov and Kh. B. Khokonov, *J. Appl. Phys.* **54**, 1346-1349 (1983)
- [12] Search for alloys and compounds performed using www.google.com

THE CHOICE FOR IRON AND ITS CONSEQUENCES

Chapter 3

Atoms in standing waves

The description of the atom-light interaction in terms of classical induced dipole moments given in the introduction suffices to understand that standing waves can act as lenses on atoms. However, it is not enough to understand all the experiments discussed in this thesis. Hence, we need to discuss a more refined theory, specifically the dressed state model [2]. We will first outline the theory, and then investigate its implications for atom lithography experiments. This chapter is intended mainly to help the reader understand the simulations and experiments done in Chapters 5 and 7.

1 Theory

An atom in a light field close to a resonance will absorb and re-emit photons. The re-emission can occur in two ways: the atom can decay spontaneously to its ground state, or it can undergo stimulated emission. The model discussed here seeks to describe the effect of all stimulated emissions as a semiclassical dipole potential; spontaneous emission is considered separately later on.

1.1 The semiclassical approximation

This approach is valid if the atom can be considered as a point particle that moves through a potential landscape with a well-defined velocity. This means that the wave nature of the atom can be neglected when considering its center-of-mass motion. Hence, the position uncertainty of the atom must be much smaller than the wavelength λ of the light. Taking the De Broglie wavelength λ_{DB} as a measure of this uncertainty:

$$\lambda_{DB} \ll \lambda. \quad (3.1)$$

For iron atoms moving at 1000 m/s, $\lambda_{DB} = 7$ pm, and $\lambda_{DB}/\lambda \approx 2 \times 10^{-5}$. However, the diffraction limit for atom optics is far greater than the De Broglie wavelength, as the numerical aperture of the lenses is very small. Typical values are around 10 nm [1].

ATOMS IN STANDING WAVES

In this context, the uncertainty in the velocity $\Delta(v)$ is effectively small if the uncertainty in the Doppler shift it induces is much smaller than the natural linewidth $\Gamma = 2\pi \times 2.58$ MHz of the transition:

$$k\Delta(v) \ll \Gamma, \quad (3.2)$$

with k the wave number of the laser light. The velocity uncertainty is of the order of one recoil kick $\hbar k/m = 0.02$ m/s. This yields a Doppler shift of 0.02Γ . We thus conclude that the position and velocity of the atom are well-defined, and that it may be considered as a point particle.

1.2 Dressed states

The dressed state model discussed here was first introduced by Dalibard and Cohen-Tannoudji in 1985 [2]. The adjective “dressed” refers to the fact that one considers not the eigenstates of the atom but rather those of the complete atom-light field system.

A stationary atom in a light field will have a Hamiltonian of the form:

$$H = H_{atom} + H_{light} + H_{int}, \quad (3.3)$$

which is nothing more than saying that there will be energy contributions from the state of the atom (H_{atom}), the state of the light field (H_{light}), and the interaction between the two (H_{int}). We assume that the atom is a two-level atom, though the approach also works for more complicated atomic structures. The internal energy of the atom is zero in the ground state, and $\hbar\omega_0$ in the excited state.

The frequency of the laser ω_L is assumed to be such that $|\omega_L - \omega_0| \ll \omega_0$. The energy eigenvalues of the light field are $E_n = (n + \frac{1}{2})\hbar\omega_L$, with n the number of photons in the light field. This is a “ladder” of states separated by $\hbar\omega_L$, as shown in Fig. 3.1(a). If we now include the atom in the Hamiltonian, we get a ladder of pairs of states. For blue detuning ($\Delta = \omega_L - \omega_0 > 0$), the ladder is shown in Fig. 3.1(b). The separation between the states in a pair is equal to $\hbar\Delta$, much smaller than the separation between the pairs $\hbar\omega_L$.

These states become dressed when the interaction between the atom and the light field is taken into account. This interaction mixes the states of the light field and the atom and shifts the eigenenergies of the system. The coupling between the atom and the light field takes place almost entirely within a pair of states on the ladder, and can be characterized by the Rabi frequency ω_R and the phase ϕ of the light field. The Rabi frequency is related to the intensity of the light field by $\omega_R = \Gamma\sqrt{I/2I_s}$. After solving for the eigenstates and eigenenergies of the complete system, Dalibard and Cohen-Tannoudji find that for each n , there is a pair of eigenstates with:

$$\begin{aligned} E_{n,+} &= (n+1)\hbar\omega_L - \frac{\hbar\delta}{2} + \frac{\hbar\Omega}{2}, \\ E_{n,-} &= (n+1)\hbar\omega_L - \frac{\hbar\delta}{2} - \frac{\hbar\Omega}{2}. \end{aligned} \quad (3.4)$$

THEORY

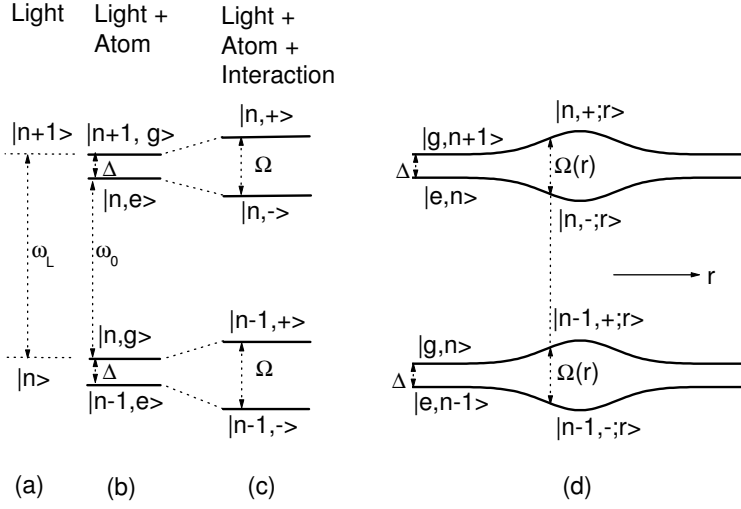


Figure 3.1: Energies of the eigenstates of the system under consideration. (a) Eigenstates of light field. (b) Eigenstates of light field and atom. (c) Eigenstates of the light field and atom including interaction, usually referred to as “dressed states”. (d) Position dependent dressed states generate a potential landscape.

The frequency separation between the dressed states Ω depends on ω_R and Δ by:

$$\Omega = \sqrt{\omega_R^2 + \Delta^2}. \quad (3.5)$$

The dressed states themselves are a linear superposition of the ground and excited states:

$$\begin{aligned} |n, +\rangle &= \exp(i\phi/2) \cos(\theta) |e, n\rangle + \exp(-i\phi/2) \sin(\theta) |g, n+1\rangle; \\ |n, -\rangle &= -\exp(i\phi/2) \sin(\theta) |e, n\rangle + \exp(-i\phi/2) \cos(\theta) |g, n+1\rangle. \end{aligned} \quad (3.6)$$

Here θ is defined by:

$$\cos 2\theta = -\Delta/\Omega. \quad (3.7)$$

The separation between the dressed states is always greater than that between the bare states for finite light intensity, as is shown in Fig. 3.1(c). For the situation under consideration here, the exact value of n is not important. As long as n is large, the light shifts are not affected significantly by the addition or removal of a single photon. We will feel free to omit it in the remainder of this work.

Generally, the phase and intensity of a light field will depend on position \vec{r} . As a result of the intensity variations, the energy of the dressed states will also vary with position. This generates a potential landscape that the atoms move through, as shown in Fig. 3.1(d). We will use this potential in the remainder of this thesis.

1.3 Spontaneous emission

Not included in the dressed states are the effects of spontaneous emission. This process is a transition from the excited state to the ground state, during which n decreases by one. The rate at which an atom undergoes spontaneous emissions is proportional to its excited state population. This population can be derived from Eq. 3.6. The chance that an atom will end up in a given dressed state is given by the ground state population of that state. An atom that undergoes a spontaneous emission thus has a finite chance of remaining in its original dressed state, and a finite chance of changing dressed state. The transition rates between dressed states that result from these chances can be expressed in terms of the angle θ defined above:

$$\Gamma_{+-} = \Gamma \cos^4 \theta; \quad (3.8)$$

$$\Gamma_{-+} = \Gamma \sin^4 \theta. \quad (3.9)$$

After many spontaneous emissions, a balance between the dressed states is formed, and the effective potential averaged over both dressed states can be described by a logarithmic function [2]. In the case of atom lithography, this is explicitly not the correct description. An atom that moves through a 0.1 mm laser beam at 1000 m/s interacts with the light for some 100 ns. The natural decay time of the transition under consideration in this thesis is 62 ns. The fact that less than half of the atoms is in the excited state means that the effective decay time will be more than twice this value. This means that typically, atoms will undergo zero or one spontaneous emission events in the course of the entire focusing interaction, hardly enough for any kind of radiative balance.

In addition, the atom receives a recoil kick in a random direction any time a spontaneous emission occurs. The effects of this recoil kick are normally small in atom lithography. After one recoil at the start of the interaction, the resulting velocity change of 0.02 m/s, entails a displacement of 2 nm at the end of the interaction. This is not a significant displacement.

1.4 Moving atoms

The dressed states are eigenstates for *stationary* atoms. If the atomic center-of-mass position \vec{r} varies with time, so do the eigenstates of the atom-light system. The atom can follow these variations adiabatically if its motion, and hence the rate of change of its eigenstates, is slow enough. If the eigenstates change very quickly, the internal state of the atom will remain unchanged, and only its description in terms of the dressed states will change. Viewed from the dressed state perspective, there is a chance that it is transferred from one dressed state into the other. This is called a nonadiabatic transition.

An upper limit estimate of the nonadiabatic (NA) transition probability $P_{i \rightarrow j}$ between levels $|n, i; \vec{r}\rangle$ and $|n, j; \vec{r}\rangle$ can be found in Ref. [3]:

$$P_{i \rightarrow j} \leq \max \left\{ \frac{|\langle n, j; \vec{r} | \frac{d}{dt} | n, i; \vec{r} \rangle|^2}{|\omega_{ij}|^2} \right\}, \quad (3.10)$$

NUMERICAL MODEL

where ω_{ij} is the Bohr frequency between levels i and j at time t . In the dressed state model, $|i\rangle$ and $|j\rangle$ can be $|+\rangle$ or $|-\rangle$, and $\omega_{ij} = \Omega[\vec{r}(t)]$. The overlap integral in the numerator can be found using Eq. 3.6 assuming constant phase ϕ :

$$\frac{d}{dt}|n, i; \vec{r}\rangle = \frac{d\vec{r}}{dt} \cdot \vec{\nabla}|n, i; \vec{r}\rangle = \pm \vec{v} \cdot \vec{\nabla} \theta(\vec{r})|n, j; \vec{r}\rangle. \quad (3.11)$$

The gradient of θ can be found using Eq. 3.7. If we insert a sine-shaped standing wave with maximum Rabi frequency $\omega_{R,max}$ as the expression for I , we can thus estimate the NA transition probability as:

$$P_{i \rightarrow j} \lesssim \max \left[\left(\frac{\vec{k} \cdot \vec{v}}{2} \right)^2 \frac{|\Delta \omega_{R,max} \cos(\vec{k} \cdot \vec{r})|^2}{|\Delta^2 + \omega_{R,max}^2 \sin^2(\vec{k} \cdot \vec{r})|^3} \right]. \quad (3.12)$$

From this expression, we can find where the NA transitions are most likely to occur: around the nodes of the standing wave. The chance for a NA transition when an atom traverses a node is overestimated by:

$$P_{i \rightarrow j} \lesssim \left| \frac{\vec{k} \cdot \vec{v} \omega_{R,max}}{2 \Delta^2} \right|^2 \quad (3.13)$$

Clearly, a large detuning and modest Rabi frequency help limit the amount of NA transitions. As with the spontaneous emissions, the model treats NA transitions as a correction in hindsight.

2 Numerical model

We will now proceed to apply the dressed state model described above to atom lithography. What we seek is a prediction of the atomic flux distribution after the interaction with the light field. To this end, we will solve the equations of motion for a large number of atoms numerically. We will discuss the results of these simulations.

2.1 Equations of motion

The atoms are classical point particles moving through a potential U . The energy shift of the atoms as a function of the light field intensity I and detuning Δ is:

$$U = \pm \frac{\hbar}{2} \sqrt{\frac{I(\vec{r})}{2I_s} \Gamma^2 + \Delta^2} - \frac{\hbar \Delta}{2}, \quad (3.14)$$

where the sign is that of the dressed state the atom is currently in. Calculating the trajectory of an atom through a light mask is now just a matter of integrating its Newtonian equation of motion.

We describe our light mask as a one-dimensional Gaussian standing wave, obtained by superposition of two running waves with a waist of width w :

$$I(\vec{r}) = I_0 \sin^2(kx) \exp\left(-2 \frac{z^2}{w^2}\right). \quad (3.15)$$

ATOMS IN STANDING WAVES

Here $k = 2\pi/\lambda$ is the wave number of the running wave, and the atoms are assumed to move along the z -axis. The central intensity can be described in terms of the running wave power by $I_0 = 8P/\pi w^2$

Assuming that the atoms' kinetic energy is much larger than the potential height of the light mask allows us to neglect its effect on their longitudinal motion. We thus concentrate on their lateral motion, which is far slower:

$$F_x = -\frac{\partial U}{\partial x} = m \frac{\partial^2 x}{\partial t^2}. \quad (3.16)$$

As our interest lies in the trajectories of the atoms, we transform from t to z by introducing v_z . If we further introduce dimensionless parameters $\chi = kx$ and $\zeta = z/w$, the resulting equation reads:

$$\frac{d^2\chi}{d\zeta^2} = \pm AB \frac{\exp(-2\zeta^2) \sin(2\chi)}{\sqrt{1 + B \exp(-2\zeta^2) \sin^2(\chi)}}. \quad (3.17)$$

Here, we have defined:

$$A = \frac{k^2 w^2 \hbar |\Delta|}{2m v_z^2}$$

$$B = \frac{4P\Gamma^2}{\pi w^2 I_s \Delta^2} = \frac{\omega_{R,max}^2}{\Delta^2} \quad (3.18)$$

On inspection of A , we find that the $m v_z^2$ term is a measure for the kinetic energy of the atoms. Also, the factor $k^2 w^2$ can be traced directly to the aspect ratio w/λ of the potential variations. The ratio $m v_z^2/k^2 w^2$ is a measure for the maximum kinetic energy of the transverse motion of the atoms that fit within the acceptance angle of the atom lenses. On the other hand, $\hbar\Delta$ is the energy splitting between the dressed states outside the light mask. Thus, we find that A physically represents the ratio between the transverse kinetic energy of the atoms that can be focused and the splitting of the dressed states outside the standing wave.

All the terms that enter into B are related to the light mask itself. The maximum intensity in the light mask is given by Eq. 3.15, and reappears here. So B can clearly be interpreted as a measure of the maximum saturation parameter divided by the detuning expressed in linewidths. In terms of energy, \sqrt{B} measures the maximum light shift in units of the splitting of the dressed states outside the standing wave.

Outside the standing wave, the intensity I of the light is zero, and the ground state is $|+\rangle$ for $\Delta > 0$ and $|-\rangle$ for $\Delta < 0$. Unless they undergo a spontaneous or nonadiabatic transition, they will stay in their initial state, and their trajectory can be calculated by simply integrating Eq. 3.17.

2.2 Spontaneous emissions

We include the effects of spontaneous emission in the model by evaluating the chance that an atom has undergone spontaneous emission at set intervals. The spontaneous decay rate from one dressed state to the other can be obtained from

NUMERICAL MODEL

Eq. 3.8. Seeking to express θ in terms of the model parameters, we recall Eq. 3.7. This can be rewritten as:

$$\sin[2\theta(\vec{r})] = \tilde{B}(\vec{r}) / \sqrt{1 + \tilde{B}(\vec{r})^2}, \quad (3.19)$$

with $\tilde{B}(\vec{r}) = B \exp(-2\zeta^2) \sin^2(\chi)$. Now, we can obtain an expression for the maximum spontaneous emission rate in terms of $B(\vec{r})$:

$$\Gamma_{DS}(\vec{r}) = \frac{\Gamma}{2} \frac{1 + \frac{1}{2}\tilde{B}(\vec{r}) \pm \sqrt{1 + \tilde{B}(\vec{r})^2}}{1 + \tilde{B}(\vec{r})}, \quad (3.20)$$

where the sign is negative if the signs of the detuning Δ and the dressed state are the same. The chance that an atom has undergone a spontaneous emission in time interval τ is now simply $\Gamma_{DS}\tau$.

An upper limit to the chance of spontaneous emission during the interaction with the light mask is given by $\Gamma w / v_z$, as the light mask extends from $z = -w$ to $z = w$, and the spontaneous decay rate is $\Gamma/2$ at most. This is typically of order unity in our experiments.

2.3 Non-adiabatic transitions

The probability for non-adiabatic transitions to occur is more difficult to calculate, and one would be better off simply solving the optical Bloch equations numerically. However, we can estimate the effects of non-adiabatic transitions crudely. Non-adiabatic transitions are most likely to occur when atoms cross a node, and so we state in our model that they occur *exclusively* when an atom crosses a node.

The estimate for the NA transition probability (Eq. 3.13) can be rewritten in terms of the numerical model parameters:

$$P_{i \rightarrow j} \lesssim \left(\frac{kv}{2\Delta} \right)^2 B. \quad (3.21)$$

We set the model NA transition probability to unity if the above estimate is greater than unity; else, we set it to zero. Though it is only a crude approximation, it is satisfactory for the present model. For an atom moving with 1 m/s in the x -direction through a standing wave detuned by 150 MHz, the value of the estimate is unity for $B \sim 10^4$.

2.4 Calculation

We start with a number of atoms that are homogeneously distributed over a single wave length in the x -direction. The transverse velocity distribution of a laser cooled atomic beam is approximately Gaussian [4]; that of an uncooled beam from a round nozzle can be approximated by a Gaussian. The atoms have a Gaussian transverse velocity distribution. The longitudinal velocity distribution of the atom beam is that of an effusive beam (see Ch. 2). The longitudinal velocities are assigned in ascending order; all other parameters are chosen randomly for each trajectory.

ATOMS IN STANDING WAVES

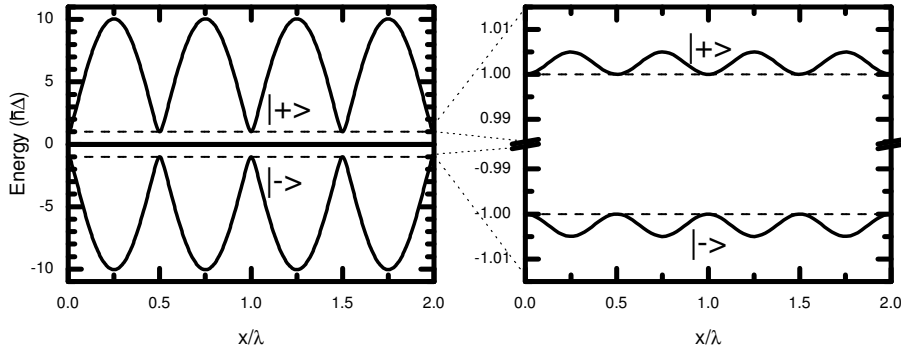


Figure 3.2: Left: Dressed state potentials for $B = 100$. Dashed lines indicate zero-intensity levels. Note the difference in shape between the potential minima for $|+\rangle$ and $|-\rangle$ states. Right: Same, for $B = 0.01$. Sine-like potential strongly resembles classical case.

We approximate the magnetic substructure of the transition used by assigning each atom to a random substate, after which the calculation is performed using the appropriate Clebsch-Gordan coefficient for each atom. We assume that the light used is linearly polarized.

The equation of motion of every atom is integrated over a set distance, before we check for spontaneous and NA transitions. The effect of either is to change from one dressed state to the other. The possibility that atoms that undergo spontaneous emission decay to a different magnetic substate is neglected. We make a histogram of the atomic flux distribution at set intervals. These histograms are saved to a data file.

3 Results

Before we show the results of these semiclassical simulations, we discuss the potential that is used. The left part of Fig. 3.2 displays the potential for the case of a very strong light field, where $B = 100$. The case of a very weak light field with $B = 0.01$ is displayed to the right. It is immediately apparent that both potentials are very different in shape as well as in scale.

In the high- B potential, the potential minima of the $|+\rangle$ state differ radically in shape from those of the $|-\rangle$ state. The minima of the $|-\rangle$ state are smooth, broad and parabolic over a large range. In fact, the potential looks like a series of parabolas at first glance. This could be a way to circumvent any nonparabolic aberrations in the atom focusing process. On the other hand, the minima of the $|+\rangle$ state are very unparabolic, looking more like a V-shaped potential. The result is that the oscillation time of the atoms within the potential depends on the starting point of the oscillation. This is not optimal for perfect focusing, but does have an advantage for preliminary experiments such as those performed in this thesis. The axicon-like potential should create focus lines rather than focal points, as the starting position of the atoms is homogeneously distributed. Hence, the formation of structures should

RESULTS

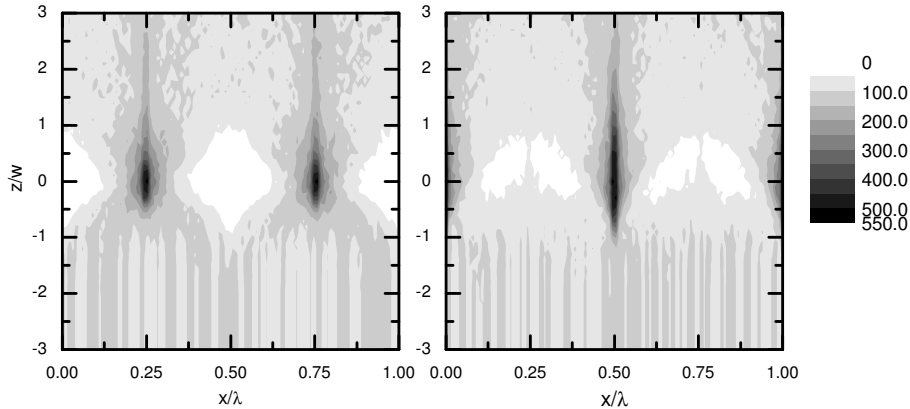


Figure 3.3: Flux distribution of an atomic beam passing from below through a strong light mask. Left: $\Delta > 0$ generates focus points. Right: $\Delta < 0$ gives rise to focus lines.

be far less sensitive to the experimental parameters.

The potential for a weak standing wave is very sine-like. The difference between the $|+\rangle$ and $|-\rangle$ state minima has effectively vanished, and focusing is expected to proceed in a similar fashion for both states. For positive detuning, the atoms start out in the $|+\rangle$ state, and due to the low spontaneous emission rate, they stay in that state. Hence the atoms get focused in the potential minima by a sine-like potential. For negative detuning, the same story applies, except that the sine-like potential now focuses the atoms in the intensity maxima. This is in complete agreement with the classical image presented in the introduction.

To demonstrate the difference between the two detunings, we simulated a perfectly collimated atom beam that interacts with a strong standing wave. The longitudinal velocity distribution was taken to be at 2000 K; the light mask was assumed to have a running wave power of 50 mW in a 50 μm radius beam waist at a detuning of 150 MHz (58 Γ). The results are shown in Fig. 3.3. Interaction with a red-detuned standing wave generates focus points, as shown on the left. The blue-detuned standing wave gives rise to focus lines, as shown on the right. A typical simulation of 10000 atoms under these circumstances gave rise to zero NA transitions. For blue detuning, some 4500 spontaneous emissions occurred, meaning that the majority of atoms did not undergo *any* spontaneous emissions. For red detuning, some 7000 emissions occurred, reflecting the fact that atoms are drawn to intensity maxima in this case.

The relatively long z -range over which atom focusing occurs for the red detuned case stands out. The strength of the lenses varies per atom. This is due mainly to the spread in Clebsch-Gordan coefficients for the Fe atoms; secondarily, the longitudinal velocity spread of the Fe atoms also contributes. The spread in Clebsch-Gordan coefficients can be compensated for relatively easily by optical pumping to an extreme circular state. The longitudinal velocity spread is a more difficult issue, as described in Ch. 2.

References

- [1] C. J. Lee, Phys. Rev. A 61, 063604 (2000); S. J. H. Petra, K. A. H. van Leeuwen, L. Feenstra, W. Hogervorst, and W. Vassen, Eur. Phys. J. D 27 83-91 (2003).
- [2] J. Dalibard and C. Cohen-Tannoudji, J. Opt. Soc. Am. **B 2**, 1707-1720 (1985)
- [3] A. Messiah, Mécanique Quantique II, Dunod, Paris (1964)
- [4] H. Metcalf and P. van der Straten, Laser Cooling and Trapping, Springer Verlag, Heidelberg (1999)

Chapter 4

Experimental apparatus

In this chapter, the experimental setup is described that is used to deposit the Fe nanostructures. This setup must fulfill a number of criteria. It must obviously contain an Fe evaporation source, and must provide for both laser cooling and the interaction with the light mask. A laser system has to provide the necessary light for both. Finally, it must allow for application of a capping layer *in vacuo* to protect the nanostructures from oxidation.

A schematic overview of the atomic beam line is given in Fig. 4.1. The atoms exit the source (1) and pass through a 2 mm diameter aperture (2) before being collimated in the laser cooling section (3). For alignment and diagnostic purposes, a removable 10 μm slit (4) has been installed between the laser cooling and deposition sections. The atoms are deposited onto a substrate (5) in the deposition chamber. Finally, imaging of the atomic beam is possible with a light sheet and CCD camera (6) at the end of the beam line.

1 Vacuum system

We choose to house the three beam line sections in different stainless steel vacuum chambers, allowing for differential pumping. Also, we add a load lock so that samples may be brought into the deposition chamber without breaking its vacuum. An overview of the vacuum setup is shown in Fig. 4.2.

The evaporation source is located in a separate vacuum chamber. In effusive mode, the background pressure in the source chamber must be low enough that the Fe atoms that leave the source do not collide with background gas atoms as they traverse the chamber. The mean free path of the Fe atoms λ with respect to collisions with background gas is given by [1]:

$$\lambda = \frac{1}{n\sigma \frac{v_{rel}}{v_{Fe}}}, \quad (4.1)$$

where n is the background gas atomic number density, and σ is the collision cross-section. We estimate σ at 0.5 nm². The relative velocity of the atoms $v_{rel} = \sqrt{v_{BG}^2 + v_{Fe}^2}$ depends on the velocities of the background gas molecules and the Fe

EXPERIMENTAL APPARATUS

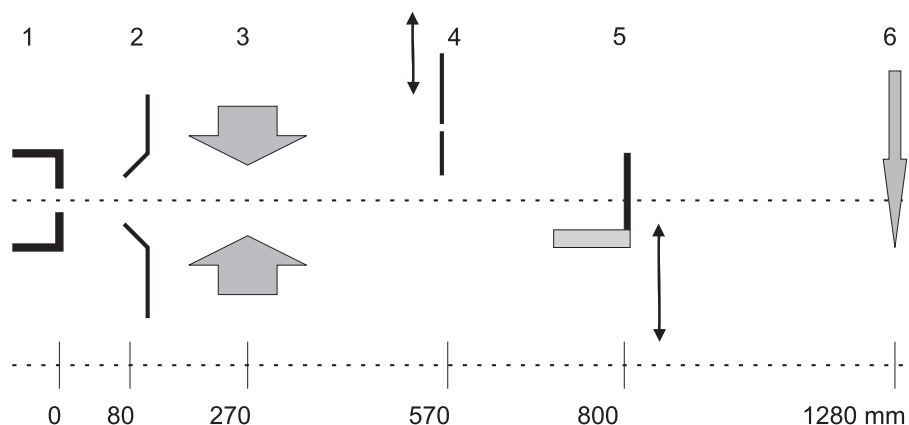


Figure 4.1: Schematic of the atomic beam line. (1) Fe source crucible. (2) Skimmer for differential pumping. (3) Laser cooling section. (4) Movable slit. (5) Deposition setup; only sample and mirror are shown. (6) Light sheet for atom beam imaging.

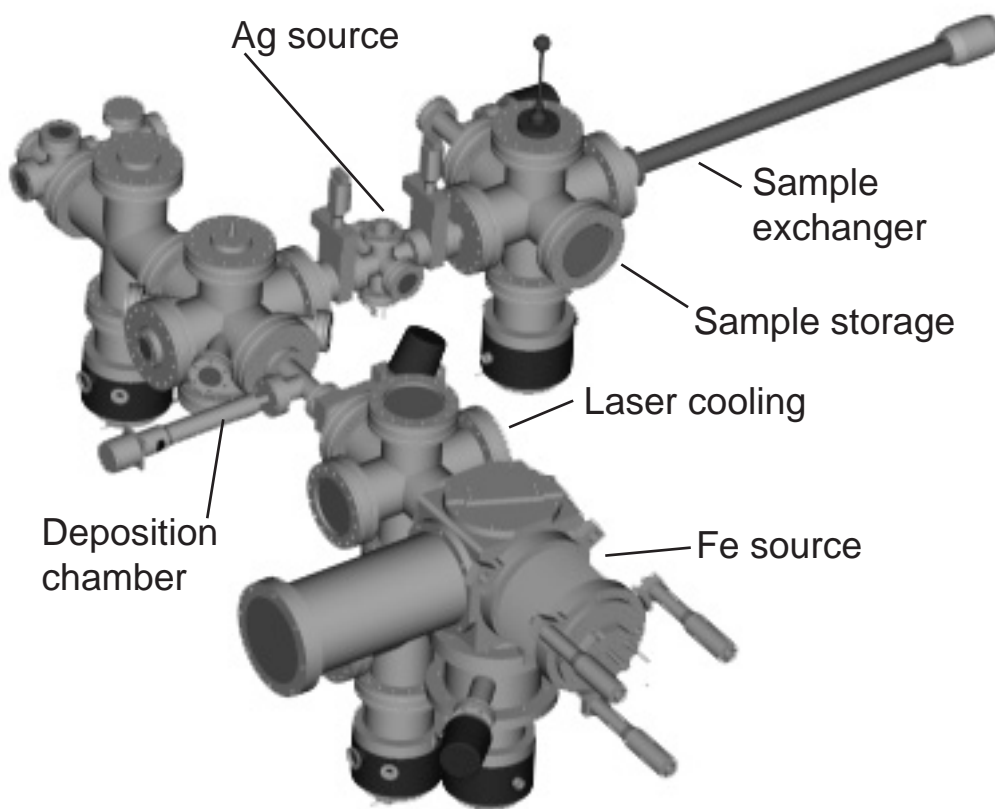


Figure 4.2: Vacuum setup. Fe beam line from bottom right to top left. Top right: sample exchanger.

FE SOURCE

atoms (v_{BG} and v_{Fe} , respectively). For an Fe atom traveling at 1000 m/s, the mean free path is equal to the chamber size (0.2 m) when the background pressure is 4×10^{-4} mbar. We demand that the pressure in the source chamber must be lower than 10^{-4} mbar. We achieve this pressure by pumping the vacuum chamber with a 100 l/s turbomolecular pump.

Transverse laser cooling is applied to the Fe atoms as close to the source as possible. The laser-cooled atom beam is far better collimated, and hence less sensitive to divergence-related flux losses. The laser cooling section must only have a low enough pressure that the Fe atoms traverse it without colliding. An estimate similar to that above yields a maximum allowable pressure of $\leq 5 \times 10^{-5}$ mbar, easily achieved by the 250 l/s turbomolecular pump.

The background pressure in the deposition vessel must be low enough that the background flux is small compared to the Fe beam flux. This requirement translates into a background pressure lower than 10^{-11} mbar. The turbomolecular pump attached to this chamber can achieve a pressure of 10^{-10} mbar. However, gas flow from the relatively high-pressure source chamber limits the achievable pressure to 10^{-9} mbar. The background gas consists mainly of hydrogen and helium due to the velocity selectivity of the pumping mechanism. Fortunately, Fe does not react with hydrogen, and our worries can be restrained to the heavier molecules that do react with Fe. We hope to achieve relatively pure deposition in spite of the poor overall background pressure.

A sample exchange mechanism is required both to allow for the application of a capping layer, to preserve the vacuum in the deposition chamber and, most importantly, to allow alignment of the atom beam with a sample in the vacuum system. A separate vacuum chamber acts as a load lock. It contains a storage space capable of containing up to four samples. A magnetic linear drive is used to transport the samples to and from the load lock. The Ag source is situated halfway between the deposition chamber and the load lock. A turbomolecular pump achieves a pressure below 10^{-7} mbar in the load lock.

2 Fe source

We obtain a bright atomic Fe beam from a custom-designed beam source [2] described below. The same design can be configured to generate both a thermal and a supersonic iron atom beam with little effort.

2.1 Design

Figure 4.3 shows a schematic design of the iron source. Its interior is isolated thermally from the water cooled vacuum vessel by Ta foil radiation shielding. A graphite coil with a resistance of 0.6Ω heats a crucible containing Fe to around 2000 K at 1000 W heating power. Argon gas can be let in through a tantalum tube from the left for supersonic operation. The beam exits the tube through a 1 mm diameter supersonic expansion nozzle. The hole in the heat shields through which the Fe atoms

EXPERIMENTAL APPARATUS

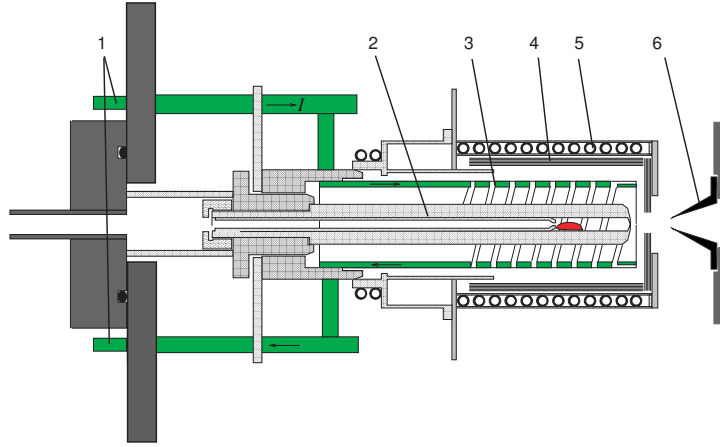


Figure 4.3: Fe source design. Heating current for graphite coil (4) comes through copper electrodes (1). Aperture (7) defines beam from expansion out of crucible (3). Water cooled oven (6) is isolated by 20 Ta foil radiation shields (5).

leave the oven is 6 mm diameter.

The effective temperature of the source is the temperature of the iron droplet inside the crucible. As this droplet is free to creep around, we cannot know where it will be; therefore, we cannot measure this temperature directly. We thus need to measure the Fe atom flux experimentally. Two available techniques allow for Fe flux measurements: Laser Induced Fluorescence (LIF) and mass flux measurements using a McVac MCM-160 quartz crystal microbalance.

Laser Induced Fluorescence

The basic principle of LIF is to observe the fluorescence of the atoms in a beam as they are irradiated by a laser beam. An atom subjected to resonant laser light will be excited, and subsequently decay to a lower lying state. The leak present in atomic Fe is small enough that decays to any other state than the ground state may effectively be neglected, provided that the interaction time is short enough. For atoms in motion, the Doppler effect causes a shift away from resonance, reducing the net photon scattering rate. The photon scattering rate Γ_p for arbitrary detuning δ_0 is given by [3]:

$$\Gamma_p = \frac{\Gamma}{2} \frac{s_0}{1 + s_0 + \left(\frac{\delta_0 - \vec{k} \cdot \vec{v}}{\Gamma}\right)^2}. \quad (4.2)$$

In Eq. 4.2, \vec{k} is the wave vector of the laser light, and \vec{v} is the velocity of the atom. We align the light beam such that $\delta_0 - \vec{k} \cdot \vec{v} = 0$ in the center of the detection area. The beam is highly saturated for $s_0 \gg 1$. We denote the variation in $\vec{k} \cdot \vec{v}$ by $\Delta(\vec{k} \cdot \vec{v})$. The photon scattering rate is close to the limiting value $\Gamma/2$ in the entire detection area for $\sqrt{s_0} \gg \Delta(\vec{k} \cdot \vec{v})/\Gamma$. In our setup, we expect the Fe atoms to have longitudinal velocities ~ 1000 m/s, and the detection range is geometrically limited to ± 2 mrad.

FE SOURCE

For saturation over the entire detection area, we need a saturation parameter such that $\sqrt{s_0} \gg 2$, which is easily obtained.

In principle, the emission pattern detected by a CCD camera can be used to determine the absolute atomic density, from which, in turn, the flux can be determined. In practice, this requires knowing the quantum efficiency of the CCD detector and the transmission coefficient and collection angle of the optics in front of it. This time-consuming calibration has not been performed; instead, we use LIF as a relative flux calibration. We derive the absolute flux calibration from growth rate measurements using a quartz crystal microbalance.

Flux calibration

The measurements of the total mass flux out of the source are shown in Fig. 4.4 as squares. The LIF measurements are shown as circles, and have been fitted to the curve by normalization at 32 A. Clearly, for source currents over 33 A, the total mass flux increases much faster than the ${}^5\text{D}_4$ Fe flux.

Kinetic gas theory yields a relationship between the effective source temperature and the deposition rate at a given distance from the source, as detailed in Ch. 2. The uncertainty in the experiment is in the temperature measurement. We determine an effective temperature from the measurement of the Fe flux at 32 A. We relate this to the temperature at other current settings by the Stefan-Boltzmann radiation law. This is a safe assumption at these high temperatures. We have measured that the heating coil is Ohmic, and can thus state that:

$$T(I_1)/T(I_0) = [P(I_1)/P(I_0)]^{\frac{1}{4}} = (I_1/I_0)^{\frac{1}{2}}. \quad (4.3)$$

This can then be used to predict the flux from the Fe source at all other input powers. Here, too, we have normalized the curves at 32 A, where the operational temperature proved to be 1830 K, and the Fe vapor pressure 0.05 mbar. This calculation is shown in Fig. 4.4 as a dashed line.

Whereas the agreement between the theoretical curve and the LIF data is reasonable, there is an obvious discrepancy between the mass flux and the LIF flux at higher source currents. This means that matter other than Fe must be codeposited.

At source currents higher than 35 A, the overall pressure in the Fe source chamber rises rapidly. This indicates that the source produces material that is gaseous at room temperature. Given the elements present in the source (Fe, Al, O, C, and Ta), the most likely gas is CO_x . This can only be generated if the carbon from the heating coils somehow reacts with the oxygen in the alumina crucible. A possible transfer mechanism is a reaction between the Fe vapor in the source oven and the graphite heating coil to produce iron carbide (Fe_3C). The iron carbide vapor could then dissociate on the alumina crucible, producing CO_x . The Fe_3C vapor then also leaves the source with the Fe, explaining the increase in mass flux measured with the microbalance. Further investigation would be necessary to ascertain the nature of the reaction with any degree of certainty.

This problem can only be mitigated by replacing the graphite heating coil with, for instance, a tungsten coil. However, tungsten is not as self-supporting as graphite

EXPERIMENTAL APPARATUS

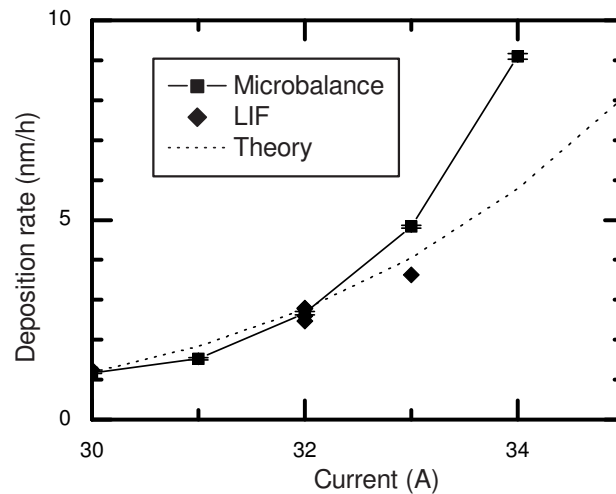


Figure 4.4: The Fe deposition rate as a function of source heating current. Squares and line: total flux measured using a crystal microbalance. Circles: LIF data, measuring the ${}^5\text{D}_4$ Fe flux. Dashed line: theoretical calculation.

is, meaning that the whole oven would have to be redesigned. We choose to work with the existing oven design, and accept the flux limitation this imposes.

3 Deposition

The most basic form of atom lithography experiment requires a laser beam and an atom beam perpendicular to each other. We choose an integrated, compact sample holder on which both the sample and the mirror that is used to create the standing light wave are mounted rigidly at a minimal distance from one another. The sample holder is shown in Fig. 4.5. This design has two advantages. Most importantly, the rigid mounting of sample and standing wave mirror suppresses drifts and oscillations in their relative position and angle. As a side effect, this setup means that a new mirror-sample assembly can be designed and constructed *ex vacuo* and easily be tested. The drawback to this approach is that the sample holder placement in the vacuum vessel must be very reproducible to avoid repeating the laborious procedure after each deposition run.

In the experiments described here, the sample holder holds a 0.5 mm thick piece of Si[100] wafer. The sample can be from 3 to 8 mm wide, and from 2 to 10 mm long (perpendicular to the mirror). Typically, it is cut to 6×6 mm. It is clamped rigidly onto a 4 mm thick Macor slab by screw-clamps. The space between the clamps is 2 mm wide, more than enough for the experiments we wish to perform. The uncooled Fe beam extends to around 5 mm from the mirror.

The Macor electrically isolates the sample from the rest of the vacuum system. The Macor, in turn, is attached to a stainless steel sample holder. The 8 × 8 × 3 mm

DEPOSITION

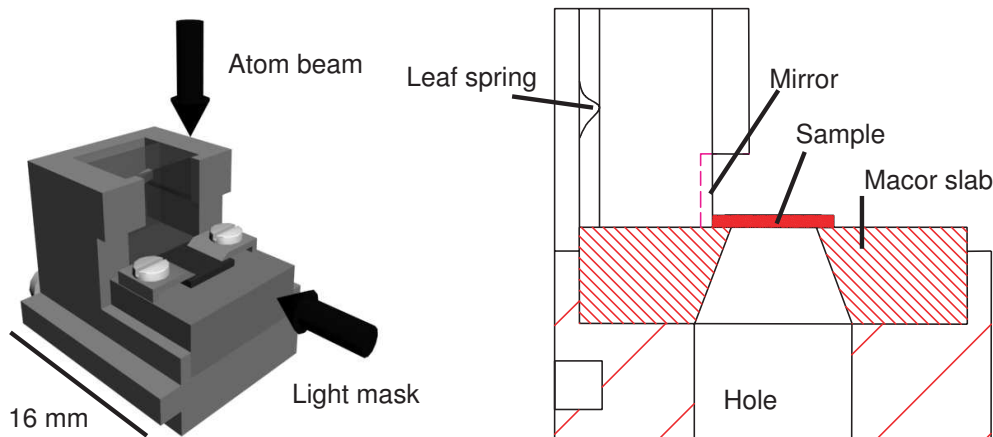


Figure 4.5: Left: sample holder. Right: Cross section of sample holder. The sample is clamped to a macor isolator that is screwed onto the steel frame. The mirror is pressed to the frame by a spring.

mirror (reflectivity > 0.99) is clamped to the sample holder by a steel leaf spring. Once fastened, the sample has no degree of freedom relative to the mirror other than through thermal expansion. Small adjustments in the mirror orientation of a few mrad are possible by shifting the spring with a pair of tweezers. This shifts the effective point where the leaf spring presses the mirror to the sample holder. The mirror orientation with respect to the samples could thus be adjusted with an accuracy of 0.5 mrad.

A hole through the sample holder and Macor slab provides access to the rear of the sample. The electron gun that was installed to bake out the samples targets the sample through this hole. Also, a stainless steel dummy sample with a 0.5 mm diameter hole in it can now be used as an *in vacuo* atom beam alignment tool. We permanently devote one of the four sample holders to this task.

We have chosen a setup with movable sample holders. Hence, the alignment of the sample holder relative to the vacuum chamber must be highly reproducible, as adjustment of the alignment of *in vacuo* components is technically demanding. The sample holder is held reproducibly in a seat, rigidly mounted in the vacuum vessel, by a set of stainless steel leaf springs. The springs are capable of withstanding temperatures up to 500 °C, ensuring that they remain elastic despite baking out numerous samples. After several deposition runs, problems developed due to mutual roughening of the sample holder and the springs. Eventually, the sample holders either no longer touched the springs, or the shear resistance between the sample holders and the springs was so large that they could no longer be moved by the magnetic linear drive. A solution was found in placing 'lubricating' Boron Nitride spacers between the sample holder and the springs. The spacers are part of the seat; we found no need to replace them during a year of frequent experiments.

EXPERIMENTAL APPARATUS

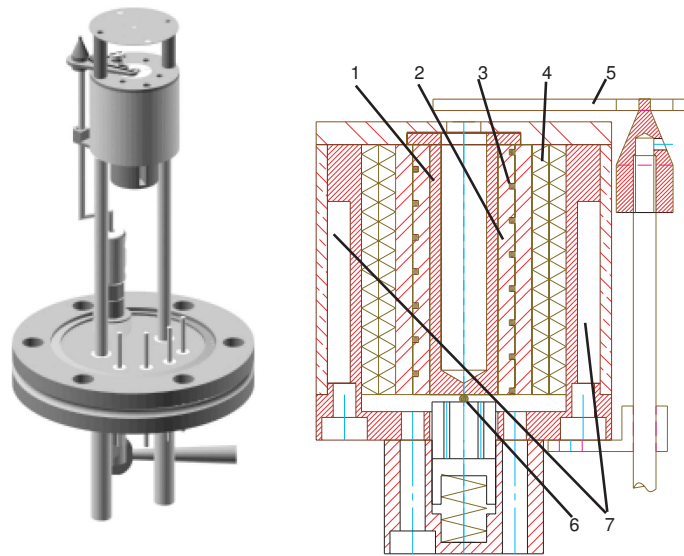


Figure 4.6: Left: Ag source. Water cooling through legs. Not shown: heating and thermocouple wires. Right: crucible design. (1) Tungsten crucible containing Ag; (2) Alumina spacer; (3) Ta filament; (4) Ta foil heat shields; (5) Mechanical shutter; (6) Thermocouple; (7) Water cooling.

4 Effusive Ag source

As described in Ch. 2, we need to be able to apply a capping layer *in vacuo*. To this end, we use an effusive source, following a design from the MMN group at the Department of Applied Physics of TU/e. Its design is shown in Fig. 4.6. The Ag is contained inside a W crucible from which it can evaporate through a 2 mm diameter orifice. The crucible is heated using a 5 Ω Ta filament wound through an alumina spacer. The crucible temperature can be measured using a K-type thermocouple, which is spring-pressed to the bottom of the W crucible. The hot interior of the source is insulated from the outside world using a stack of Ta foil heat shields. The hollow stainless steel outer shell of the Ag source provides water cooling. A mechanical shutter controls the Ag flux out of the source.

We perform a flux calibration to check the accuracy of the temperature measurement by the thermocouple. For this purpose, we use a quartz crystal microbalance (McVac MCM-160). The results of these measurements are shown in Fig. 4.7, along with a calculation based on literature values for the vapor pressure of silver [4] and the known source geometry. As can be seen, the thermocouple temperature accurately represents the effective source temperature. We typically operate the source at 3.5 A, 25 V, and 800 $^{\circ}\text{C}$, for an Ag deposition rate of around 1 $\text{\AA}/\text{min}$.

OPTICAL SYSTEM

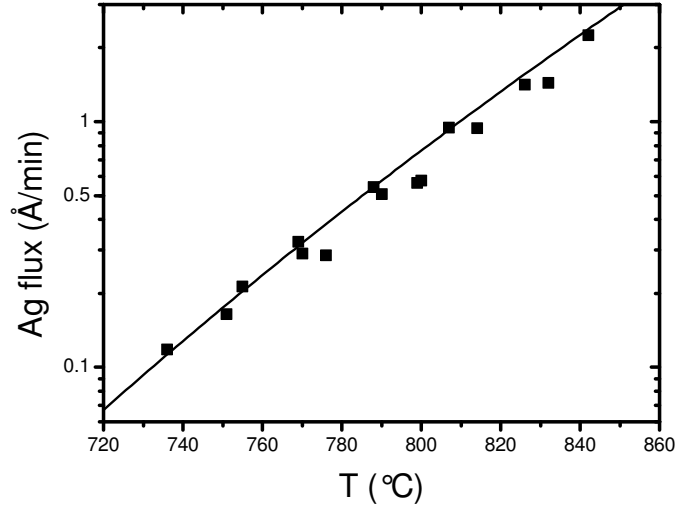


Figure 4.7: Flux calibration of the Ag source. Squares: measurements. Line: theoretical prediction.

5 Optical system

Our experiment requires an extensive optics setup, which we describe below. We begin by detailing the laser system we use to generate light at 372 nm, after which we proceed to describe the stabilization of the laser. Finally, we describe the light mask. As mentioned before, the lithography setup is sensitive to alignment errors. We will assess these in the following. More details on the laser system and the frequency stabilization can be found in Ref. [5].

5.1 Laser system

For laser cooling and focusing of Fe, we estimate that, at maximum, a laser power of about 500 mW is necessary [6]. There are no commercial systems capable of delivering 500 mW at 372 nm. To obtain light of the right wavelength, we have frequency doubled a commercially available Ti:S laser operating at 744 nm, using a doubling system built at the Free University of Amsterdam.

Frequency doubling is based on the nonlinear susceptibility of certain materials. The quadratic part of the response to an input at frequency ω can be Fourier expanded into a DC component and a component at frequency 2ω . Thus, on transmission of light, the crystal will produce radiation at the second harmonic frequency of the incident light. A full mathematical treatment [7] of the problem also yields a quadratic dependence of second harmonic output intensity on the input intensity. Written in terms of power:

$$P_{2\omega} = K \times P_{\omega}^2. \quad (4.4)$$

The nonlinear crystal we use to obtain the second harmonic is Lithium Triborate (LBO). In order to maximize the intensity of the fundamental passing through the

EXPERIMENTAL APPARATUS

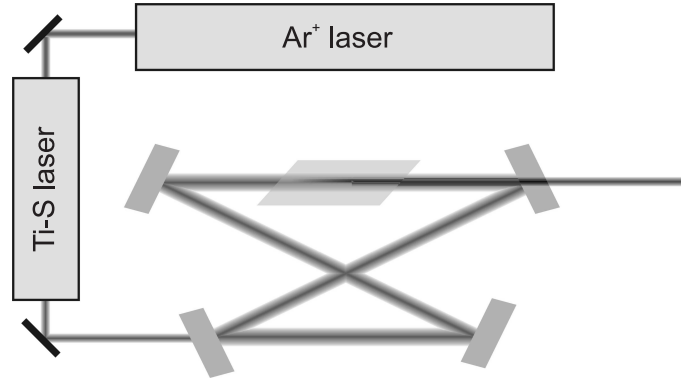


Figure 4.8: Laser system for Fe atom lithography. Laser light at 744 nm is generated from multi-line green light in a tunable Ti:S laser. It is fed into a ring cavity with an LBO crystal in it. In the crystal, frequency doubled light at 372 nm is generated.

crystal, the crystal is placed in a ring cavity as shown in Fig 4.8. The ring cavity consists of four mirrors, three with a power reflection coefficient $R = 0.999$ and one with $R = 0.99$. The Ti:S laser light enters the cavity through the $R = 0.99$ mirror. The cavity length was locked to the incoming laser light wavelength with the use of the Hänsch-Couillaud technique [8]. The maximum value of the cavity's finesse without crystal was calculated at 500.

The laser system's UV output power critically depends on the finesse of the cavity, which was determined from transmission measurements to be 177 ± 6 . The cavity increases the laser power inside it by a factor of 90, and thus increases the 372 nm output power by a factor of 8100. The power output at 372 nm proved to depend quadratically upon the input power into the cavity, with a conversion efficiency coefficient $K = 2.20 \pm 0.05 \times 10^{-4} \text{ mW}^{-1}$. This enables the laser system to produce over 800 mW of 372 nm laser light if pumped with 2 W of red light. On a regular basis, 300 mW of light is produced at 1.4 W pump power.

5.2 Frequency stabilization

Having obtained the necessary output power at 372 nm, we need a way to lock the laser wavelength to the wavelength of the ${}^5\text{D}_4 \rightarrow {}^5\text{F}_5$ atomic transition. To do this, we use polarization spectroscopy [9] of this transition. We need atomic Fe to observe this transition. In our setup, we generate the Fe atoms by sputtering from the cathode of a hollow cathode discharge. We applied polarization spectroscopy to this discharge. In polarization spectroscopy, Doppler broadening of the absorption profile is compensated for [9]. This theoretically enables us to obtain an error signal with a peak-to-peak width determined by the natural linewidth of the transition, $\Gamma/2\pi = 2.58 \text{ MHz}$ for our target transition.

The iron density and temperature inside the hollow cathode discharge were measured by absorption spectroscopy. The absorption dip had a FWHM of 1.00 GHz and an amplitude of about 40 %. The temperature was deduced from the Doppler width

OPTICAL SYSTEM

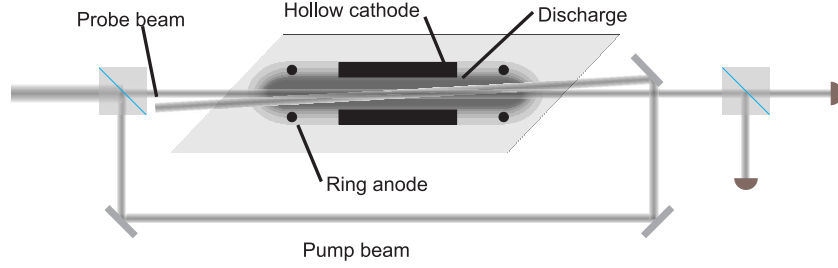


Figure 4.9: Polarization spectroscopy setup. Pump beam introduces birefringence in the iron discharge. The effect of this birefringence on the polarization of a counter propagating probe beam is analyzed using two photodiodes (right).

of the absorption dip to be 673 ± 6 K. From the intensity of the absorption dip, the iron atomic density in the discharge was estimated at $3.2 \pm 0.2 \times 10^{16} \text{m}^{-3}$.

We use polarization spectroscopy to lock the laser to the atomic transition frequency. In polarization spectroscopy, a pump laser at the same frequency, but of different polarization, induces a Doppler-free birefringence in the Fe gas. By measuring this birefringence, we obtained a dispersive error signal with a peak-to-peak width of 40 MHz. Using this error signal, we are able to limit the frequency drift of the laser system to to 0.2 MHz. The typical difference between the laser frequency and the resonance frequency is determined by the line width of the Ti:S laser, which is about 1 MHz.

5.3 Laser cooling

Atom lithography requires a collimated atom beam. The use of laser cooling permits to achieve this without the excessive flux loss caused by the use of apertures. The introduction to this thesis contains a brief theoretical outline of Doppler cooling. A thorough description of the laser cooling of atomic Fe is given elsewhere [10].

The laser cooling section runs from the 60 mm long laser cooling section starts 120 mm behind the source nozzle. The cooling beams are typically set to a saturation parameter of 1.5, at a detuning of -2Γ . A 10 mW resonant laser beam runs 1.20 m behind the source nozzle; the fluorescence of the Fe beam can be imaged using a CCD camera.

Figure 4.10 displays some typical results of the laser cooling. Left, the profile of the uncooled beam is determined mainly by the geometry of the setup. The cooled atom beam shows a very different profile, which is peaked at the position where the nanostructures are to be deposited. Center, the ratio of the cooled and uncooled beam intensities peaks to about 1.8. Thus, apart from the collimation-related improvement in nanostructure contrast, the local deposition rate will almost double. Overall, about 22 % of the Fe flux is lost to the leak in this image. Right, images of the beam collimation measurements taken using the $10 \mu\text{m}$ slit. The center line flux gain is also 1.8. The divergence of the beam decreases from 0.35 mrad RMS in the uncooled case to 0.25 mrad in the cooled case.

EXPERIMENTAL APPARATUS

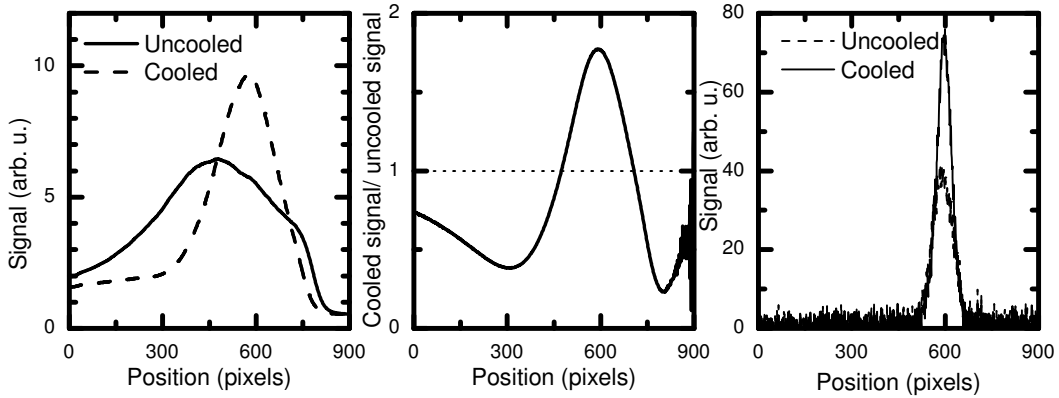


Figure 4.10: Laser cooling of Fe. Left: the uncooled beam profile (solid line) compared to the cooled beam profile (dashed line). Center: ratio of cooled to uncooled beam intensities. Right: beam collimation measurements using a 10 μm slit.

For an atom beam traveling at 1000 m/s, this divergence is equivalent to a residual transverse velocity distribution with a Gaussian width of 0.25 m/s. Had the cooling transition been closed, its Doppler limit would be 0.1 m/s. The difference between the observed collimation and the Doppler limit can be attributed to two factors: the leak in the transition and the finite laser line width. The intensity increase of 1.8 is a meager result compared to the factor 6 or so that is typically achieved by closed-system laser cooling. The main reason for this discrepancy is the leak in the transition. However, despite being clearly non-ideal, the collimation and flux of the Fe atom beam are still sufficient for atom lithography.

5.4 Light mask

We use light from the laser system described above to create the light mask. As the light mask must be detuned from resonance to suppress spontaneous emission, we use an acousto-optic modulator (AOM) to shift the laser beam frequency by 150 MHz - about 58 natural line widths. The ideal alignment of the light mask is shown schematically in Fig. 4.11(a). The light mask is perfectly perpendicular to both the atom beam and the mirror, and the Gaussian waist is exactly on the mirror surface.

One obvious alignment error in the light mask would be for the laser beam not to impinge perpendicularly on the retro-reflecting mirror, as shown in Fig. 4.11(b). The most dramatic effect of this error would be for the incoming and retro-reflected beam not to overlap. This would require a huge misalignment of 50 mrad, as the beam size is $\sim 50 \mu\text{m}$, and the propagation distance is $\sim 1 \text{ mm}$. Another effect of this misalignment is a change in standing wave period; the standing wave fronts are always parallel to the mirror. If the laser beam is oriented at an angle θ_i to the surface normal of the mirror, the resulting standing wave will have period $\cos \theta_i \times \lambda/2$. Thus, the relative deviation of the period from $\lambda/2$ is approximately $1/2 \theta_i^2$. In our setup, it is easy to align the laser beam so that $\theta_i < 1 \text{ mrad}$ by overlapping the

OPTICAL SYSTEM

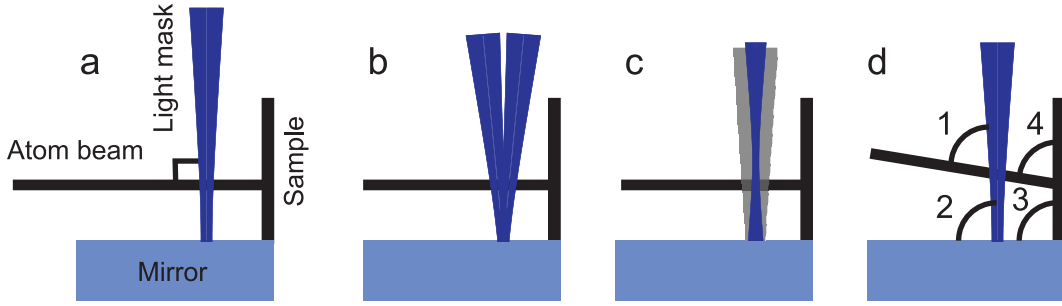


Figure 4.11: Alignment of the deposition setup. (a) Ideal alignment. (b) Laser not perpendicular to mirror. (c) Beam waist not on mirror. (d) Atom beam not perpendicular to light mask.

incoming and reflected laser beams. The resulting error in standing wave period is then approximately 10^{-4} nm.

The light mask should also be aligned so that both the mirror and the atom beam are well within the Rayleigh length [11] of the focus to minimize wavefront curvature (cf. Fig. 4.11(c)). The Rayleigh length for this focus is 16 mm, which means that we should position the lens so that the focus is within ± 10 mm of mirror, which is easy. As the distance between mirror and atom beam is fixed at 1 mm, this resolves both these alignment issues.

The most pressing alignment problem by far is posed by the small angular acceptance of the atom lenses. In the case of a misalignment between atom beam and light mask, the situation becomes that shown in Fig. 4.11 (d). The laser beam as it arrives at the vacuum setup measured $0.8 \times 0.9 \text{ mm}^2$. Assuming that the lenses are effectively 100 nm wide, a 1 mm thick atom lens has an angular acceptance of 10^{-4} rad, meaning that all atoms must impinge perpendicularly on the light mask to within this angle. As this level of collimation and alignment of the atom beam is hardly feasible, we reduce the beam waist at the location of the light mask using a lens. The focal length of the lens is $f=200$ mm, resulting in a measured beam waist of $45 \pm 1 \mu\text{m}$, and a tolerance of 2 mrad.

In Fig. 4.11 (d), the angle that requires a careful alignment is angle 1, which cannot be measured directly. Regardless of whether the laser beam is actually perfectly perpendicular to the mirror, the standing wave wave fronts will be parallel to the mirror surface. Hence, we can assume that angle 2 is $\pi/2$. As, in our sample holder-mirror assembly, the sample is mounted rigidly relative to the mirror, angle 3 can be measured and adjusted *ex situ*. We ensure that its deviation from perpendicular is less than 0.5 mrad. The atom beam is now perpendicular to the light mask (angle 1 = $\pi/2$) if it is perpendicular to the sample (angle 4 = $\pi/2$).

The atom beam direction is defined by two apertures. The first aperture is the hole in the skimmer, and the second aperture is in a dummy sample also used to align the laser cooling. We align a He:Ne laser so that it passes through both apertures, and then use the specular reflection off a Si sample to perform this alignment. The sample can be adjusted by rotating the vacuum flange the sample holder assem-

EXPERIMENTAL APPARATUS

bly is attached to - the angle between the sample and the atom beam in the other direction is not critical. The remaining aberration from perpendicular of angle 4 is estimated around 0.3 mrad. This can only be done if the entire vacuum is brought up to atmosphere. However, repeated sample exchanges showed that the alignment of the standing light wave is preserved from sample to sample to within 0.3 mrad. This means that the alignment procedure does not have to be repeated between depositions.

6 Conclusion

In conclusion, we have constructed and tested a setup for atom lithography of Fe. This setup allows for atom lithography in a clean environment, corrosion protection of the atom lithography setup, and a relatively high production rate of several samples per day. It can also be used to investigate the influence of substrate conditions on the diffusion and growth of the nanostructures. Adapting the light mask geometry only requires changing the sample holder. This is a unique versatility that is not seen in other atom lithography setups.

Adapting the setup to fit other materials would not take a large amount of effort, provided that the laser wavelength needed is not too far from that of Fe. In this case, exchanging the crucible in the Fe source with one containing the desired element, replacing the nonlinear crystal in the cavity, and using a different hollow cathode for the frequency stabilization suffices.

References

- [1] T. I. Gombosi, *Gaskinetic theory* (Cambridge University Press, Cambridge, 1994)
- [2] R. C. M. Bosch, H. C. W. Beijerinck, P. van der Straten, and K. A. H. van Leeuwen, *Eur. Phys. J. A. P.* **18**, 221-227 (2002)
- [3] H. Metcalf and P. van der Straten, *Laser Cooling and Trapping* (Springer Verlag, Heidelberg, 1999).
- [4] A. N. Nesmeyanov, *Vapor pressure of the chemical elements*, Elsevier (1963)
- [5] B. Smeets, R. C. M. Bosch, P. van der Straten, E. te Sligte, R. E. Scholten, H. C. W. Beijerinck, and K. A. H. van Leeuwen, *Appl. Phys. B*, **76**, 815-819 (2003)
- [6] R. C. M. Bosch, PhD thesis, TU/e (2002)
- [7] Y. R. Shen, *The Principles of Nonlinear Optics*, J. Wiley (1984)
- [8] T. W. Hänsch and B. Couillaud, *Opt. Comm.* **35**, 441-444 (1980)
- [9] W. Demtröder, *Laser Spectroscopy, Basic Concepts and Instrumentation*, Springer-Verlag (1981)

CONCLUSION

- [10] B. Smeets, R. W. Herfst, L. P. Maguire, E. te Sligte, P. van der Straten, H. C. W. Beijerinck, and K. A. H. van Leeuwen, manuscript submitted to *Applied Physics B*
- [11] F. L. Pedrotti and L. S. Pedrotti, *Introduction to Optics*, Prentice-Hall (1987)

EXPERIMENTAL APPARATUS

Chapter 5

Deposition experiments

We have used the setup described previously to deposit Fe nanolines and thin films. In this chapter, we describe the deposition procedure, the nanostructures deposited, and some preliminary measurements on the magnetic properties of the thin films we deposit. Preliminary experiments, which resulted in lower, but otherwise similar structures, have been published in Ref. [1]. A similar experiment was performed independently at Radboud University at around the same time, resulting in broader, but also higher structures [2].

1 Procedure

The low Fe flux that can be obtained from our Fe source forces us to use long deposition times. At a 2 nm/h deposition rate, we need to deposit for hours to get a reasonable layer thickness. We therefore use a fixed deposition time of two hours. LIF measurements of the laser cooled beam flux before and after the deposition runs often revealed a significant decline in Fe flux during a deposition, up to a factor 2. Hence, we do not deposit for longer times.

Additionally, the long deposition time proved to be problematic for the laser cooling section. The laser frequency stabilization with the hollow cathode discharge drifted slightly over this time scale; we suspect that this is due to slow drifts in the magnetic field inside the Fe hollow cathode discharge. The frequency drifts were of the order of the natural line width, corresponding to magnetic field drifts of a few Gauss. This drift is too much for reliable laser cooling. The ferromagnetic hollow cathode makes influencing the magnetic field inside the hollow cathode discharge virtually impossible. The drift was not so much as to ruin the laser cooling, just enough to alter its results significantly.

Motivated by this problem, but also driven by an interest in novel applications of atom lithography, we decided not to apply laser cooling during the deposition experiments, but rely on the geometrical collimation resulting from the source aperture instead. To the authors' knowledge, this is the first experiment in which direct-write atom lithography has been attempted without laser cooling. The range of elements

DEPOSITION EXPERIMENTS

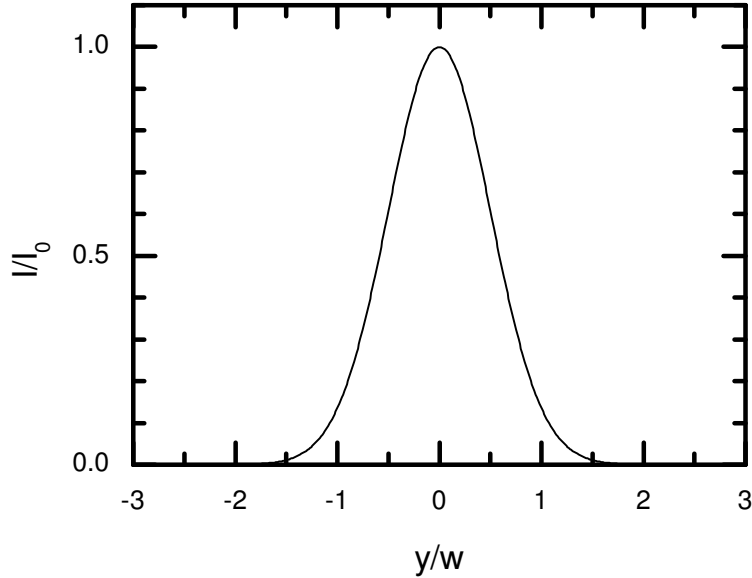


Figure 5.1: Intensity profile of the light mask. One deposition run covers all intensities less than or equal to the center line intensity.

to which atom lithography can be applied increases dramatically if the demand for a closed laser cooling transition can be dropped.

The light mask is detuned either positively or negatively from resonance using an AOM driven at 150 MHz. The frequency drift of the laser system is small on this scale. An estimate of the optimum focusing power for Fe in a circular Gaussian light mask is around 10 mW [3]; we use a much larger amount of power in the light mask to capture the entire power dependence in a single experiment. The principle is shown in Fig. 5.1. A Gaussian intensity profile contains all intensities below the central intensity I_0 . As the waist of the Gaussian in one direction does not depend on the position in the other direction, this effectively means that the experiment is done for all powers below a certain maximum power. Hence, our analysis of the experiments will be carried out as a function of the directly measured y -position on one sample, rather than as a function of the total beam power on numerous different samples. The standard total beam power will be set at 50 ± 5 mW. The alignment of the light mask with respect to the sample is such, that 90 % of the running wave power is retroreflected by the mirror, and 10 % is scattered by the sample. This positions the sample at $z = +0.9w$. After the deposition, no capping layer was applied, as our interest is in the deposition process for the time being.

2 Fe nanolines

We obtained nanostructures with a height of a few nm, a period of 186 nm and a FWHM of typically 50 nm. The nanostructures were found to extend over a range of 0.4 mm in the direction of the lines. This is unexpectedly large, as the waist radius of

FE NANOLINES

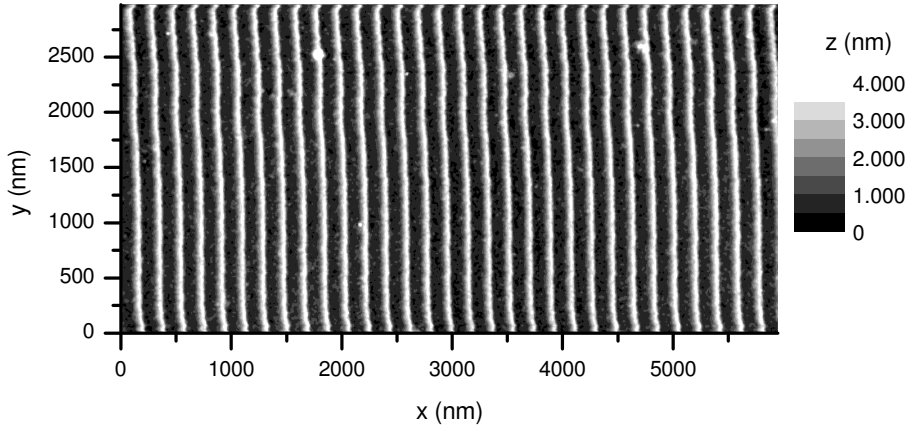


Figure 5.2: AFM scan of Fe nanolines deposited by atom lithography.

the light mask was only 0.05 mm. An Atomic Force Microscope (AFM) scan of some of these structures is shown in Fig. 5.2. The highly periodic nature of the structures is immediately apparent. The slight wavering of the lines is most likely due to drifts of the AFM piezos, as the same sample area looks slightly different for every scan.

We quantify the properties of the nanostructures by averaging ten lines of an AFM scan. This yields a structure profile as shown in Fig. 5.3. The data are represented by squares, and the drawn line represents a Gaussian fit. The width and height of all nanostructures discussed in this thesis have been extracted from similar Gauss fits. The asymmetry that is apparent in the peak shape is possibly an artifact caused by *e.g.*, the shape of the AFM tip, or the AFM electronics. It could also be caused by an effect in the deposition process, such as a misalignment.

Curiously, we initially measured a period that differed significantly from the nominal value of 186.05 nm, initially by over 20 %. To decide whether something was wrong in the deposition process or in the AFM calibration, we used a sample that had been treated atom lithographically with He* at the Free University of Amsterdam [8]. The nominal period of these structures is 541.5 nm, half the wavelength of the 1083 nm transition used in the experiment. The ratio of the two periods is 2.91; with the AFM, we measured 2.87 ± 0.06 . This excellent agreement was used for a re-calibration of the AFM. For all further scans, we used the measured nanostructure period as a length scale, which was set at 186 nm.

Scanning over y , we obtain an image of the power dependence of the characteristics of the lines, and hence the deposition process. For positive detuning, this measurement is shown in Fig. 5.4. The width of the lines is shown on the left; the full width at half maximum (FWHM) of the nanolines is around 50 nm for all locations where the nanolines can be clearly discerned. The height of the nanolines (on the right) increases towards the center of the profile.

Similar measurements were performed for negative detuning. Due to a disappointing overall Fe flux, these experiments have not yet yielded satisfactory data for a proper analysis. However, it did become clear that the nanolines deposited at neg-

DEPOSITION EXPERIMENTS

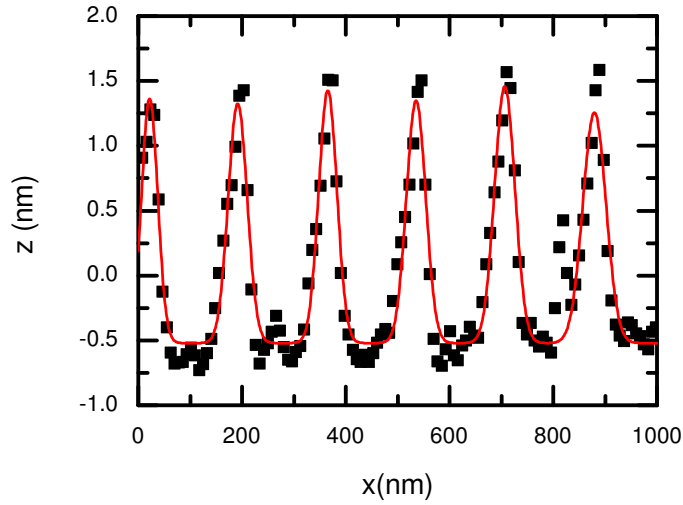


Figure 5.3: Line profile of nanolines. Squares: data. Line: Gaussian fit.

ative detuning were consistently broader than those deposited at positive detuning. The narrowest features found for $\Delta < 0$ had a FWHM of 68 ± 8 nm.

For a clear comparison, we have analyzed the results of our simulations in the same manner. The results are shown in Fig. 5.5. The horizontal axis here spans only one half of the total extent of the light mask, as the simulation results are assumed symmetric. The left plot shows the FWHM of the nanostructures for both positive and negative detuning.

In the case of positive detuning, the FWHM of the nanostructures is typically between 50 and 60 nm; it only begins to increase when the intensity is reduced by at least a factor 100 at $y = 1.5w$. Furthermore, the height of the nanostructures decays far more rapidly. The simulated nanostructure height is reduced to around 10 % of its maximum at $y = 1.5 w$, which corresponds roughly to the visibility limit of the AFM measurements. This behavior is consistent with the line focusing image developed in Chapter 3.

For the case of negative detuning, the nanoline width clearly displays an optimum. The minimum width achieved is 71 ± 3 nm, in good agreement with the measured value. The nanoline height also betrays reduced focusing quality at high intensities. The distinct optimum in feature width can be understood by recalling that the light mask acts as a parabolic lens for negative detuning (cf. Ch. 3).

The simulations only predict nanostructures in an area between $\pm 1.5 w$; with a measured beam waist of $45 \mu\text{m}$, this corresponds to lines that are ~ 0.15 mm long. The most likely explanation for the large extent of the nanolines is the non-Gaussian beam profile of the laser beam. Although the central intensity peak is Gaussian to a good approximation, the intensity of the laser light was observed to decay relatively slowly compared to an ideal Gaussian profile. The intensity in this region was up to about 10 % of the central intensity, enough to affect the atom beam.

FE NANOLINES

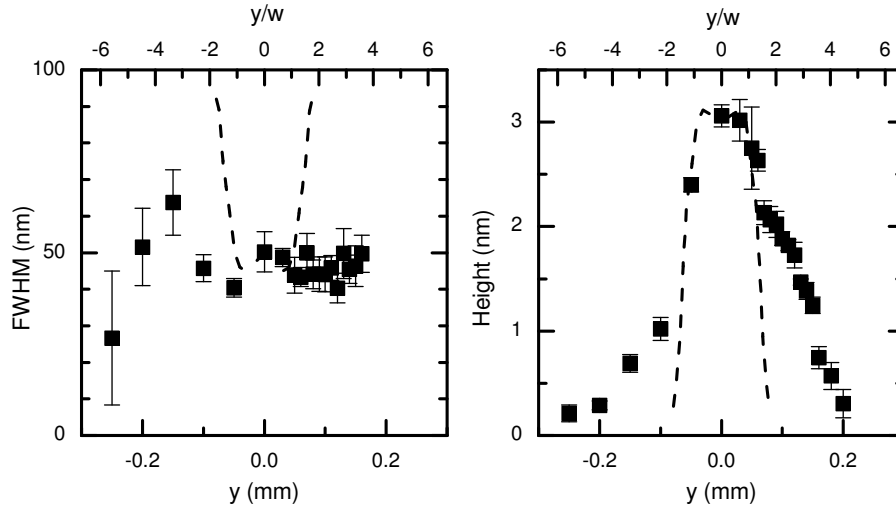


Figure 5.4: Measured width (left) and height (right) of nanolines as a function of y position for positive detuning. Dashed lines: simulated data.

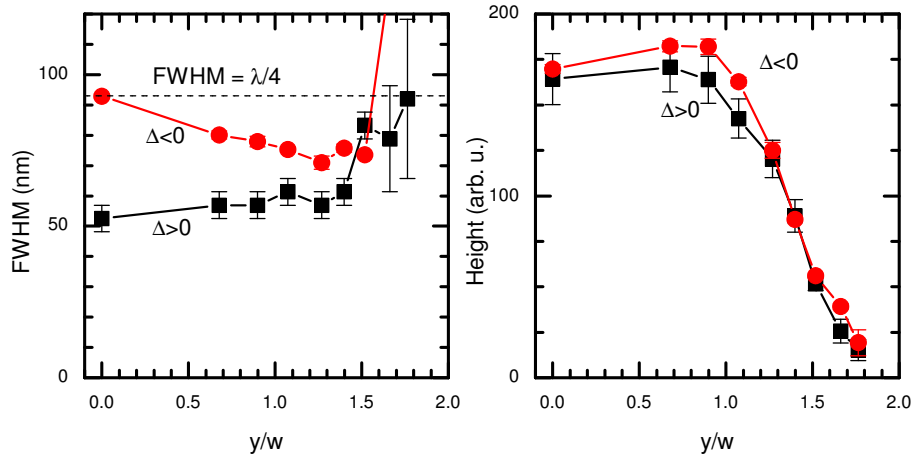


Figure 5.5: Simulated width (left) and height (right) of nanolines as a function of y position. Squares: $\Delta > 0$. Circles: $\Delta < 0$. Running wave power: 50 mW; beam waist: 50 μm .

DEPOSITION EXPERIMENTS

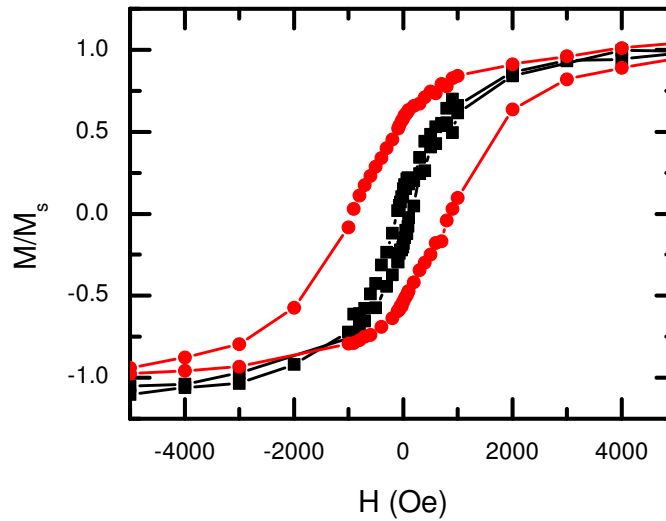


Figure 5.6: Hysteresis curves of Fe layers deposited on an Ag substrate (squares) and on a Si substrate (circles). Both were protected against corrosion with an Ag capping layer.

3 Magnetism of thin films

For a preliminary investigation of the magnetic properties of the Fe deposited in the course of these experiments, some samples were covered with simple Fe layers. These samples were investigated using a Superconducting Quantum Interference Device (SQUID) magnetometer in the FNA group of Koopmans [4].

Figure 5.6 shows the in-plane hysteresis curves of two Fe thin films. One Fe film was deposited directly onto the native oxide substrate (circles), while the other film was deposited on a native oxide substrate prepared by covering it with a 6 ± 1 nm Ag film (squares). Both samples were covered with a 6 ± 1 nm Ag capping layer before being removed from the sample. Due to the unreliability of the Fe source at the time of this experiment, the exact Fe flux is not known. However, we do know from LIF measurements that the Fe flux deposited on the bare sample is 0.75 times that deposited on the Ag-covered sample.

Obviously, both samples exhibit ferromagnetism. From the hysteresis curves, we determine the coercivities, remanences, permeabilities and magnetic moments of the samples. The coercivity of the ferromagnetic layer on the uncoated sample is 900 Oe, whereas that of the Ag-coated sample is only 100 Oe. Also, the silver underlayer reduces the remanence from $0.8 M_s$ to $0.2 M_s$. As bulk iron is a soft ferromagnet, with low remanence, we conclude that the presence of the oxide somehow hampers the 'normal' ferromagnetic behavior of the film. The total ferromagnetic moment of the Ag-substrate sample was 4.4×10^{-6} emu, that of the native oxide sample was 14.4×10^{-6} emu.

The magnetic moments of the two films differ dramatically; accounting for the slightly different deposition times, the native oxide sample has a magnetic moment *per atom* that is 4.4 times greater than that of the Ag sample. Assuming that the

magnetization of the layers is the same as that of bulk Fe, the thickness of layer on the native oxide sample is approximately 2 nm; the layer on the Ag-covered sample would then be some 0.7 nm thick. From general knowledge of the source's performance, we expect the layer thickness to be in the several nanometers. The anomalously low effective magnetization of the Ag-Fe-Ag sandwich could be caused by a variety of growth phenomena, such as island formation [5] in either the Ag or Fe films, or burrowing of the Fe atoms into the Ag layer [6]. Both could in principle affect the morphology of the Fe films and reduce the effective amount of ferromagnetic material, especially for the very thin films under consideration here.

Comparing the properties of the Fe film on the Ag-coated sample to literature values, we find that the magnetic permeability of the material may be estimated at 20 ± 2 . The permeability of high-purity Fe (99.9 %) can be up to 25000, whereas that of commercial Fe (99 %) is typically around 200 [7]. The permeability of a material is determined largely by the density of obstacles to domain wall motion. Thus, the lower its permeability, the more impurities a material contains. Apparently, the Fe layers deposited here are not very pure. This is to be expected, as the deposition chamber is at $\sim 10^{-7}$ mbar.

The large difference in hysteresis between the coated and uncoated samples cannot be explained by the composition of the material, as that is identical for both samples. It may well be caused by exchange biasing or growth effects. Oxidized Fe atoms can be part of an (anti-)ferromagnetic state present at the oxide-iron interface. This anti-ferromagnetic medium does not have a net moment in the absence of an applied field; as a result, its interaction with the field is far weaker. Thus, it is considerably more resistant to magnetization reversal. As there is an exchange interaction between the antiferromagnetic phase and the ferromagnetic phase, this hampers domain wall motion, provided that the ferromagnetic film is of a suitable thickness [9].

Which substrate we use for magnetic experiments depends on the experiment. If we aim to investigate the magnetic anisotropy of the nanostructures, a soft ferromagnet is better. Thus, it may be desirable to deposit the nanostructures on a silver layer. For magnetic recording type experiments, the larger the coercivity, the better the stability, and thus the native oxide substrates would be better suited.

References

- [1] E. te Sligte, B. Smeets, K. M. R. van der Stam, R. W. Herfst, P. van der Straten, H. C. W. Beijerinck, and K. A. H. van Leeuwen, *Appl. Phys. Lett.* 85, 4493-4495 (2004)
- [2] G. Myszkiewicz, J. Hohlfeld, A. J. Toonen, A. F. van Etteger, O. I. Shklyarevskii, W. L. Meerts, and Th. Rasing, *Appl. Phys. Lett.* 85, 3482-3484 (2004)
- [3] J. J. McClelland, *J. Opt. Soc. Am. B* 12, 1761-1768 (1995); we estimate the average Clebsch-Gordan coefficient at $1/2$.
- [4] Measurements performed by C. J. P. Smits

DEPOSITION EXPERIMENTS

- [5] J. Oster, M. Huth, L. Wiehl, and H. Adrian, *J. Magn. Magn. Mater.* **272-276**, 1588-1589 (2004)
- [6] D. E. Bürgler, C. M. Schmidt, D. M. Schaller, F. Meisinger, R. Hofer, and H.-J. Güntherodt, *Phys. Rev. B* **56** 4149-4158 (1997)
- [7] *CRC Handbook of Chemistry and Physics*, 79th Ed. (CRC Press, Boca Raton, 1998)
- [8] Samples courtesy of W. Vassen
- [9] J.-G. Hu, G.-J. Jin, and Y.-Q. Ma, *J. Appl. Phys.* **94**, 2529-2533 (2003)

Chapter 6

Magnetism of periodic nanostructures

The reason for using Fe in our atom lithography experiment was the fact that it is ferromagnetic. We therefore desire to investigate the magnetic properties of the nanostructures we have deposited. In the last chapter, we have proven the ferromagnetic nature of the material we deposit. The next step is to find a signature of the nanostructured nature of the deposited layer.

The simplest analysis technique available is the magneto-optical Kerr effect (MOKE), which investigates the reflectivity of the magnetic material to discern signs of ferromagnetism [1]. Varying the applied magnetic field in both size and direction allows for detection of magnetic anisotropy. This involves a laser, and its resolution is thus limited by the spot size of the laser beam. Hence, the technique can only investigate the properties of the nanostructured material averaged over many lines.

A large amount of theoretical [2] and experimental [3] work has been done on ferromagnetic nanowire arrays. However, most of this work concerns two-dimensional arrays of nanowires which have been obtained by electrodepositing the metal in a matrix. The results cannot be straightforwardly translated to the present work. A better match is provided by one-dimensional arrays of nanowires made using electron beam lithography [4]. These are typically arrays of wires with a rectangular cross-section, which are also different from the continuous modulated thin films we investigate. We would be interested primarily in the effect of the modulation of the surface shape of our thin film, which we expect to show up as an anisotropy in the direction that is perpendicular to the nanolines and in the substrate plane.

This chapter will present some considerations on the magnetic anisotropy of the ferromagnetic nanostructures produced in this thesis. To this end, we begin by introducing the magnetic field generated by a magnetization distribution, also known as the demagnetizing field. We describe the magnetostatic energy terms that can play a role in the anisotropy of the nanostructures in section 2. The model we use to investigate the anisotropy is introduced in section 3. The resulting stray fields are presented in Sec. 4; the ensuing anisotropy is discussed in Sec. 5. We conclude with a summary of further potential experiments.

1 Demagnetizing field

A magnetized object will generate a magnetic field that normally extends outside the object itself. This field is called the demagnetizing field, and it can be calculated using Maxwell's equations. These relations between electric field \vec{E} , magnetic induction \vec{B} , charge density ρ , and current density \vec{J} can be found in any textbook [5, 6] and read:

$$\begin{aligned}\nabla \cdot \vec{E} &= \frac{\rho}{\epsilon_0} \\ \nabla \times \vec{E} &= -\frac{\partial \vec{B}}{\partial t} \\ \nabla \cdot \vec{B} &= 0 \\ \nabla \times \vec{B} &= \mu_0 \vec{J} + \mu_0 \epsilon_0 \frac{\partial \vec{E}}{\partial t}\end{aligned}\tag{6.1}$$

By definition, the magnetization \vec{M} is such, that:

$$\vec{B} = \mu_0 (\vec{M} + \vec{H}).\tag{6.2}$$

Inserting this into Maxwells equations, we get:

$$\begin{aligned}\nabla \cdot \vec{E} &= \frac{\rho}{\epsilon_0} \\ \nabla \times \vec{E} &= -\mu_0 \frac{\partial \vec{H}}{\partial t} - \mu_0 \frac{\partial \vec{M}}{\partial t} \\ \nabla \cdot \vec{H} &= -\nabla \cdot \vec{M} \\ \nabla \times \vec{H} &= \vec{J} + \epsilon_0 \frac{\partial \vec{E}}{\partial t} - \nabla \times \vec{M}\end{aligned}\tag{6.3}$$

Now let us begin by noting that the magnetization enters into the right hand side of these equations as a source term. Its divergence, for example, generates \vec{H} just as electric charge generates \vec{E} . This is why we introduce a magnetic charge density $\rho^* \equiv \mu_0 \nabla \cdot \vec{M}$, and a magnetic current density $\vec{J}^* \equiv \mu_0 \partial \vec{M} / \partial t$. The rotation of \vec{M} is effectively a bound current density, which can be removed from the equations by separating the current density \vec{J} into a magnetization-dependent part and a free current density according to $\vec{J} = \vec{J}_f + \vec{\nabla} \times \vec{M}$:

$$\begin{aligned}\nabla \cdot \vec{E} &= \frac{\rho}{\epsilon_0} \\ \nabla \times \vec{E} &= -\mu_0 \frac{\partial \vec{H}}{\partial t} - \vec{J}^* \\ \nabla \cdot \vec{H} &= -\frac{\rho^*}{\mu_0} \\ \nabla \times \vec{H} &= \vec{J}_f + \epsilon_0 \frac{\partial \vec{E}}{\partial t}\end{aligned}\tag{6.4}$$

The free current density is now the current density that results from the applied currents in the system. We now have a set of equations that can be used to calculate \vec{H} for any given magnetization configuration. This will be very useful later on. As a last remark, note that magnetic charge is every bit as conserved as electric charge, and that its total in all space must necessarily be zero.

The preceding showed that magnetic charge generates \vec{H} in exactly the same way that electric charge generates \vec{E} . Coulomb's law in integral form states that:

$$\vec{E}(\vec{r}) = \frac{1}{4\pi} \int \frac{\vec{r} - \vec{r}'}{|\vec{r} - \vec{r}'|^3} \frac{\rho}{\epsilon_0} d^3 \vec{r}'.\tag{6.5}$$

In the absence of free currents, the analogous formula for calculating \vec{H} is:

$$\vec{H}(\vec{r}) = \frac{-1}{4\pi} \int \frac{\vec{r} - \vec{r}'}{|\vec{r} - \vec{r}'|^3} \frac{\rho^*}{\mu_0} d^3\vec{r}' \equiv \vec{H}_d(\vec{r}). \quad (6.6)$$

This field is called the demagnetizing field \vec{H}_d . As it is generated only by the magnetization of an object, it is the only non-vanishing field when all external field sources are removed. This is typically the field that a Magnetic Force Microscope (MFM) seeks to detect [9].

2 Energy of ferromagnetic nanostructures

The energy of ferromagnetic nanostructures has several terms. We will first briefly describe them, before going into the calculation of their contributions.

An external applied field obviously has an interaction with the magnetic nanostructure, and this is by far the simplest of the energy terms under consideration here. The applied field energy density is given by:

$$E_a = -\mu_0 \vec{H}_a \cdot \vec{M}. \quad (6.7)$$

For an applied field of 1000 Oe, this energy density can be up to 172 kJ/m³ for iron.

2.1 Exchange energy

The exchange interaction is the quantum mechanical effect that underlies all magnetic ordering. It is caused directly by the Pauli principle, which states that the total wave function of a set of identical fermions is anti-symmetric [7]. Suppose two electrons have the same spin orientation and therefore a symmetric spin wave function. Then their spatial wave function must be asymmetric, meaning that their chance of being at the same place at the same time becomes zero. For two electrons with opposite spins, the spatial wave function is symmetric, allowing the electrons to be at the same place at the same time. Hence, the expectation value of the distance between them increases if their spins are parallel, and the strength of the repulsive Coulomb interaction between the two electrons decreases. The size of this effect is proportional to the overlap of the two electronic spatial wave functions. Thus, it is an electrostatic interaction that has a very short range. It is very strong between electrons at nearest-neighbor lattice sites, but generally negligible between non-nearest-neighbor lattice sites.

The energy density E_{ex} that results from the exchange interaction is given by [8]:

$$E_{ex} = A_{ex} \left(\nabla \frac{\vec{M}}{|\vec{M}|} \right)^2 = A_{ex} [(\nabla \cos \alpha_x)^2 + (\nabla \cos \alpha_y)^2 + (\nabla \cos \alpha_z)^2], \quad (6.8)$$

where α_i is the angle between the magnetization and the i coordinate axis. For Fe, the value of the proportionality constant A_{ex} is 1.95×10^{-11} J/m [1]. Assuming that variations could occur at a length scale of ~ 10 nm, the resulting energy density is around 200 kJ/m³.

2.2 Crystalline anisotropy

The crystalline anisotropy field is due to the fact that a ferromagnetic solid crystal is not isotropic. For a cubic crystal, such as Fe, the energy difference between various orientations is dictated by the angle to the orthogonal crystal axes. The spins in Fe will normally align themselves along the crystal axes. The energy needed for a different orientation of the spins is given by [1]:

$$E_c = K_1[\sin^2 \alpha_1 \sin^2 \alpha_2 + \sin^2 \alpha_2 \sin^2 \alpha_3 + \sin^2 \alpha_1 \sin^2 \alpha_3]. \quad (6.9)$$

In this, α_i is the angle between the magnetization and the i th crystal axis. The proportionality constant K_1 depends on the crystal lattice. For Fe, $K_1 = 48 \text{ kJ/m}^3$ [1].

The nanostructures currently under consideration have been deposited on an amorphous SiO_2 layer. As such, we do not know whether they would preferentially crystallize with any specific orientation of the crystal axes. In addition, the slightly grainy texture of the nanostructure surface profile seems to indicate that the nanostructures are polycrystalline. If the crystals are oriented randomly, the resulting crystalline anisotropy energy should be independent of the orientation of \vec{M} . If they are not, the crystalline anisotropy is still the smallest of the terms under consideration. Hence, we neglect this term in the anisotropy model.

2.3 Dipole energy

The dipole energy finds its source in the interaction of the nanostructures with the demagnetizing field they generate. In the magnetic charge view, the form (but not the content) of Poynting's theorem changes. The electromagnetic power density is now given by [6]:

$$p = \vec{E} \cdot \vec{J}_f + \vec{H} \cdot \vec{J}^*, \quad (6.10)$$

which can easily be seen from the symmetry of the set of equations 6.4. If we assume that the free current density is zero everywhere, we can calculate the energy density needed to magnetize a material. This looks like:

$$E_d \equiv \int p \, dt = \int \vec{H} \cdot \vec{J}^* \, dt = \mu_0 \int \vec{H}_d \cdot \frac{\partial \vec{M}}{\partial t} \, dt. \quad (6.11)$$

Now, \vec{H}_d scales linearly with the overall magnitude of the magnetic charges that generate it (cf. Eq. 6.6). This charge distribution is nothing more than the divergence of \vec{M} . Hence, \vec{H}_d scales linearly with \vec{M} : $\vec{H}_d = \vec{N} \cdot \vec{M}$. The demagnetizing tensor \vec{N} only depends on the geometry. Thus, the integral becomes:

$$E_d = \mu_0 \int_0^{M_s} \vec{N} \cdot \vec{M} \cdot d\vec{M} = \frac{\mu_0}{2} \vec{H}_d \cdot \vec{M}_s \quad (6.12)$$

In the case that $|\vec{H}_d| = |M_s|$ in Fe, this energy density can reach 3.7 MJ/m^3 ; this occurs for out-of-plane magnetization of a thin film. In this work, values are likely to be a fraction of this, as we investigate the in-plane anisotropy of the nanostructures. For any given structure, calculating the total dipole energy is now a straightforward matter of integration.

3 Magnetic anisotropy model

We seek to calculate the applied field necessary to compensate the energy difference between the states with magnetization parallel and perpendicular to the nanolines, which we will dub the *anisotropy field* H_{an} . If the total magnetic energy of the nanostructure with perpendicular-but-in-plane magnetization in the absence of an external field is W , it can be found from:

$$H_{an} = \frac{W}{\mu_0 \int M_x d^3\vec{r}} \quad (6.13)$$

Conveniently, the energy of the state in which \vec{M} is parallel to the lines is zero in the absence of an applied field. As the magnetization is perfectly homogeneous, there is no exchange energy contribution; also, there are no charges inside the nanolines. Surface charges do not form as the magnetization is parallel to the surface everywhere.

For a magnetization perpendicular to the lines, there will generally be exchange and magnetic dipole contributions in addition to the applied field term. The magnetization configuration will be such that the total magnetic energy is minimized.

3.1 Description of the nanolines

As we are interested in the shape anisotropy of the nanolines, the model must first describe their shape. We assume that the nanolines are perfectly periodic, as the optical potential that focuses the atoms is perfectly periodic. The height of the structures is along the z -axis, and their modulation along the x -axis. We assume that the extent of the lines in the y -direction is infinite. The peak shape is chosen to be Gaussian, for mathematical simplicity. A picture of the assumed line shape is shown in Fig. 6.1. The Gaussian peaks of $1/e$ half width w and height h_1 sit atop a background layer of height h_0 . As we choose to normalize all distances to the nanostructure period, the analytical expression for the structure height as a function of x is:

$$h(x) = h_0 + h_1 \sum_{n=-\infty}^{\infty} \exp\left[-\frac{(x-n)^2}{w^2}\right] \quad (6.14)$$

Typical values for the nanolines under consideration in the present work are $h_0 = 0.02$, $h_1 = 0.02$, and $w = 0.2$.

We introduce dimensionless parameters for ease of calculation. The magnetization M of Fe is set to unity; this also serves as the unit of all magnetic fields H . All energy densities will be expressed in units of $\mu_0 M^2$. The magnitude of the magnetization can be considered constant [1], so we need only concern ourselves with its orientation. As the magnetization is perpendicular to the lines everywhere, \vec{M} can be written in terms of the angle α_x between the magnetization and the x -axis:

$$\vec{M} = M(\cos \alpha_x, 0, \sin \alpha_x). \quad (6.15)$$

Now, we can proceed to calculate the energy contributions of the various terms for any given $\alpha_x(x, z)$, and then deduce the anisotropy field of that configuration.

MAGNETISM OF PERIODIC NANOSTRUCTURES

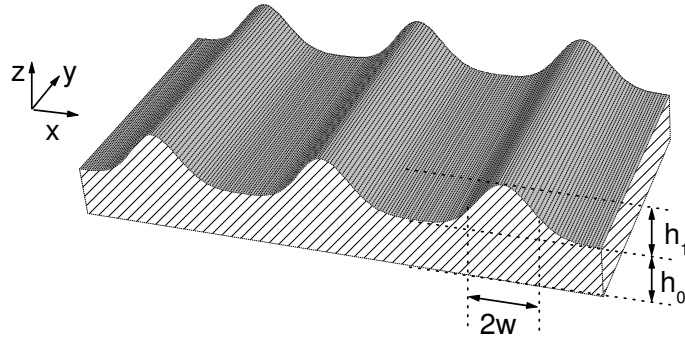


Figure 6.1: The nanolines are modeled as a series of Gaussian peaks on a background layer.

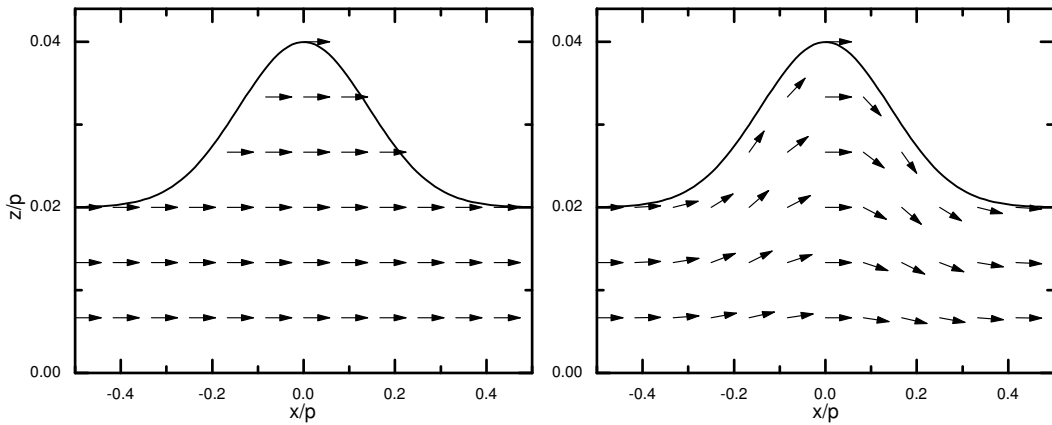


Figure 6.2: We investigate two magnetization configurations. Left: homogeneous magnetization generates only surface charge. Right: inhomogeneous magnetization generates no surface charge.

To find the true value of the anisotropy field, we must first find the configuration $\vec{M}(\vec{r})$ with minimal magnetic energy. This is an unwieldy problem, as the dipole energy density is expressed as an integral over all space. Instead of completely solving this problem, we confine ourselves to calculating the anisotropy for two instructive cases. The anisotropy values resulting from these calculations then place an upper limit on the true value of the anisotropy field.

Figure 6.2 shows the magnetization orientation of the two configurations. The first configuration chosen is homogeneous magnetization throughout the nanostructure, which will generate zero exchange energy, and limit the dipole interaction to fields generated by magnetic surface charges. We will dub this the surface charge (SC) scenario. We choose the second configuration so that it does not generate any surface charge, and is still relatively easy to handle analytically. This will be referred to as the volume charge (VC) scenario.

3.2 SC model

We now proceed on the assumption that the magnetization of the nanoline is homogeneous over the entire structure, and is oriented along the x -axis with $\alpha_x = 0$. This is the left configuration in Fig. 6.2. The surface charges are described by:

$$\rho^* = -\nabla \cdot \vec{M} = -\delta(z - h(x, y)) \vec{M} \cdot \vec{n} = \delta(z - h(x, y)) \frac{\frac{\partial h}{\partial x}}{\sqrt{1 + (\frac{\partial h}{\partial x})^2}}. \quad (6.16)$$

These expressions have been converted to the dimensionless units; the surface normal is referred to as \vec{n} . The h -dependent part of the expression is simply a sine. As we are looking for the anisotropy effect of the nanolines, we are interested mainly in the x -component of the demagnetizing field. It is given by:

$$H_x(x, y, z) = \frac{1}{4\pi} \iint \frac{\frac{\partial h}{\partial x'}(x')}{\sqrt{1 + (\frac{\partial h}{\partial x'}(x'))^2}} \frac{x - x'}{((x - x')^2 + (y - y')^2 + (z - h(x'))^2)^{3/2}} dx' dy', \quad (6.17)$$

or, after integrating out the y -dependence:

$$H_x(x, y, z) = \frac{1}{2\pi} \int \frac{\frac{\partial h}{\partial x'}(x')}{\sqrt{1 + (\frac{\partial h}{\partial x'}(x'))^2}} \frac{x - x'}{(x - x')^2 + (z - h(x'))^2} dx'. \quad (6.18)$$

Similarly, the z component of the demagnetizing field can be shown to be:

$$H_z(x, y, z) = \frac{1}{2\pi} \int \frac{\frac{\partial h}{\partial x'}(x')}{\sqrt{1 + (\frac{\partial h}{\partial x'}(x'))^2}} \frac{z - h(x')}{(x - x')^2 + (z - h(x'))^2} dx'. \quad (6.19)$$

Calculating the energy of the structure is simply the integral:

$$\frac{W}{\mu_0 M^2} = \frac{1}{2} \int H_x(\vec{r}) d^3 \vec{r}, \quad (6.20)$$

with the integration volume a cross-section of a nanoline over one full period by some arbitrary y -length. This integration can be carried out numerically without frustratingly large computation times.

3.3 VC model

We now explore another option, one that nulls the surface poles. The key physical assumption in this model is the energetic dominance of surface poles over all else. This assumption is made not because we believe it correct, but rather because we want to investigate the other energy terms separately from the surface energy. We impose the boundary condition:

$$\alpha(x, h(x)) = \arcsin \frac{\partial h / \partial x}{\sqrt{1 + (\partial h / \partial x)^2}}, \quad (6.21)$$

MAGNETISM OF PERIODIC NANOSTRUCTURES

where $h(x)$ is a function that describes the nanoline height profile. One guess at a magnetization distribution $\alpha(x, z)$ is:

$$\alpha(x, z) = \alpha(x, h(x)) * \frac{z}{h(x)}, \quad (6.22)$$

with $\alpha(x, h(x))$ taken from Eq. 6.21. This expression is analytically very simple. Also, it has a good chance at producing relatively low exchange energies, as its derivative with respect to z is constant. The orientation of the magnetization vectors is displayed on the right in Fig. 6.2. Given this distribution and the expressions for the various energy terms, the rest is a matter of calculus.

The task of numerically computing the energy of these nanolines is not very complicated, but it does require large amounts of calculation time if performed exactly. The following will be a set of simplifications, so that the computation times may remain limited and some physical insight may be gained. The most important simplification will be the assumption that we deal with relatively low and broad nanolines.

Exchange energy

The exchange energy density is a relatively straightforward energy density functional, given the distribution $\alpha(x, z)$. From Eq. 6.8, it can be shown that:

$$E_{ex} = A_{ex} \left[\left(\frac{\partial \alpha}{\partial x} \right)^2 + \left(\frac{\partial \alpha}{\partial z} \right)^2 \right]. \quad (6.23)$$

The derivatives of α can be evaluated to:

$$\begin{aligned} \frac{\partial \alpha}{\partial x} &= \left[\frac{\partial^2 h / \partial x^2}{1 + (\partial h / \partial x)^2} - \frac{\partial h / \partial x}{h(x)} \arcsin \frac{\partial h / \partial x}{\sqrt{1 + (\partial h / \partial x)^2}} \right] \frac{z}{h(x)}; \\ \frac{\partial \alpha}{\partial z} &= \frac{1}{h(x)} \arcsin \frac{\partial h / \partial x}{\sqrt{1 + (\partial h / \partial x)^2}}. \end{aligned} \quad (6.24)$$

While this is enough to calculate exactly the exchange energy of any structure, we are interested in low, wide nanolines, with widths typically in the tens of nanometers and heights of a few nanometers. Thus, we may assume that $h \ll w$, and therefore that $\partial h / \partial x \ll 1$. Keeping only terms in first order in the derivatives dramatically simplifies them:

$$\begin{aligned} \frac{\partial \alpha}{\partial x} &= 0; \\ \frac{\partial \alpha}{\partial z} &= \frac{\partial h}{\partial x} \frac{1}{h(x)}. \end{aligned} \quad (6.25)$$

The exchange energy density is now approximated by:

$$E_{ex} = A_{ex} \left[\frac{\partial h}{\partial x} \frac{1}{h(x)} \right]^2. \quad (6.26)$$

Converted into dimensionless units, the value of the exchange constant equals $A_{ex} = 1.52 \times 10^{-4}$.

CALCULATED DEMAGNETIZING FIELD

Dipole energy

The magnetic dipole energy can be calculated using the magnetic charge density. In dimensionless form, this is given by:

$$\rho^* = \nabla \cdot \vec{M} = \left(-\sin \alpha \frac{\partial \alpha}{\partial x} + \cos \alpha \frac{\partial \alpha}{\partial z} \right). \quad (6.27)$$

In the general case, this too is an unwieldy expression when written in terms of $h(x)$ and its derivatives. However, it may be simplified drastically by assuming the nanolines are low and broad, as above:

$$\rho^* = \frac{1}{h(x)} \frac{\partial h}{\partial x}. \quad (6.28)$$

Our next step is to evaluate the integral Eq. 6.6 for the demagnetizing field. After integrating out the y - and z -integrals, we are left with:

$$\begin{aligned} H_x &= \frac{1}{2\pi} \int_{-\infty}^{\infty} \left[\arctan \frac{h(x')-z}{x-x'} + \arctan \frac{z}{x-x'} \right] \frac{\partial h}{\partial x'} \frac{dx'}{h(x')}; \\ H_z &= \frac{1}{2\pi} \int_{-\infty}^{\infty} \ln \left[\frac{(x-x')^2 + (z-h(x'))^2}{(x-x')^2 + z^2} \right] \frac{\partial h}{\partial x'} \frac{dx'}{h(x')}. \end{aligned} \quad (6.29)$$

The dipole energy density is now given - in the low structures approximation - by:

$$E_d = \vec{H}_d \cdot \vec{M} \approx \frac{1}{2} H_x. \quad (6.30)$$

The total energy of the system is now given by:

$$W = \int [E_d(\vec{r}) + E_{ex}(\vec{r})] d^3 \vec{r}. \quad (6.31)$$

To limit the calculation time for the total energy of this system on a standard PC, we evaluate this expression on a rough grid to calculate the dipole energy density. Also, we use some analytical calculus detailed in the appendix to this chapter to accelerate the calculations and enhance our understanding of the results. This is extended to a finer grid by cubic interpolation. Along with the much simpler expression for the exchange energy density, which can be evaluated directly, it gives us a total energy density over the fine grid. We can integrate this over a single nanoline to obtain the total magnetostatic energy, and hence the anisotropy field.

4 Calculated demagnetizing field

The first result of the models we investigate is the demagnetizing field they predict. These fields are shown in Figs. 6.3 and 6.4. Figure 6.3 is a vector plot of \vec{H}_d for the SC case (top) and the VC case (bottom). The vectors diverge from and converge to the locations of the magnetic charges. The figure shows that they are located on the surface for the SC model, and inside the material for the VC model. They are bigger for the SC model, indicating that the demagnetizing field has greater energy density in this case.

MAGNETISM OF PERIODIC NANOSTRUCTURES

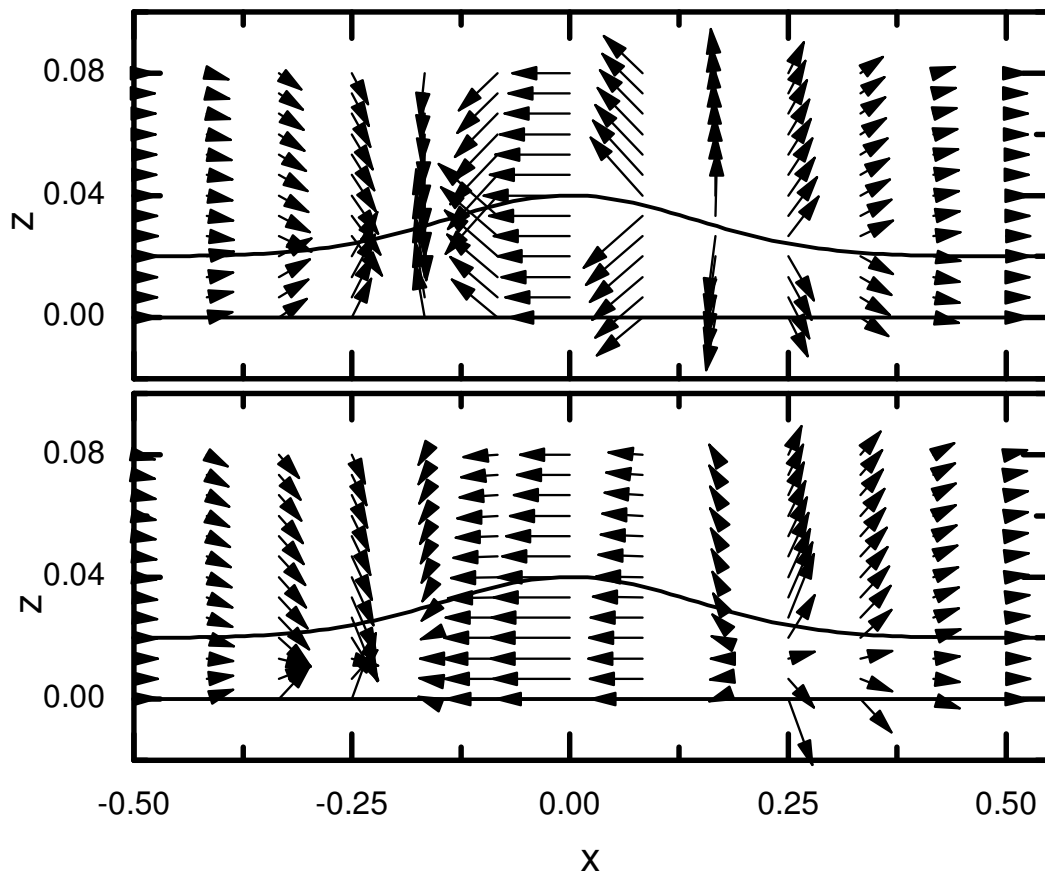


Figure 6.3: Vector diagrams of demagnetizing field. Top: SC model. Bottom: VC model. Lines indicate the extent of the magnetic material.

CALCULATED DEMAGNETIZING FIELD

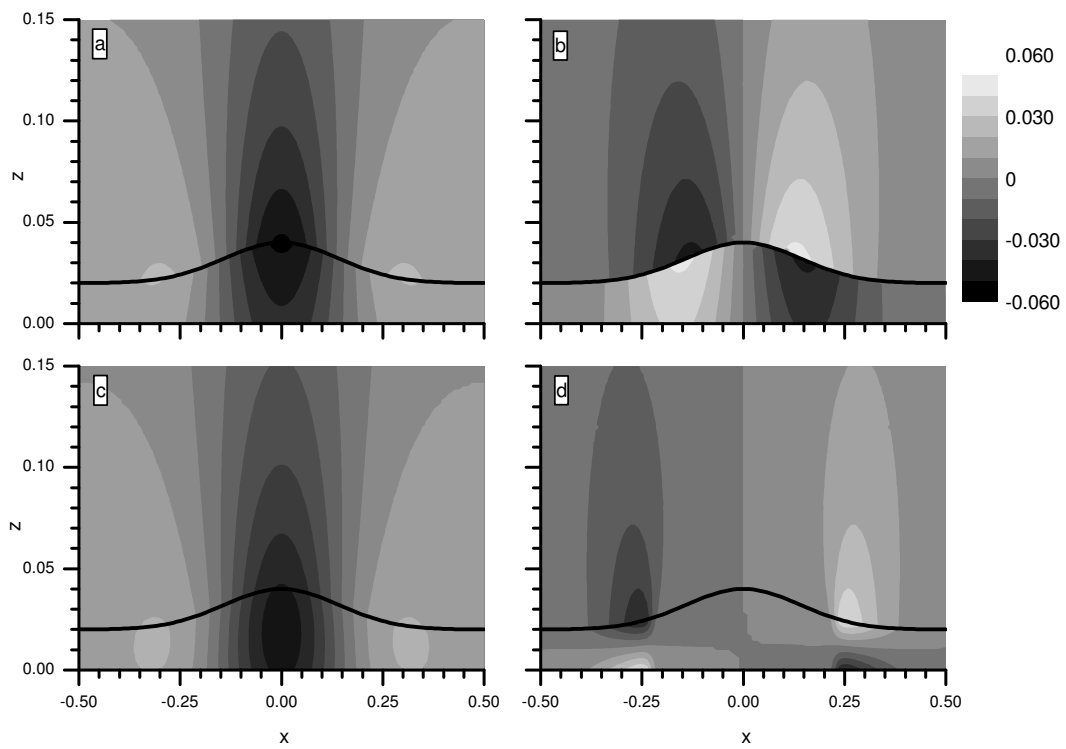


Figure 6.4: Demagnetizing field for the SC model (a: x component; b: z component) and the VC model (c: x component; d: z component). Lines indicate the extent of the magnetic material.

The x and z component of the field in the SC scenario are shown in Fig. 6.4 a and b, respectively. Figure 6.4 c and d show the x and z components of H_d for the VC case. Investigating the SC case, we find that the x component of H_d is opposite to the magnetization direction inside the nanoline itself. This is its usual orientation, hence the term ‘demagnetizing field’. In the background layer between the nanolines, however, its x component is aligned parallel to the magnetization. Although this orientation may appear puzzling at first sight, it is less mysterious when considered in the magnetic charge view. The magnetization points out of the structure at its right flank. Hence, a positive charge arises there. The next structure (not shown in the figure) has a negative charge at its left flank. Hence, a field line will run from one nanoline to the next that runs *parallel* to the magnetization. The total shape anisotropy of the nanolines is now a sum of the energy cost of the nanolines and the energy gain of the background layer in between. The z component (Fig. 6.4b) shows the location of the surface poles very clearly. Though it does not contribute to the anisotropy energy of the nanostructure as it is perpendicular to the magnetization, it might in principle be used in stray field detection. Its advantage over the x -component is that the latter has a relatively large applied field background, and thus requires more sensitive detection.

For the VC case, the demagnetizing field x component (Fig. 6.4c) and z component (Fig. 6.4d) are also shown. The picture of the x component is similar to its SC counterpart. The main difference can be seen around $x = \pm 0.3$, where the demagnetizing field reaches a maximum. In contrast to the SC case in Fig. 6.4a, the maximum is now *inside* the nanostructure. Hence, the contribution of the demagnetizing field to the anisotropy field will be smaller. The z component of the demagnetizing field is also smaller in the VC case, which stands to reason as the magnetic charge that generates it is spread out over a larger area. The most conspicuous feature of Fig. 6.4d is the fact that the field maxima are located relatively far out to the sides of the nanoline. We could find no obvious explanation for this phenomenon.

5 Calculated anisotropy field

We have run the simulations described above for both cases, choosing standard settings: $h_0 = 0.02$, $h_1 = 0.02$, $w = 0.2$. This means that we have a set of Gaussian peaks that are as high as the background, both being 3.72 nm high. The FWHM of the peaks is 62 nm, which is realistic considering our deposition results. We will vary the three parameters separately. Also, results are presented as a function of the total atomic flux, and contrast ratio. A discussion of the results is provided.

Structure height

First, we vary the nanoline height h_1 . The results are shown in Fig. 6.5. In the SC case, the anisotropy field is at first linear with respect to the nanoline height. This is to be expected, as the surface charge density scales as $\partial h / \partial x$. For high lines, the surface charge density is less than would be expected from extrapolation of the linear case.

CALCULATED ANISOTROPY FIELD

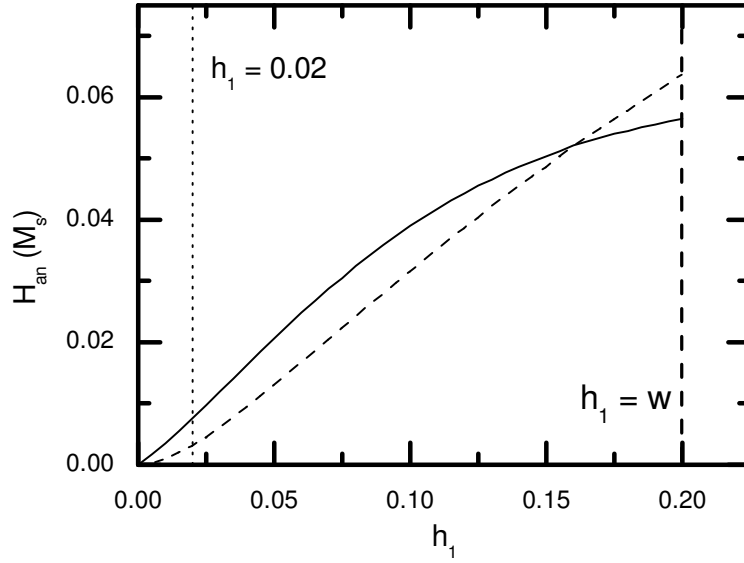


Figure 6.5: Anisotropy field as function of line height. Drawn line: SC model. Dashed line: VC model. Structures can no longer be considered low when height equals half their width $h_1 = w$.

This is due to the factor $1/\sqrt{1 + (\partial h/\partial x)^2}$ in the charge density. The VC case, however, is very much different. For small line heights, H_a goes as a higher power of h_1 . The reason for this is that the magnetic poles are spread out into the whole background layer. These diffuse poles create smaller demagnetizing fields than the concentrated surface poles of the homogeneous situation. In the VC model, H_a does not saturate for high h_1 . This is an artifact due to the assumption in the model that the lines are low. A more full calculation of the nanostructure properties would result in a more similar behavior at high h_1 for the SC and VC models.

Background height

The results for the background height are displayed in Fig. 6.6. Both models give an anisotropy that diminishes with increasing background, which is intuitively understandable as increasing h_0 makes the structure more and more like a simple layer, which has no in-plane shape anisotropy.

However, the decrease in anisotropy with increasing h_0 is far more rapid for the VC case than for the SC case. The reason for this effect can be found by looking at the plots of the demagnetizing field x-component shown in Fig. 6.4. In both models, \vec{H}_d is oriented along the magnetization in the region between the nanolines. This compensates for part of the energy cost of the demagnetizing field. However, for the VC model, its values are greater, and thus compensate for a larger fraction of the energy cost.

MAGNETISM OF PERIODIC NANOSTRUCTURES

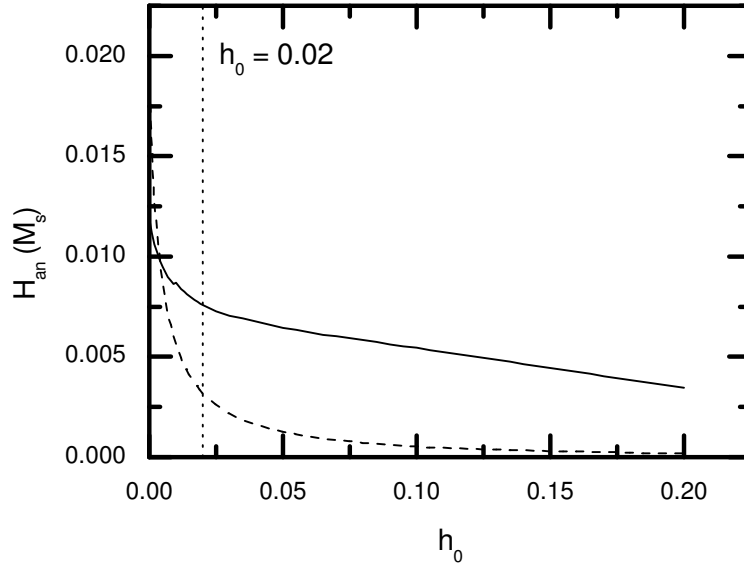


Figure 6.6: Anisotropy field as function of background height. Drawn line: SC model. Dashed line: VC model. Note the dramatic decline for the VC model.

Structure width

Figure 6.7 displays the effect of varying line width on the value of H_a . There are three regimes of line width, as indicated by the vertical dashed lines.

For very narrow lines, the assumption that $h_1 \ll w$ is no longer valid, and the results of the VC model can no longer be taken at face value. The high value of the resulting anisotropy here results primarily from the exchange energy contribution - the orientation of the spins has to change on a small length scale, which is energetically unfavorable. In this regime, the expressions for the SC case are still valid, and the anisotropy of the SC nanostructure increases linearly with increasing nanoline width. This is logical, as the nanoline can be regarded as a dipole if it is small enough. The moment of this dipole is then proportional to the nanoline cross-section area, and thus to the width of the nanoline. The interaction energy between the dipole and the background layer is proportional to the dipole moment, and thus to the nanoline width.

For high w , the nanolines overlap. This becomes seriously awkward when the single peak FWHM is more than half the nanostructure period. This point is at $w = 0.3$. Any bigger values of w are simply a further contribution to the overlap of the nanolines, and simply reflect the changes in effective h_0 and h_1 .

In the intermediate regime, H_a has a maximum for $h_1 \approx 0.08$ in the homogeneous case, and decreases monotonically with increasing w in the exchange model. For all values of w for which a comparison is meaningful, the SC scenario is less favorable than the VC model.

CALCULATED ANISOTROPY FIELD

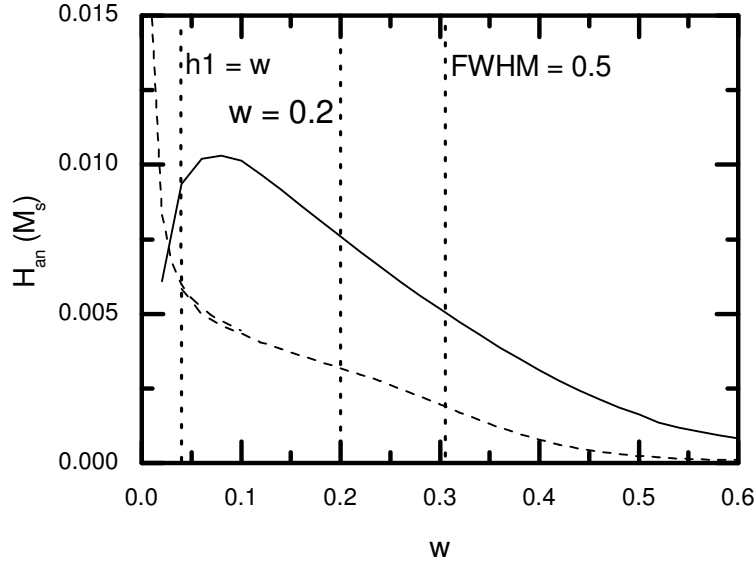


Figure 6.7: Anisotropy field as function of nanoline width. Drawn line: SC model. Dashed line: VC model.

Flux contrast

We define the contrast ratio as h_1/h_0 . As we varied it, we found that the resulting behavior differed strongly, depending on whether we varied h_0 or h_1 . However, the *ratio* of the anisotropy fields from the two models *did* change in a consistent fashion, as is shown in Fig. 6.8. For low contrast, the anisotropy of the nanostructures decreases faster with lower contrast in the VC case, as was already noted above. This behavior turns out to be very consistent as a function of contrast ratio.

The 'break-even point', where both scenarios predict the same amount of anisotropy, is around a contrast ratio of five to ten, and it is indicated in the figure. Attaining this kind of contrast ratio is not beyond atom lithography in general [10], but is virtually impossible with Fe using this transition. As the lowest anisotropy configuration is energetically the most favorable, we may conclude that the nanostructures described in this thesis will never be homogeneously magnetized.

Total flux

The results of a simulation of the anisotropy as a function of the total height are shown in Fig. 6.9 on the left. In this simulation, both h_0 and h_1 have been varied simultaneously; their values are identical for every data point and are shown on the x-axis. As can be seen, the results for both models are similar except for a factor determined by the contrast ratio. Based on the dependence on structure contrast observed above, we expect this behavior. The main deviation from this law occurs for high lines, where h_1 approaches w . In this domain, the VC model is expected to overestimate the anisotropy.

If we investigate the anisotropy ratio (H_{an} predicted by the exchange model in

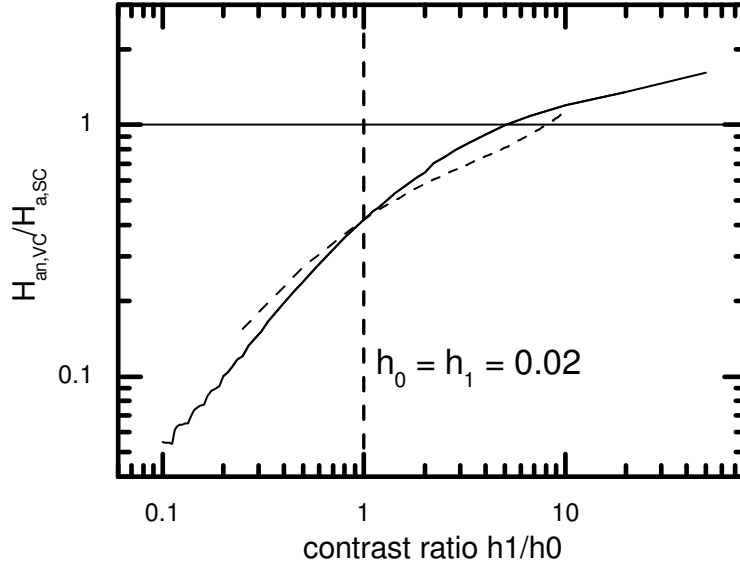


Figure 6.8: Ratio between magnetic anisotropy fields calculated for both models as a function of structure contrast. Drawn line: constant h_1 , varying h_0 . Dashed line: constant h_0 , varying h_1 .

units of that predicted by the homogeneous model) as a function of the nanoline height, we find that it is largely constant. This is shown in Fig. 6.9 on the right; the values for this ratio are consistently between 0.3 and 0.7. Indeed, when $h_0, h_1 < 0.15$, and the VC model can be expected to be accurate, the ratio between them never deviates more than 15 % from 0.45.

Real nanostructures

The nanolines that were deposited in the framework of this thesis could produce anisotropy fields of $7.59 \times 10^{-3}M$ for the SC model, and $3.18 \times 10^{-3}M$ for the VC model. These values correspond to 164 Oe and 69 Oe, respectively. This upper limit could be further reduced by a more efficient distribution of the space and volume charges in a more complicated arrangement than the two cases investigated here. The most important factor in achieving high anisotropy fields is the contrast ratio of line height to background height. Increasing the height and reducing the width of the nanostructures from their present values would also result in an increased anisotropy.

For nanolines as deposited at Radboud University [11], which are sine-shaped, and 8 nm high on a 20 nm background layer [11], the VC magnetization configuration tested here yields an anisotropy field of 33 Oe, whereas the SC model predicts an anisotropy field of 185 Oe. This difference of a factor 6 is mainly due to the fact that the surface poles generated by the homogeneously magnetized nanostructures generate a demagnetizing field that is independent of the background height h_0 . The inhomogeneously magnetized nanostructures are able to use the extra space

CONCLUDING REMARKS

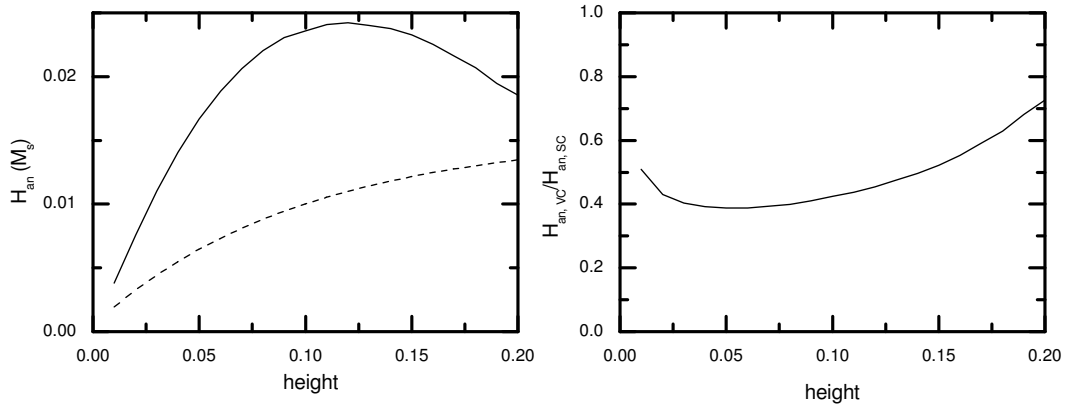


Figure 6.9: Left: Magnetic anisotropy as a function of total flux. Drawn line: SC model; dashed line: VC model. Dotted line indicates $h_0 = h_1 = 0.02$. Right: Ratio between results of the exchange and homogeneous models, which is nearly constant over a large range.

provided by the background to diffuse the poles, and reduce their effect.

6 Concluding remarks

We have investigated the anisotropy of ferromagnetic nanolines deposited by atom lithography theoretically. We found that the nanoline height contrast is the single most important parameter determining the anisotropy field. The values that result from the present calculations should be taken as upper limits.

A more detailed insight into the magnetism of these modulated structures can be gained by magnetic force microscopy (MFM). This form of scanning probe microscopy [12] uses a ferromagnetic tip to detect magnetic fields or field gradients. The tip size limits the resolution of the scheme to ~ 20 nm, which is small enough to discern the nanostructures, provided that the magnetic fields they generate are large enough. These stray fields reveal the domain structure of the nanostructured material. An investigation of its switching behavior and domain wall motion is then possible.

Having characterized the material, an investigation of its unique properties would be of interest. The main distinguishing feature of these nanostructures is their periodicity, which is guaranteed by the manufacturing process. This could effectively make the nanostructures a magnonic crystal. As the dispersion relationship for spin waves in a magnetic film depends on the thickness of the film [13], the periodic variations in thickness of the nanostructures entail periodic variations in spin wave dispersion. Hence, based on the Bloch theorem [14], we would expect some form of band structure to form for a suitable height modulation. The dispersion relationship for spin waves through the nanostructured medium might be obtained from time-resolved MOKE measurements [15]. The propagation of spin waves has also received interest in the context of solitons [16].

For a more dramatic variation of the spin wave spectrum, experiments with struc-

tured doping could be considered. Codepositing another ferromagnetic material would result in a magnetic layer of periodically varying composition. This, too, would affect the dispersion relationship of the spin waves, resulting a magnonic crystal. These experiments could be of great interest for spintronics applications [17].

References

- [1] E. du Trémolet de Lacheisserie, D. Gignoux, M. Schlenker, Eds., Magnetism, Kluwer Academic, Dordrecht (2002)
- [2] A. J. Bennett and J. M. Xu, Appl. Phys. Lett. **82** 3304-3306 (2003)
- [3] Y. Peng, T.-H. Shen, B. Ashworth, X.-G. Zhao, C. A. Faunce, and Y.-W. Liu, Appl. Phys. Lett. **83**, 362-364 (2003)
- [4] W. C. Uhlig and J. Shi, Appl. Phys. Lett. **84**, 759-762 (2004); J. I. Martín, M. Vélez, R. Morales, J. M. Alameda, J. V. Anguita, F. Briones, and J. L. Vincent, J. Magn. Magn. Mater. **249**, 156-162 (2002)
- [5] D. J. Griffiths, Introduction to Electrodynamics, 2nd Ed., Prentice-Hall, Englewood Cliffs (1989)
- [6] L. M. Magid, Electromagnetic Fields, Energy, and Waves, J. Wiley and Sons, New York (1972)
- [7] D. J. Griffiths, Introduction to Quantum Mechanics, 2nd Ed., Prentice Hall, Englewood Cliffs (1995)
- [8] C. Kittel, Rev. Mod. Phys. **21**, 541-583 (1949)
- [9] D. Rugar, H. J. Mamin, S. E. Lambert, J. E. Stern, I. McFadyen, and T. Yogi, J. Appl. Phys. **68**, 1169-1183 (1990)
- [10] V. Natarajan, R.E. Behringer, G. Timp, Phys Rev. **A53**, 4381-4385 (1996)
- [11] G. Myszkiewicz, J. Hohlfeld, A. J. Toonen, A. F. van Etteger, O. I. Shklyarevskii, W. L. Meerts, and Th. Rasing, Appl. Phys. Lett. **85**, 3482 (2004)
- [12] D. Sarid, Scanning Force Microscopy, Oxford University Press, Oxford (1994)
- [13] B. Hillebrands and K. Ounadjela (Eds.), Spin Dynamics in Confined Magnetic Structures I, Springer, Heidelberg (2002)
- [14] C. Kittel, Introduction to solid state physics, 7th Ed., J. Wiley and Sons, New York (1996)
- [15] M. van Kampen, C. Jozsa, J. T. Kohlhepp, P. LeClair, L. Lagae, W. J. M. de Jonge, and B. Koopmans, Phys. Rev. Lett. **88**, 227201 (2002)
- [16] J. W. Fleischer, M. Segev, N. K. Efremidis, D. N. Christodoulides, Nature **422**, 147 - 150 (2003)

CONCLUDING REMARKS

- [17] D. Awschalom, R. A. Buhrman, J. M. Daughton, S. von Molnár, and M. L. Roukes, Eds., Spin Electronics, Kluwer Academic, Dordrecht (2004)

A Appendix

Empirically, it was found that the calculation of the energy of the VC magnetic configuration was still a very time-consuming process, as the integral for the demagnetizing field is very slow to converge. This can be seen by looking at the integrand, which goes as $1/x'$ for large x' ; thus, the integral only converges because $\partial h/\partial x'$ periodically changes sign.

We therefore look for an analytical way to estimate the integral. This may be done by splitting the integral in three parts - one for $x' < -x_c$, one for $-x_c < x' < x_c$ and one for $x_c < x'$. In the central part, the arctangents are crucial to keep the integrand finite, and the integral is evaluated explicitly. In the outer parts, we approximate the integrand by:

$$\left[\arctan \frac{h(x') - z}{x - x'} + \arctan \frac{z}{x - x'} \right] \frac{\partial h}{\partial x'} \frac{dx'}{h(x')} \approx \frac{1}{x - x'} \frac{\partial h}{\partial x'} dx'. \quad (6.32)$$

This approximation is valid provided that $x_c \gg \{\max(h), z\}$. The integral now becomes:

$$\int_{x_c}^{\infty} \frac{\partial h}{\partial x'} \frac{dx'}{x - x'}. \quad (6.33)$$

Integration by parts yields:

$$\int_{x_c}^{\infty} \frac{\partial h}{\partial x'} \frac{dx'}{x - x'} = \frac{h(x_c)}{x_c - x} - \int_{x_c}^{\infty} \frac{h(x')}{(x - x')^2} dx'. \quad (6.34)$$

This integral will at least converge much faster, but it can be estimated analytically. In fact, if we assume that the Gaussian peaks are well-separated ($\exp(-0.25/w^2) \ll 1$) or roughly $w < \sqrt{2}/4 \approx 0.35$, the contribution of a single peak around $x - x' = n$, $|n| \gg \{x, w\}$ can be approximated further:

$$\begin{aligned} \int_{x_c}^{\infty} \frac{h_1 \exp(-(x'-n)^2/w^2)}{(x-x')^2} dx' &= \int_{x_c-n}^{\infty} \frac{h_1 \exp(-y^2/w^2)}{(x+n-y)^2} dy \\ &= \int_{x_c-n}^{\infty} \frac{h_1 \exp(-y^2/w^2)}{(1-(y/(x+n))^2)} dy \times \frac{1}{(n+x)^2} \\ &\approx \frac{h_1 w \sqrt{\pi}}{n^2}. \end{aligned} \quad (6.35)$$

The approximation is possible because the Gaussian is zero except around $y \approx 0$, and the derivatives of the function by which it is multiplied are very small at this point. Summing this result over all n yields $h_1 w \sqrt{\pi} \times \pi^2/6$, and we must only subtract the terms from that sum that we include in the numerically evaluated integral.

Now the contribution of a background term h_0 to the integral becomes:

$$\int_{x_c}^{\infty} \frac{h_0}{(x - x')^2} dx' = \frac{h_0}{x - x_c}. \quad (6.36)$$

Putting the previous results together, we arrive at a result for the tail integral:

$$\int_{x_c}^{\infty} \frac{\partial h}{\partial x'} \frac{dx'}{x - x'} = \frac{h(x_c) - h_0}{x - x_c} - h_1 w \sqrt{\pi} \left[\frac{\pi^2}{6} - \sum_{n=1}^{n_c-1} \frac{1}{n^2} \right]. \quad (6.37)$$

APPENDIX

In order to count peaks wholly or not at all in this summation we put x_c halfway between the two peaks, *i.e.* $x_c = n_c - 1/2$.

All of this work leads to a relatively quickly evaluated expression for the demagnetizing field, which separates the local effects from a 'mean field' that is generated by the nanostructure array:

$$H_x = \frac{1}{2\pi} \int_{-x_c}^{x_c} \left[\arctan \frac{h(x')-z}{x-x'} + \arctan \frac{z}{x-x'} \right] \frac{\partial h}{\partial x'} \frac{dx'}{h(x')} + \frac{h(x_c)-h_0}{\pi(x-x_c)} - \frac{h_1 w}{\sqrt{\pi}} \left[\frac{\pi^2}{6} - \sum_{n=1}^{n_c-1} \frac{1}{n^2} \right]. \quad (6.38)$$

QUANTUM FEATURES IN ATOMIC NANOFABRICATION...

Chapter 7

Quantum Features in Atomic Nanofabrication using Exactly Resonant Standing Waves

The work described in this chapter was done at the University of Konstanz. The text has been published in Phys. Rev. Lett. 93, 237402 (2004).

The ability to control the motion of atoms utilizing the atom-light interaction has led to new fundamental physics such as laser cooling [1], Bose-Einstein condensation [2], and precision experiments [3]. The control of the trajectories of atoms has also found its way to applied science and allows the fabrication of nanostructures [4, 5].

The basic idea of atomic nanofabrication is the controlled deposition of atoms on a surface. This is achieved by employing spatially varying light forces, realized in *standard* atomic nanofabrication with off resonant standing light waves. These forces are well described within a classical atom-light interaction model [5]; however, this picture implies that these forces vanish for exactly resonant light fields. Thus no nanostructures are expected, whereas the quantum mechanical treatment of the atom-light interaction predicts the formation of structures for exactly resonant standing light waves. Furthermore, the detailed analysis of the formed pattern reveals that in contrast to the off resonant case the spatial phase of the light field plays a crucial role for the quantum mechanical motion of the atoms. Additionally, this system represents a new method for generating periodic patterns with feature spacing smaller than the periodicity of the light intensity distribution. Introducing a detuning in the order of the natural linewidth periodic nanostructures with doubled periodicity can be fabricated. This adds a new scheme to the previously proposed and demonstrated methods to beat the $\lambda/2$ periodicity limit of standard nanofabrication [6–8].

In our experiments a chromium atomic beam is collimated to a divergence of less than 1 mrad (full width at half maximum) by one-dimensional laser cooling in a $\text{lin}\perp\text{lin}$ configuration. The atomic beam impinges perpendicular onto the exactly resonant standing light wave (${}^7\text{S}_3 \rightarrow {}^7\text{P}_4$ at $\lambda=425.6$ nm) which is realized by

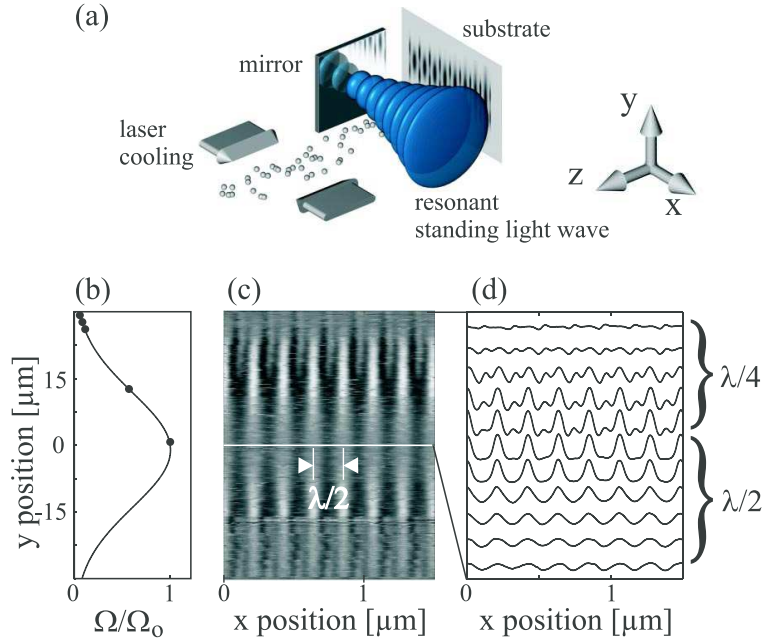


Figure 7.1: Experimental setup and results. (a) A collimated chromium beam impinges on a resonant standing light wave and subsequently hits a substrate. After deposition the substrate topography is analyzed with an atomic force microscope (AFM). (b) The Rabi frequency shows a spatial dependence due to the Gaussian laser beam profile along the y direction. Thus each individual substrate contains the whole intensity dependence of the atom-light interaction. (c) The AFM image and (d) cross sections reveal the light intensity dependence of the formed structures. For low intensity, peculiar periodic structures with feature spacings below $\lambda/2$ are observed.

retroreflecting a linearly polarized Gaussian laser beam (waists $w_z = 21 \pm 3 \mu\text{m}$ and $w_y = 35 \pm 3 \mu\text{m}$, power $P = 17 \pm 2 \text{mW}$) from a mirror. Thus the interaction time of the atoms with a mean longitudinal velocity $v_z = 1000 \text{m/s}$ is on the order of the natural lifetime of the excited state. After traversing the light field, the chromium atoms are deposited on a silicon substrate which is placed $35 \pm 5 \mu\text{m}$ behind the center of the standing light wave in order to reduce diffraction effects from the substrate edge [9]. After 30 min of deposition, the sample is taken out of the high vacuum chamber and analyzed with an atomic force microscope (AFM). In Figs. 7.1(c) and 7.1(d) the topography of the fabricated nanostructure is shown. The image consists of 42 overlapping AFM scans revealing the topography over $60 \mu\text{m}$ in the y direction. Because of the Gaussian profile of the light field in the y direction [see Fig. 7.1(b)], this image shows the full intensity dependence of the focusing properties of the resonant standing light wave.

The measured topography reveals that for high light intensities nanostructures with a periodicity of $\lambda/2$ corresponding to 213 nm are produced. This is the same result as obtained with an off resonant standing light wave, although in our experiment there is no force expected in the classical atom-light interaction picture. For smaller intensities a striking complex periodic line pattern is produced, which re-

veals lines spaced at 213 nm and additional features in between. We show that this feature can be attributed to the quantum nature of the atom-light interaction and of the atomic propagation.

First we give a qualitative discussion of the obtained experimental results in the framework of dressed states. We then discuss our quantum mechanical simulations which even allow a quantitative comparison between theory and experiment.

Dressed states are the eigenstates of the coupled atom-light system and are superpositions of the eigenstates of the uncoupled atom $|g\rangle$ and $|e\rangle$. In the exactly resonant case the dressed states and their energy are very simple [10] and are given by:

$$|\pm; \vec{r}\rangle = \frac{1}{\sqrt{2}}(e^{-i\phi(\vec{r})/2}|g\rangle \pm e^{i\phi(\vec{r})/2}|e\rangle), E_{\pm} = \pm \frac{\hbar}{2}|\Omega(\vec{r})|, \quad (7.1)$$

where the atom-light coupling is characterized by the complex Rabi frequency $\Omega(\vec{r}) = -2\vec{d} \cdot \vec{E}(\vec{r}) = |\Omega(\vec{r})|e^{i\phi(\vec{r})}$, \vec{d} is the atomic electric-dipole moment, and \vec{E} represents the electric field amplitude of the light field.

For a perfect standing light wave, the dressed states are degenerate at the nodes where the electric field vanishes and thus $E_+ = E_- = 0$. This degeneracy is lifted in our experiment, because we use a mirror with a reflectivity of $R = 94\%$. The corresponding intensity distribution and resulting complex Rabi frequency is depicted in Fig. 7.2(a). It is important to note that the phase of the Rabi frequency changes dramatically at the nodes of the standing light wave that breaks the symmetry of the light field there. In Fig. 7.2(b) the corresponding dressed state energies are shown and the motion of a ground state atom is indicated.

In the regions where the Rabi frequency has a weak phase dependence the evolution of a ground state atom is given by the corresponding dressed states, whose motions are governed by Newtons equations of motion resulting from the corresponding potential E_+ and E_- . In standard nanofabrication utilizing far off resonance light forces the ground state atom is very well described by only one dressed state (blue detuning mainly $|+\rangle$). But in an exactly resonant light field a ground state atom is described as a fifty-fifty superposition of the two dressed states $|+\rangle$ and $|-\rangle$. Thus an atomic wave packet in a light field gradient will split into two parts. The $|-\rangle$ is attracted to the intensity maxima while the $|+\rangle$ state is pulled to the intensity minima as indicated in Fig. 7.2(b). This splitting is known as the optical Stern Gerlach effect [11] and has already been observed by looking at the momentum distribution [12]. In our experiment we directly observe this effect by detecting the atomic position on the nanometer scale.

The motion in the $|-\rangle$ -state potential is almost perfectly harmonic close to its minimum and concentrates the atoms like a lens for matter waves. This is very similar to the standard atomic nanofabrication schemes. The $|+\rangle$ -state potential has a triangular shape in the vicinity of its minimum and corresponds to an atom optical axicon, which produces a focal line. Since the distance between adjacent $|+\rangle$ -state and $|-\rangle$ -state potential minima is $\lambda/4$, nanostructures with half the standard periodicity limit of $\lambda/2$ are expected.

The experimental observation that these $\lambda/4$ structures are not found for high light intensity can easily be understood by realizing that nonadiabatic (NA) transi-

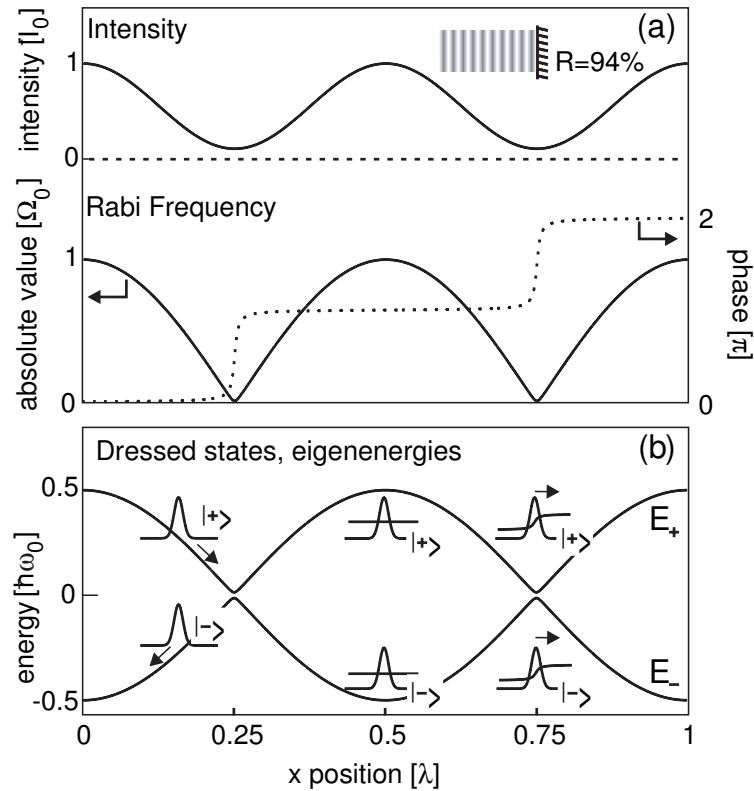


Figure 7.2: Dressed states description of on resonant atom-light interaction: (a) The standing light wave is formed by retroreflecting a laser beam from a mirror with reflectivity $R = 94\%$ as shown in the inset. This leads to a periodic intensity distribution that is not fully modulated (depicted not to scale). Hence, the Rabi frequency is complex. The change in phase proves to be dramatic at the standing wave node, where the phase jumps by π within few nanometers. (b) Where the phase is constant, the ground state wave packet is decomposed into two resting dressed state wave packets, whereas near the nodes this decomposition leads to two moving dressed state wave packets. Their motion is deduced from the dressed state eigenenergies, therefore a $|+\rangle$ -state wave packet is attracted to the node and a $|-\rangle$ -state wave packet to the antinode of the standing wave. As illustrated at position $x = 0.75$, the motion of wave packets near the node is influenced less by the potentials and more by the phase gradient of the Rabi frequency.

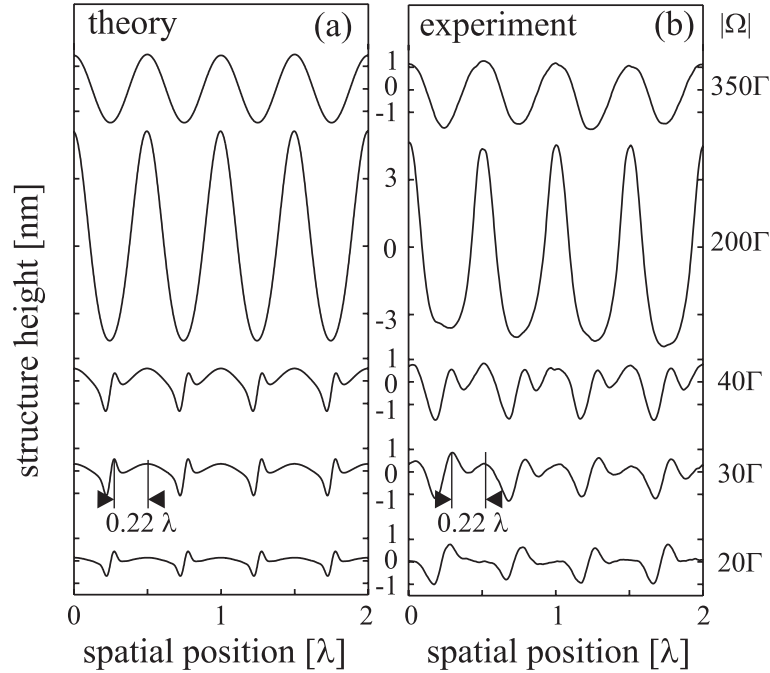


Figure 7.3: (a) Cross sections of the calculated atomic flux at a distance of $35\ \mu\text{m}$ behind the center of the standing wave for the indicated Rabi frequencies. For large Rabi frequencies, $\lambda/2$ period nanostructures are formed, whereas low Rabi frequencies lead to peculiar patterns with feature spacings smaller than $\lambda/2$. (b) AFM cross sections taken at different positions as indicated with solid circles in Fig. 7.1(b) corresponding to equivalent Rabi frequencies as used in the quantum simulation. The experimental findings are in excellent quantitative agreement with the simulation.

tions between the dressed states can happen near the nodes. The probability for a NA transition is estimated as discussed in [10]. It is found that the reflectivity must be chosen smaller than 50% to suppress NA transitions and allow for the atoms to oscillate around the potential minima of the $|+\rangle$ state. For our high reflectivity of $R = 94\%$ the NA transition probability is almost unity. However, for interaction times shorter than a quarter of an oscillation time in the axicon potential, which depends on the light intensity, a localization at both nodes and antinodes can be expected. Thus the simple dressed state potential picture explains why in the high intensity region only $\lambda/2$ structures are observed, whereas it fails to explain the observed complex pattern for low light intensity shown in Figs. 7.1(d) and 7.3(b).

The so far discussed semiclassical description of the motion is correct only for light fields with vanishing phase gradients. But near the node, where the phase of the Rabi frequency changes rapidly, the simple potential treatment is not applicable. Nevertheless, the dressed state picture allows one to understand the position of the lines formed near the nodes of the standing light wave qualitatively. As indicated in Fig. 7.2(b) a resting atomic ground state wave packet at the light field node is described in the dressed state basis by a coherent superposition of two dressed state wave packets moving in the same direction with a momentum $m v = \hbar/2\nabla\phi$. For our

experimental situation we estimate the velocity of these wave packets to be $\sim 26v_r$ where $v_r = \hbar k/m = 1.8$ cm/s is the recoil velocity and k is the wave number of the light. Thus one expects that atoms in the $|+\rangle$ state near the node run up the potential due to this velocity [indicated in Fig. 7.2(b)]. An estimate of the expected shift after a certain time can be found by calculating the classical trajectory of a particle starting at the node with an initial velocity $\sim 26v_r$ in the linear potential $V(x) = \hbar k|\Omega|x/2$. For the interaction time of 40 ns and a Rabi frequency of $|\Omega| = 20\Gamma$ we find the position to be shifted by 14 nm from the node. Experimentally we observe 12 ± 3 nm. This effect is very closely connected to the scattering force [11] commonly applied in laser cooling. There the situation is usually much simpler since the populations of the dressed states can be assumed to be in steady state, while in our experiment this is not the case.

Therefore to understand our experimental findings quantitatively we numerically solve the Schrödinger equation for the two-level atom in momentum space [13]. Here, the two-level approach is reasonable as long as the intensive linearly polarized light field defines the quantization axis and thus couples only magnetic substates with equal quantum number ($\Delta m = 0$). This is strictly speaking not true near the nodes. Therefore we numerically calculated the eigenenergies near the intensity minimum including the earth magnetic field for arbitrary directions. We find that the resulting eigenenergies are always symmetric with respect to the node of the standing light wave. Additionally the spatial range where anticrossings [6] between a few of the involved energy levels occur is ± 4 nm, which is the region where the dynamics is governed anyway by NA transitions. In order to get a quantitative agreement between the experimental findings and the numerical solution we include the effect of spontaneous emissions empirically. According to the dressed state analysis given in [10], spontaneous emissions can change the dressed state leading to momentum diffusion due to the instantaneous sign reversal of the dipole force (the recoil kick of the emitted photon is negligible). After the interaction time t this momentum diffusion translates into a feature broadening $\Delta x(\Omega) \propto v_r \Omega t / \Gamma$. To account for this broadening a convolution of the calculated spatial probability distribution (taking into account the divergence of the beam) with a Gaussian of width $\Delta x(\Omega)$ is applied. This convolution is important only at high light intensities while it does not significantly influence the structure shape at low light intensities. The additional broadening effect due to the growth behavior of Cr [9] is negligible for our broad structures (70 nm).

Cross sections of the calculated atomic flux at a distance of $35 \mu\text{m}$ behind the center of the standing wave are shown in Fig. 7.3(a) and compared to the experimental findings shown in Fig. 7.3(b). The experimental cross sections are taken at positions indicated in Fig. 7.1(b) with solid circles. The theoretical curves shown are obtained for the indicated Rabi frequencies. These values are consistent within the uncertainty of the independently measured incoming power and beam waists. Furthermore, we take into account the internal magnetic substructure of chromium by multiplying the calculated Rabi frequency by a factor of 0.65 (average Clebsch-Gordan coefficient for linear polarization), assuming equally populated substates. This is valid in our case because the atoms travel 1 m in a magnetically unshielded

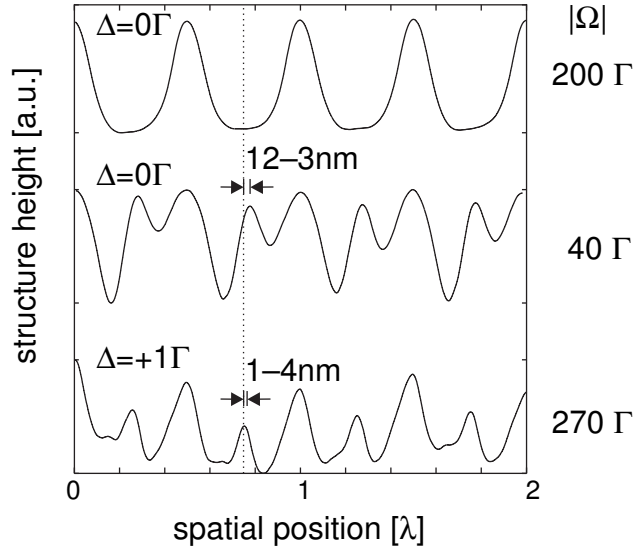


Figure 7.4: Comparison between nanostructures fabricated with different detunings: For $\Delta = 0$, $\lambda/2$ structures are shown to illustrate the shift of 12 ± 3 nm of the new feature in between. The nanostructures obtained by detuning the laser frequency $\Delta = 1\Gamma$ exhibit a much smaller shift of 1 ± 4 nm. The observed behavior confirms the prediction of our quantum simulation and demonstrate the periodicity doubling for very near resonant standing light waves.

region before they enter the focusing region. The simulated flux is in very good agreement with the experimental finding for all Rabi frequencies, and especially the peculiar structure shape is very well reproduced. It is important to note that the structure width and height at high Rabi frequencies are dominated by the momentum diffusion resulting from spontaneous emission.

Our simulations predict that for small blue detuning $\Delta = 1\Gamma$ of the standing light wave the production of nanostructures with a period of $\lambda/4$ is possible. Our results are similar to the reported periodicity reduction by Gupta et al. [6], where the chromium specific polarization dependence of the atom-light interaction was utilized. Another method using a Raman configuration consisting of two pairs of counterpropagating traveling wave fields has also been put forward to realize optical potentials with $\lambda/8$ periodicity [8]. Our experimental findings are shown in Fig. 7.4, where we compare $\lambda/2$ focusing in the high intensity limit with the low intensity focusing for exactly on resonance and detuned $\Delta = 1\Gamma$ standing light wave. The observed shift for exactly resonant standing light waves of 12 ± 3 nm is in excellent agreement with the theoretical prediction of 12.7 nm. In the detuned case the theory predicts 0.7 nm which is also consistent with the measured shift of 1 ± 4 nm deduced from the pattern shown in Fig. 7.4.

In conclusion, we have shown that exactly resonant light waves employed in an atomic nanofabrication scheme lead to new complex nanostructures. We are able to attribute the unexpected atomic distribution found on the substrate to the presence of the phase gradient of the resonant light field near its nodes. Our quantum sim-

ulations confirm our observations quantitatively. We have also shown that the $\lambda/2$ periodicity limit of conventional atomic nanofabrication schemes can be improved by a factor of 2 using standing light waves with a detuning on the order of the natural linewidth.

We thank J. Mlynek for his generous support, and O. Maragò for many fruitful discussions. This research is funded by the SFB513 and Emmy Noether program of the Deutsche Forschungsgemeinschaft, and the Optik-Zentrum in Konstanz and by the RTN network Cold quantum gases under Contract No. HPRN-CT-2000- 00125.

References

- [1] Steven Chu, C.N. Cohen-Tannoudji, W.D. Phillips, *Rev. Mod. Phys.* **70**, 685741 (1998)
- [2] W. Ketterle, *Rev. Mod. Phys.* **74**, 1131-1151 (2002)
- [3] T. L. Gustavson, P. Bouyer, and M. A. Kasevich, *Phys. Rev. Lett.* **78**, 2046-2049 (1997)
- [4] G. Timp, R.E Behringer, D.M. Tennant, J.E. Cunningham, M. Prentiss and K.K. Berggren, *Phys. Rev. Lett.* **69**, 1636-1639 (1992)
- [5] D Meschede and H Metcalf, *J. Phys. D: Appl. Phys.* **36** (2003) R17-R38; M.K. Oberthaler and T. Pfau, *J. Phys.: Condens. Matter* **15**, R233-R255 (2003)
- [6] R. Gupta, J. J. McClelland, P. Marte, and R. J. Celotta, *Phys. Rev. Lett.* **76**, 4689-4692 (1996)
- [7] Th. Schulze, B. Brezger, P. O. Schmidt, R. Mertens, A. S. Bell, T. Pfau, and J. Mlynek, *Microelectron. Eng.* **46**, 105-108 (1999).
- [8] B. Dubetsky and P. R. Berman, *Phys. Rev. A* **66**, 045402 (2002), and references therein.
- [9] W. R. Anderson, C.C. Bradley, J. J. McClelland, and R. J. Celotta, *Phys. Rev. A* **59**, 2476-2485 (1999).
- [10] J. Dalibard and C. Cohen-Tannoudji, *J. Opt. Soc. Am. B* **2**, 1707-1720 (1985)
- [11] R. J. Cook, *Phys. Rev. A* **35**, 3844-3448 (1987)
- [12] T. Sleator, T. Pfau, V. Balykin, O. Carnal, and J. Mlynek, *Phys. Rev. Lett.* **68**, 1996-1999 (1992)
- [13] M.A. Efremov, M.V. Fedorov, V.P. Yakovlev and W.P. Schleich, *Laser Physics* **13**, 995-1003 (2003)

Chapter 8

Barrier-limited surface diffusion in atom lithography

This chapter has been published in J. Appl. Phys. 95 1749-1755 (2004).

1 Introduction

One of the many applications of the optical dipole force [1] is atom lithography [2]. In this technique, a laser light field induces an electrical dipole moment in atoms passing through it. This electrical dipole experiences a force from the intensity gradient of the light field. Using a plane standing wave, as shown in Fig. 8.1, the light field will function as an array of lenses, focusing the atoms to the nodes or antinodes for light frequencies above or below the atomic resonance. By placing a substrate in the focal plane, the atoms are deposited onto this substrate with a spatially modulated flux distribution with half-wavelength period. The resulting structures can be investigated *ex situ* by techniques such as Atomic Force Microscopy (AFM). The main advantages of this lithography technique are its compatibility with Molecular Beam Epitaxy (MBE) [3] and its considerable parallelism [4].

This kind of experiment has been performed using Na [5], Cr [6] and Al [7] atoms, and our group is pursuing it for Fe atoms [8]. In the case of Cr, an extensive study on structure widths was done by Anderson *et al.* [9]. They found that the structures deposited were always 20 to 30 nm wider than the incoming atomic beam flux distribution. Due to the confidence and thoroughness with which this atomic beam flux distribution can be calculated, they concluded that the broadening of the nanostructures must be caused by a diffusion process on the substrate. However, the broadening proved oddly independent of substrate temperature. In Na deposition experiments by Behringer *et al.* [10], details of the sample preparation method were shown to be of crucial importance to the diffusion effects. Samples heat-cleaned in a very well baked-out ultra-high vacuum (UHV) chamber proved to be so susceptible to surface diffusion that there were no visible structures at the end of the deposition. Samples prepared in an unbaked vacuum chamber showed no signs of surface

BARRIER-LIMITED SURFACE DIFFUSION IN ATOM LITHOGRAPHY

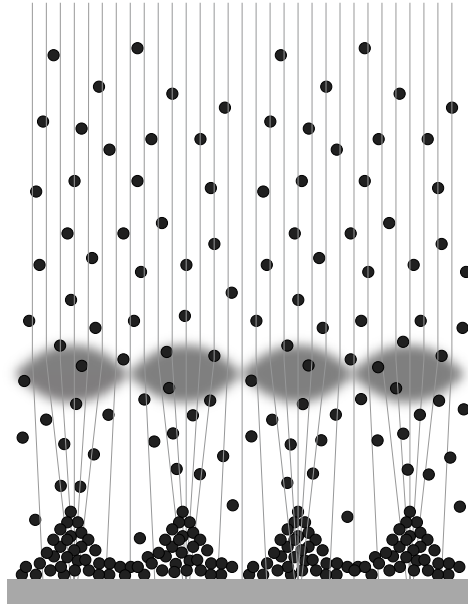


Figure 8.1: Direct-write atom lithography schematic. Atoms are deflected and focused by the laser standing wave and follow the trajectories indicated. They are deposited onto the substrate, where a periodic structure is generated.

diffusion. Behringer *et al.* [10] attribute this effect to residual hydrocarbons on the sample surface that limit surface diffusion and act as nucleation sites.

Jurdík *et al.* [11] attempt to explain the broadening of the Cr nanostructures using thermally activated surface diffusion as a mechanism. They explore various atomistic models, and find that the resulting structures show a very strong dependence on substrate temperature and on the diffusion parameters. This result prompted Bradley *et al.* [12] to investigate the hypothesis that the surface diffusion was caused by the energy released when the atoms hit the surface, a process dubbed Impact Cascade Diffusion (ICD). However, this theory does not explain the immense dependence on sample preparation conditions found by Behringer *et al.* [10]. As Jurdík *et al.* point out, their thermal surface diffusion model does not take into account the effects of pollution.

In this paper, we consider two alternative explanations for this diffusion effect. One possible explanation is that pollutants such as hydrocarbons, oxygen, *etc.*, act as a limiting factor on the surface diffusion effects observed in atom lithography experiments. A clear indication of this can be found in the extreme dependence on vacuum conditions that Behringer *et al.* [10] find. The other effect under consideration is the possibility that surface diffusion might be limited by an increased hopping activation energy at terrace boundaries. This effect is well-known in surface physics and is called the Ehrlich-Schwoebel barrier (ES barrier) [13].

The remainder of this paper will be dedicated to our numerical investigation of structure broadening in atom lithography. We begin by describing the model we use in section 2, and will continue by assigning values to most of its free parameters

in section 3. Then we first display the results of the pollution hypothesis in section 4, followed by those of the ES-barrier scenario in section 5. We compare both hypotheses in section 6.

2 Numerical model

We model atom lithography as a process in which atoms impinge perpendicularly on a surface. The atoms focused by the light field have a lateral distribution, which we assume to be Lorentzian in shape. We assume that some of the atoms will not be focused by the standing light wave, mainly because of imperfections in the atom beam. They are described as a homogeneous background flux. The surface is described as a one dimensional linear grid of sites. We limit our model to one dimension to limit the complexity of the code and reduce calculation times. The grid spacing is assumed to be equal to the lattice constant for Cr. We set the grid size to the period of the incoming atom flux distribution, 212 nm for Cr. This corresponds to 739 sites for a lattice constant of 0.287 nm. Initially, the surface is flat and nonreactive. We apply periodic boundary conditions to the surface.

Once on the surface, the atoms are able to hop from site to site. We assume all hopping processes equally likely, provided that the atoms can move without reducing their number of nearest neighbors. Processes that require reduction of the number of nearest neighbors are not allowed. If hopping in both directions is allowed, hopping proceeds with 50 % likelihood in either direction. If only one hopping direction is available, there is a 50 % chance that the atom remains stationary, and a 50 % chance that it will hop in the available direction. If both hopping directions are blocked, the atom remains stationary. This model implies that a cluster of two atoms is a stable island, and that diffusion across planes at slope 45 degrees occurs as quickly as on horizontal planes. The frequency of hopping steps is assumed constant, and given by the Arrhenius relation:

$$R_{hop} = R_0 e^{-\frac{E_d}{k_B T}}, \quad (8.1)$$

where R_0 is the lattice frequency of the material, which we assume to be 10^{12} s^{-1} , k_B is Boltzmann's constant, and T is temperature (in degrees K). We perform all simulations at $T = 300\text{K}$ unless otherwise stated.

We incorporate a possible ES barrier by assigning a greater activation energy $E_d + E_{ES}$ and thus a reduced hopping chance to atoms stepping down from a terrace. Atoms cannot step up onto a terrace as doing so would reduce their number of nearest neighbors. The ES hopping rate is given by:

$$R_{ES} = R_0 e^{-\frac{E_{ES} + E_d}{k_B T}} = R_{hop} e^{-\frac{E_{ES}}{k_B T}}. \quad (8.2)$$

The pollution is represented as a homogenous flux of pollutant species from the residual gas in the vacuum system. We assume that these pollutants will stick on the site where they hit the substrate if and only if they land on top of a chemically

BARRIER-LIMITED SURFACE DIFFUSION IN ATOM LITHOGRAPHY

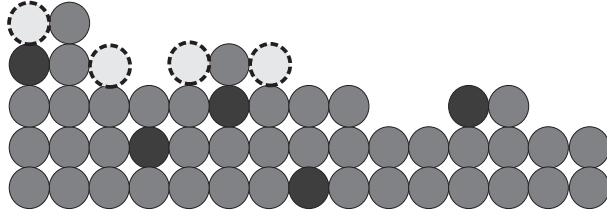


Figure 8.2: Artifacts in our diffusion model. Grey circles: deposited atoms. Dark circles: pollutant species. Dashed circles: sites to which a deposited atom may hop. Atoms move freely to sites that have no fewer neighbors than their present site, but not at all to sites that have fewer nearest neighbors. Pollutant species cannot diffuse at all and act as diffusion inhibitors.

active (non-pollutant, non substrate) atom. There they occupy exactly one atomic grid position each. They cannot diffuse at all in our model.

Our diffusion model incorporates two distinct timescales. Usually, the fastest of these by far is the regularized hopping time, which is $\tau_{hop} \sim 10^{-7}$ s at room temperature, but extremely sensitive to changes in temperature and hopping activation energy. The time between atom arrivals on the whole grid τ_{dep} is typically in the tens of milliseconds. For low temperatures, the two are not necessarily orders of magnitude apart. We compensate for this by running an internal clock with clock time 0.1 times the shortest timescale if the two timescales are less than an order of magnitude apart. If $\tau_{hop} \leq 0.1\tau_{dep}$, the hopping time is taken as clock time. We then round the longer timescale to an integer number of clock ticks.

Figure 8.2 displays some of the possibilities and artifacts in our diffusion model. Left, an atom on a step edge can step down or move away from the edge. If $E_{ES} = 0$, both processes are equally likely. In the case of ES-barrier simulations, the atom has 50 % chance to move away from the step, and a small chance to cross it. If neither happens, the atom does nothing during this diffusion step. In the center, atomic motion over pollutants embedded in the surface is unimpeded. Right, an atom that encounters a pollutant species is fixed, as moving would require reduction of its number of nearest neighbors. Also, an atom that is part of a step edge is immobile, and will never be able to detach itself from the step edge. In ES-barrier based simulations, pollutants are absent.

The model presented above is similar to the diffusion model Jurdík *et al.* judged the most realistic [11]. However, we do not allow for diffusion processes that reduce the number of nearest neighbors. This means that, contrary to the model used in Ref. [11], the diffusion process is self-terminating, and the resulting structures will be permanent. For the case of Cr, the structures do indeed remain intact for months or even years after deposition.

The key assumption in the pollutant model is that pollutant species exhibit no surface diffusion whatsoever. This extreme assumption is appropriate if the pollutant hopping rate is much smaller than that of the lithographically deposited atoms. For oxygen adatoms, there are several experiments that indicate near-total surface immobility of adatoms [14, 15].

3 Simulation parameters

We will now proceed to choose our parameters, being the atomic beam flux density profile, the pollutant flux density, the deposition time, the hopping activation energy, and the ES-barrier energy.

The atomic beam flux density profile is assumed to be a Lorentz distribution on top of a homogeneous background, with a width equal to the values calculated by Anderson *et al.* We choose the contrast ratio (peak height to homogeneous background level) to be 3.5; our own simulations of focusing find that this is a reasonable value in many cases. From the experimental data given by Anderson *et al.* [9], we deduce that the spatially averaged beam flux density was around 0.05 ML/s (1 ML = $1.21 \times 10^{19} \text{ m}^{-2}$). The deposition time is set at five minutes, as in the Anderson experiment. The incoming flux distribution FWHM remains fixed at 20 nm when other parameters are varied.

The diffusion activation energy E_d is the only free parameter in Eq. 8.1, and its absolute value is unknown: the surface diffusion activation energy for Cr has never been investigated experimentally. Only one calculation of its value is known to the authors; Schindler [16] calculates a value of 0.22 eV for Cr[110]. In the same work, he also finds values of 0.28 eV for Fe[110] and 0.47 eV for W[110]. Experimental values for these systems are 0.225 eV and 0.87 eV, respectively. For other crystal faces, the diffusion energies of Fe are consistently higher than those on the [110] face. We conclude that for the structures under consideration, which are most likely polycrystalline, the calculated value of 0.22 eV should be taken as a lower limit. We choose to perform the simulations using an effective hopping activation energy $E_d = 0.30 \text{ eV}$.

We assume that the pollutant flux is constant and homogenous. We first make a rudimentary estimate of the amount of pollution needed to explain the experimental observations. The experimental structures are broadened by 20-30 nm with respect to the incoming atom flux distribution. Per structure flank, the broadening is 10-15 nm, or 35-50 sites. For a pollutant diffusion barrier, the distance to the nearest pollutant adatom should be on the order of the diffusion length. The corresponding amount of pollution is thus one in 35-50, or 2-3 %. In the absence of pollution, the diffusion length has no fundamental limit. Thus, the influence of a small amount of pollutants on the shape of the structures deposited could be immense.

The vacuum system was ion-pumped to a pressure of around 10^{-8} mbar [9], which corresponds to a molecular background flux of around $2.5 \times 10^{-3} \text{ ML/s}$. The composition of the background gas is unknown. Literature indicates that the sticking chance of oxygen on Cr is close to unity [17]. For nitrogen, the sticking coefficient is similar [18]. Any water present can be assumed to stick as readily, and will therefore also contribute O- or OH-groups to the surface. As there are at most two atoms per molecule for these gases, we expect to find an effective chemically bonding pollutant flux of up to $5 \times 10^{-3} \text{ ML/s}$. The estimate above results in a pollutant flux of 1×10^{-3} to $1.5 \times 10^{-3} \text{ ML/s}$, well within this range. The model value will be determined from the simulations.

The height of the ES-barrier also has never been determined experimentally for

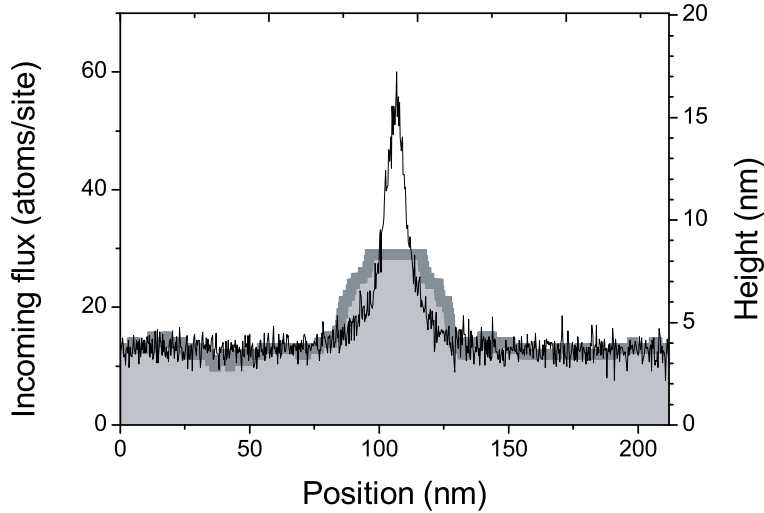


Figure 8.3: Sample simulation results. Line: incoming flux distribution (10 nm FWHM); average of five runs. Filled curve: calculated diffusion-broadened structure (34 nm FWHM); single run.

Cr. However, for Fe/Fe[100], a value of 0.04 ± 0.01 eV was found [19], and for Al/Al[111] 0.07 ± 0.01 eV was found [20]. For Al, values ranging from 0.04 eV to 0.83 eV have been calculated [21]. Comparing these values to the normal hopping energies, 0.454 eV for Fe[100] and 0.04 eV for Al[111], we find that the ES-barrier is very small compared to the hopping energy for Fe, but at least comparable for Al. Given that we assume a hopping energy of 0.3 eV for Cr, we vary the ES-barrier from 0 eV to 0.3 eV.

4 Pollutant limited surface diffusion

In this section, we investigate the results of the simulations under the assumption that $E_{ES} = 0$ eV. Thus, the only effect limiting surface diffusion is the presence of pollutant adatoms. Before investigating the dependencies of this model, we look at the structures it predicts. Figure 8.3 displays a sample incoming flux distribution and its resulting structure. To reduce statistical noise, we averaged five simulation runs for the flux distribution. The incoming beam flux distribution with a width of 10 nm is transformed into a structure with a full width at half maximum (FWHM) of 34 nm. The height of the structure is also comparable to that found experimentally. As can be seen the structure becomes broader and lower than that in the atom flux distribution, whilst the level of the background flux remains more or less the same. The top of the structure is a flat terrace; we attribute this to the fact that, in our model, atoms diffuse until they settle at a step edge. We conclude that diffusion primarily affects the shape of the structure. We find that the structure resembles the structures shown in experimental studies [9].

We analyze the structures by two figures of merit; the width of the structure

and its contrast. As the structures are not Lorentzian in shape, we determine their FWHM directly rather than from a curve fit. We define the contrast as the ratio of the height difference between the structure top and the background and the height difference between the background and substrate. We determine the background level by taking the average height of the leftmost 50 grid points. All structure widths and contrast ratios given from this point onwards are the averages of five simulation runs, and all error bars indicate standard deviations of these distributions.

Figure 8.4 shows the resulting structure FWHM and contrast as a function of effective pollutant flux. At low fluxes, diffusion clearly causes a lot of broadening. Also, the structure contrast is reduced strongly. These effects are very clearly suppressed by increasing pollution. The width of the structures found matches that found by Anderson *et al.* [9] for an effective pollutant flux of 2.0×10^{-3} ML/s. This is well within the range predicted in section 3, and close to the rough estimate in the introduction. We will use the value above throughout the remainder of this work. The pollution model has no further free parameters.

4.1 Atom flux

We can now proceed to compare the results of our model to the experimental investigations of Anderson *et al.* [9]. That comparison is displayed at the bottom of Fig. 8.5. The data points have been taken directly from their paper, and have been plotted with the simulation results. We find very reasonable agreement between the experiments and our simulations, with the two being within two standard deviations of each other at all instances. Also shown is the incoming atom flux (dashed lines). The diffusive broadening appears to be constant. This confirms our model of atoms that can diffuse for a certain length until they encounter a pollutant atom. The contrast of these structures is shown in the top half of Fig. 8.5. As can be seen, it increases with increasing structure width. This supports our earlier conclusion that the background height is not enhanced by the diffusion processes, but that instead the peak area remains constant. The structure height then decreases as a result of the broadening.

Varying the atom flux contrast ratio, we found no effect on the resulting structure widths; however, we did find that a greater atom flux contrast gives a greater structure contrast, as shown in Fig. 8.6. This, too, favors the notion of the structure being smeared out by diffusion more or less independently from the background.

4.2 Temperature

One peculiar experimental result was the lack of temperature dependence. The temperature dependence of the results from our model is shown in Fig. 8.7. For a hopping activation energy of 0.3 eV, we find no temperature dependence above 250 K. Below this temperature, we find that the diffusion is limited by the low hopping rate rather than by pollution. At higher temperatures, when the diffusion length of an atom is determined by the distance to the nearest pollutant adatom or molecule, diffusion becomes temperature independent. Lowering the activation energy lowers

BARRIER-LIMITED SURFACE DIFFUSION IN ATOM LITHOGRAPHY

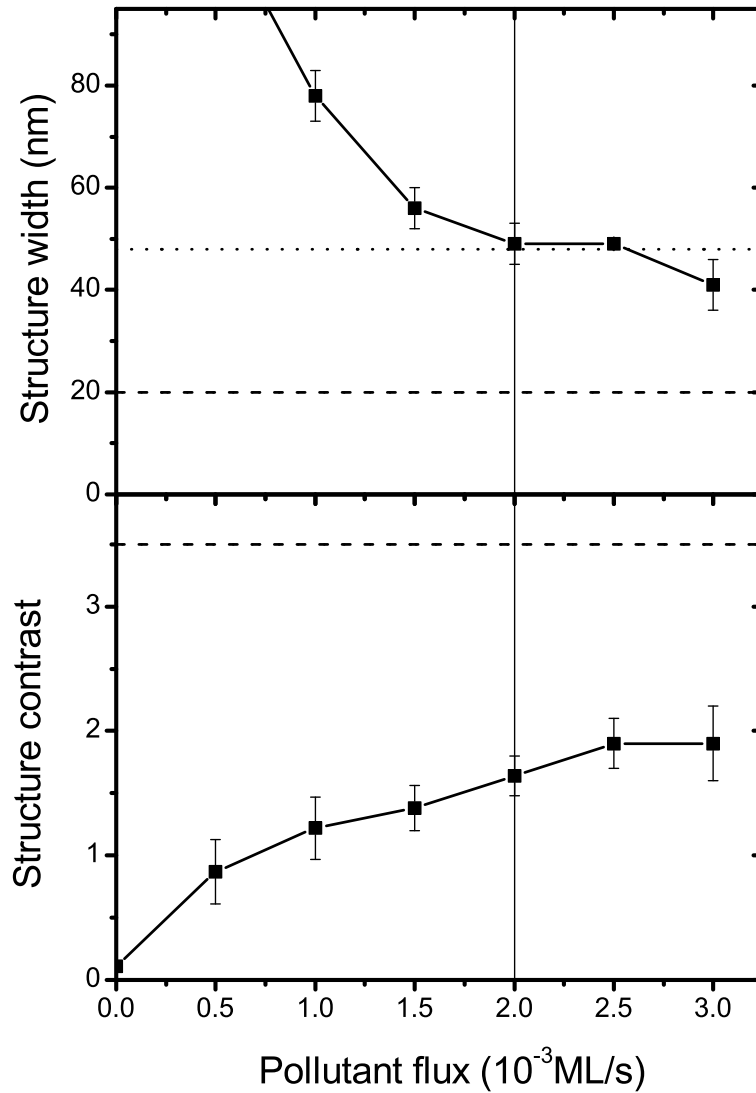


Figure 8.4: Dependence of structure FWHM (top) and contrast ratio (bottom) on effective pollutant flux. Average of 5 runs; error bars indicate standard deviation. Dashed lines indicate model input values, dotted line indicates experimental value. As pollutants suppress diffusion, they preserve structure contrast and narrowness. Vertical line indicates model value.

POLLUTANT LIMITED SURFACE DIFFUSION

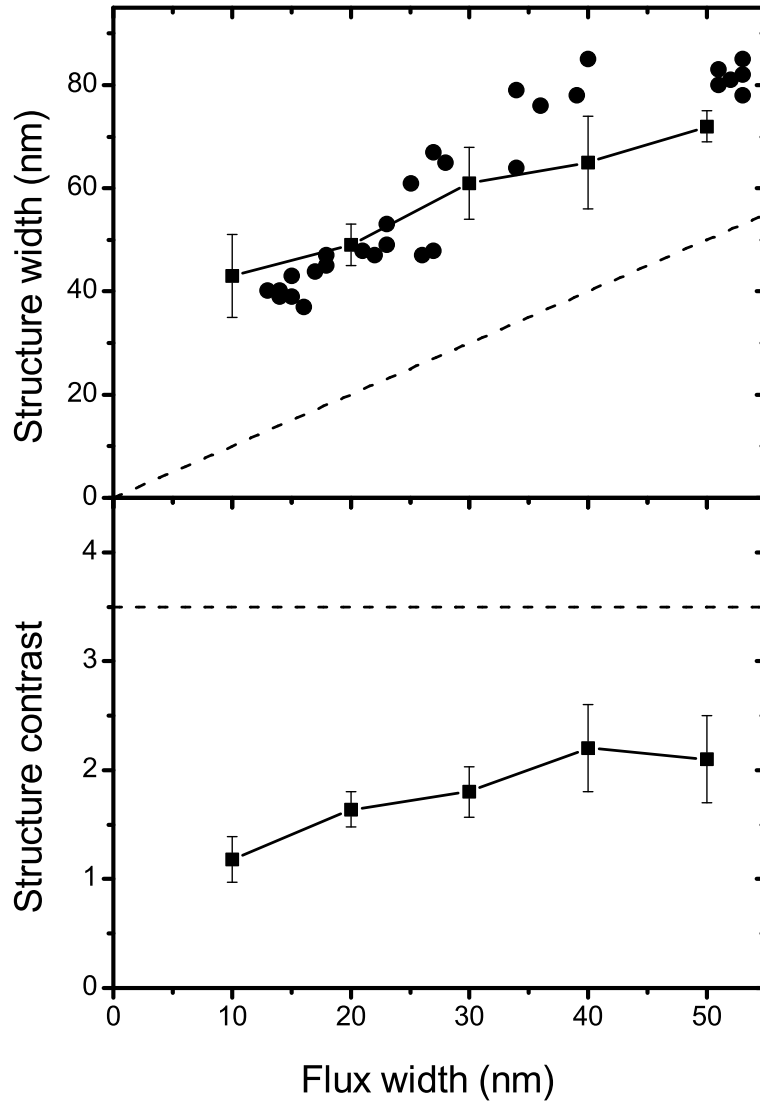


Figure 8.5: Bottom: comparison between simulated structure widths and experimental data (circles) for varying flux distribution width. Dashed line represents structure width equal to flux width. Top: simulated structure contrast for varying atom flux peak width. Dashed line indicates atomic flux contrast. Simulations are averages of 5 runs; error bars indicate standard deviations.

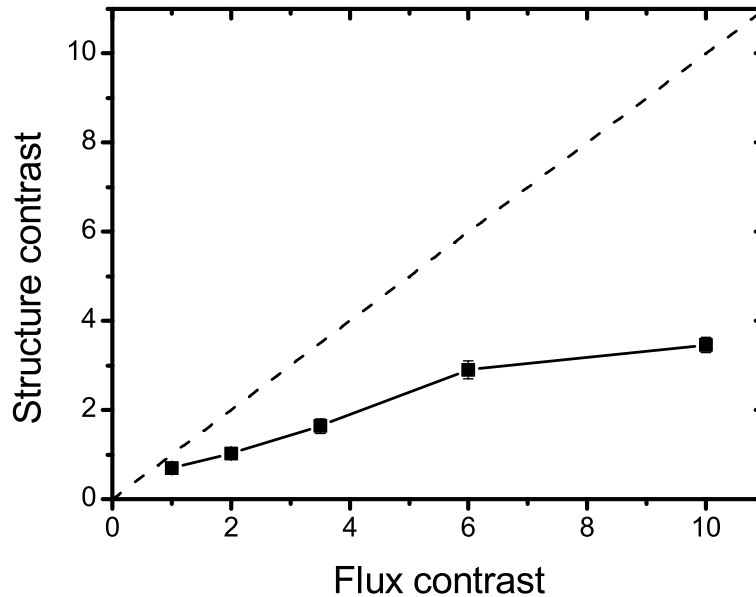


Figure 8.6: Influence of flux contrast on structure contrast. Dashed line: structure contrast equal to flux contrast.

the diffusion saturation temperature, as shown in Figure 8.7. As the range of temperatures investigated by Anderson *et al.* runs from 200 K to 350 K, we find that the effective diffusion barrier of Cr might be lower than we have assumed in this work. However, it is not a very critical parameter in our model. The other parameter from Eq. 8.1, R_0 , has no influence on the simulation results if varied by a factor of 10. Temperature affects structure contrast as little as expected: there is no effect on contrast as long as there is no effect on structure width. Only at low temperatures or high diffusion energies does the contrast increase towards the value of the atomic beam flux contrast. This is a logical result in the absence of diffusion.

4.3 Deposition duration

Finally, we investigate the dependence on deposition duration, which we also compare to the experimental data [9]. As shown in Fig. 8.8, the width of the experimental structures is large with a large uncertainty for very short depositions, after which the structures become rapidly narrower. At longer deposition times, the width of the structures increases slowly. Our simulations reproduce the initial increased width of the structures at least qualitatively. Simulation runs using a larger sample at short deposition times show that the increased scatter in structure widths is not a statistical fluke, but rather a consequence of increased scatter in the outcomes.

At longer deposition times, our simulations fail to reproduce the slow increase in structure width. We find three possible explanations for this. One reason is that the barrier to diffusion thrown up by the pollutants is too absolute in our simulations. By this we mean that in real, two-dimensional depositions, the presence of a pollutant does not mean an absolute barrier: an atom *could* diffuse around it. In our one-

POLLUTANT LIMITED SURFACE DIFFUSION

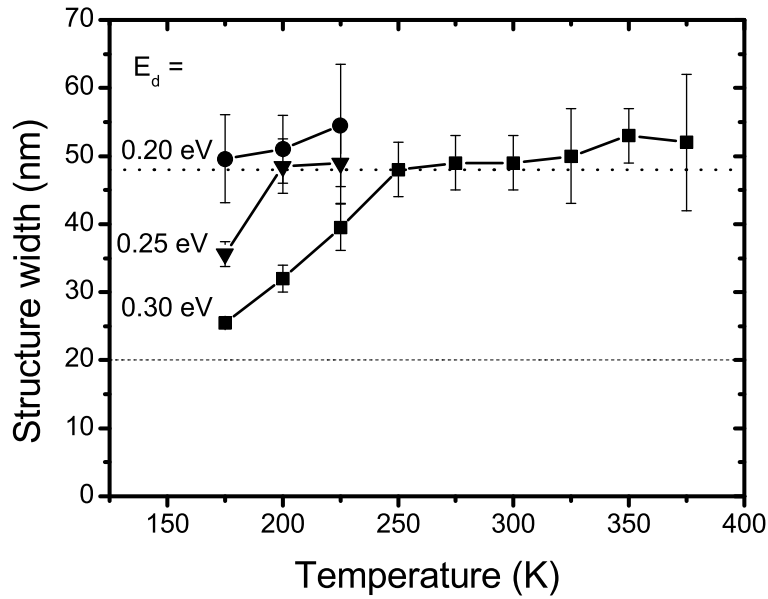


Figure 8.7: Temperature dependence of the resulting structures. Dotted line indicates experimental value, dashed line indicates flux distribution. Squares: simulated widths, $E_d = 0.3$ eV. Triangles: simulated widths, $E_d = 0.25$ eV. Circles: simulated widths, $E_d = 0.2$ eV. Temperature has no influence over a wide range.

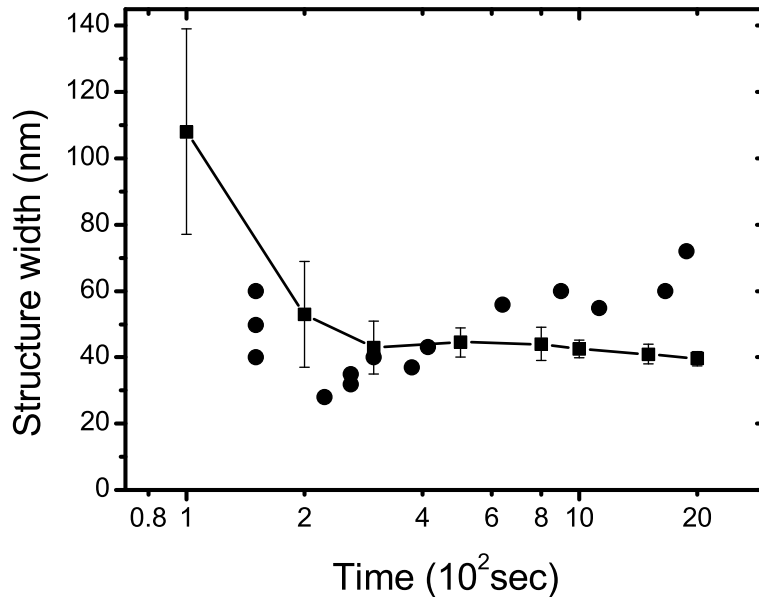


Figure 8.8: Structure width as a function of deposition duration. Line: simulations. Circles: experimental data. The slow increase in structure width at long deposition times is not reproduced, whereas the rapid decrease at short deposition times is.

dimensional simulated surface, there is no way around a pollutant at all. Second, there is also the possibility of thermal or other drifts of the substrate relative to the standing wave. The drift that would need to occur is something of the order of 10 nm over a mirror-to-line distance of around 2 mm. This means a relative length change of around 5×10^{-6} . If we attribute this to a thermal expansion of the Si substrate, the temperature drift needed is around 2 K. Note that structure width dependence on thermal drift is something different altogether from dependence on absolute temperature. A third effect could be that diffusion of the pollutant species is not completely absent, but just much slower. We deem this relatively unlikely, as it would require a very specific activation energy of pollutant diffusion.

5 ES-barrier limited surface diffusion

As in the previous section, we begin our investigation of ES barrier effects by looking at the structures predicted. Figure 8.9 displays four of the simulated structures for two different values of the ES barrier; $E_{ES} = 0.2$ eV at the top, and $E_{ES} = 0.09$ eV at the bottom. The biggest difference between the two is the marked increase in surface roughness at higher E_{ES} . This is an expected effect. As the ES barrier increases an atom's residence time on a terrace, islanding will occur on smaller terraces, leading to increased roughening. However, experimental investigations using a Scanning Electron Microscope (SEM) [22] show no roughness on that scale. This leads us to discount the possibility of a very high ES barrier.

The next step is to determine the absolute value of the ES barrier. The simulated structure widths at various values of E_{ES} are shown in Fig. 8.10. The FWHM of the structures was determined as in Sec. 4. At low E_{ES} , the structures are very broad, and they become narrower with increasing E_{ES} until a value of around 100 meV. At higher values of E_{ES} , the structures no longer become much narrower, but the spread in their FWHM increases dramatically. This is a side-effect of the increased surface roughness at high E_{ES} . Restricting ourselves to modest values of the ES barrier, we find the best agreement with experiment at a value of $E_{ES} = 0.09$ eV. We will use this value in all following simulations.

We now proceed to investigate the temperature dependence of the structures' width. Figure 8.11 shows the FWHM of the simulated structures as a function of temperature. The dependence of structure width on structure height is dramatic. At low temperatures, the ES barrier effectively appears to block nearly all diffusion. The resulting structures have widths similar to the width of the atom flux distribution. At higher temperatures, the width of the structures increases dramatically. This is in clear disagreement with the experimental findings of Anderson *et al.* [9]. We believe that this is natural, as crossing the ES barrier is a thermally activated process. We conclude that, although an ES barrier very probably does exist for Cr, its effect is not such that it can explain the experimental data.

ES-BARRIER LIMITED SURFACE DIFFUSION

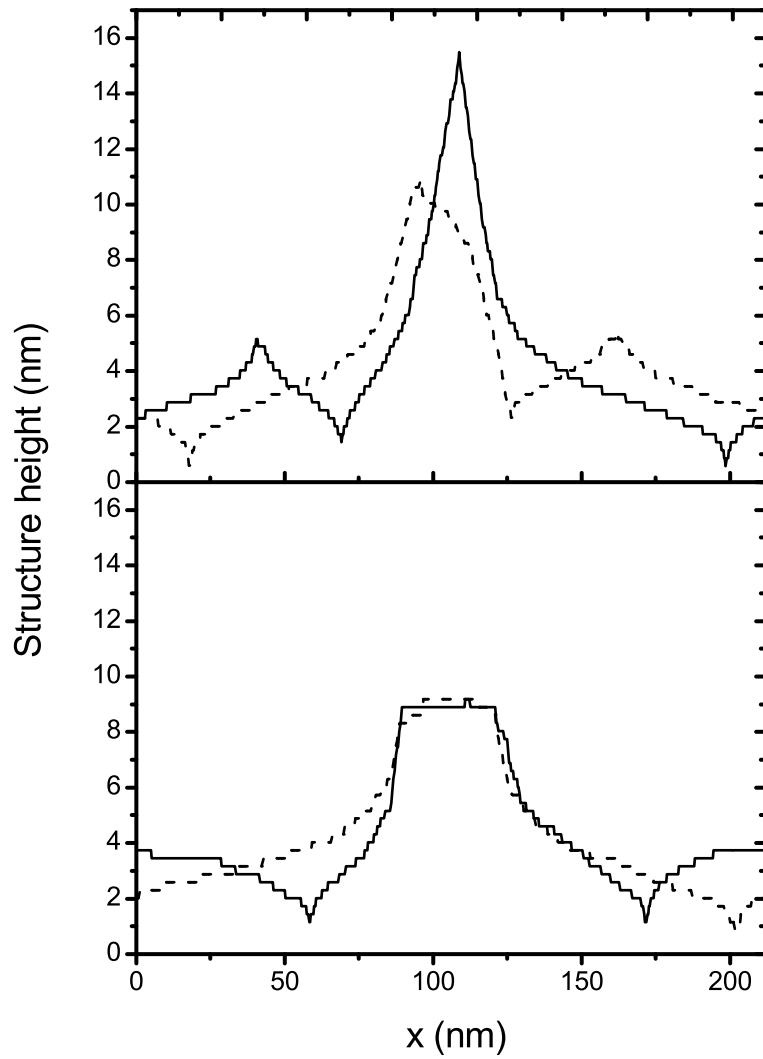


Figure 8.9: Simulated structures with Ehrlich-Schwoebel barrier. Top: two simulation runs with identical initial conditions; $E_{ES} = 0.2$ eV. Bottom: same, for $E_{ES} = 0.09$ eV. Note the increased surface roughness of the structures at high ES-barrier.

BARRIER-LIMITED SURFACE DIFFUSION IN ATOM LITHOGRAPHY

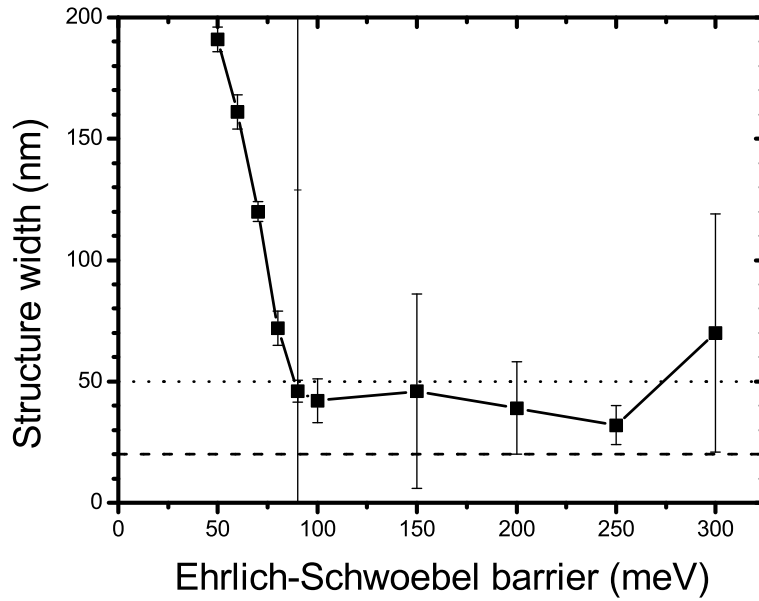


Figure 8.10: Simulated structure width as function of E_{ES} . Dashed line: atomic flux width. Dotted line: experimental structure width. The large spread in outcomes at high E_{ES} is due to increased surface roughening for a high ES barrier as seen in Fig. 8.9. Vertical line indicates model value.

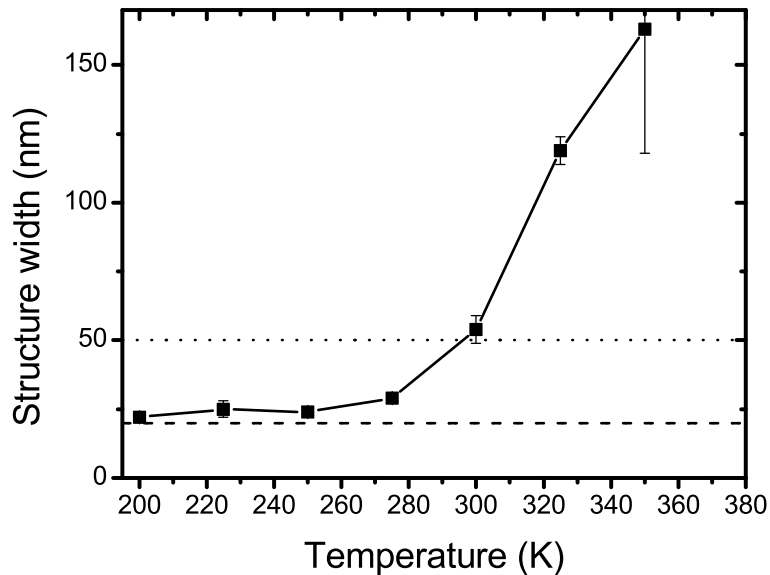


Figure 8.11: Temperature dependence of structure widths in the ES-barrier model. Symbols: simulation results. Dashed line: atomic flux width. Dotted line: experimental structure width.

6 Conclusions

We have modelled structure broadening by atomic diffusion in atom lithography. In our models, we have assumed that atomic diffusion occurs as a thermally activated process that is frustrated by some kind of barrier. We explore two different possible causes for this barrier. One mechanism is that pollutant adatoms from the vacuum background limit surface diffusion by posing a physical barrier. The alternative is that surface diffusion is limited by an ES barrier that is inherent in surface diffusion. We have performed KMC simulations of both limiting mechanisms.

The results of the pollutant-based simulation match the experimental results [9] very well. The barrier imposed by the pollutant species effectively suppresses the temperature dependence of the structure broadening. The only incongruence between our model and the experimental results is in the deposition time dependence of the structure widths. At longer deposition times, our model fails to predict the observed increase in structure broadening. This could be due to the one-dimensional nature of our simulations or to experimental drifts. A third possibility is that it is due to one of the many possible diffusion processes we have neglected. The ES-barrier utterly fails to reproduce the experimental lack of temperature dependence, and hence we believe that it is not the dominant factor in surface diffusion of Cr.

The veracity of the claims we make here would be interesting to test experimentally. This would not be very difficult as all one has to do is to introduce a controlled leak in the deposition vacuum. Furthermore, the pollutant barrier might be exploited to tune structure widths in atom lithography. The diffusion model could be further refined by the inclusion of several slower diffusion processes, such as, for instance, step edge detachment and pollutant adatom diffusion.

This work is financially supported by the Dutch Foundation for Fundamental Research on Matter (FOM). We wish to thank M. K. Oberthaler and D. Jürgens for useful discussions.

References

- [1] H. Metcalf and P. van der Straten, *Laser Cooling and Trapping* (Springer, New York, 1999)
- [2] D. Meschede and H. Metcalf, *J. Phys. D: Appl. Phys.*, **36**, R17-R38 (2003)
- [3] Th. Schulze, T. Müther, D. Jürgens, B. Brezger, M. K. Oberthaler, T. Pfau, and J. Mlynek, *Appl. Phys. Lett.* **78**, 1781-1783 (2001)
- [4] R. E. Behringer, V. Natarajan, and G. Timp, *Appl. Phys. Lett.* **68**, 1034-1036 (1996)
- [5] G. Timp, R. E. Behringer, D. M. Tennant, J. E. Cunningham, M. Prentiss, and K. K. Berggren, *Phys. Rev. Lett.* **69**, 1636-1639 (1992)
- [6] J. J. McClelland, R. E. Scholten, E. C. Palm, and R. J. Celotta, *Science* **262**, 877 (1993)
- [7] R. W. McGowan, D. M. Giltner, and S. A. Lee, *Opt. Lett.* **20**, 2535-2537 (1995)

BARRIER-LIMITED SURFACE DIFFUSION IN ATOM LITHOGRAPHY

- [8] E. te Sligte, R. C. M. Bosch, B. Smeets, P. van der Straten, H. C. W. Beijerinck, and K. A. H. van Leeuwen, *Proc. Natl. Acad. Sci.* **99**, 6509-6513 (2002)
- [9] W. R. Anderson, C. C. Bradley, J. J. McClelland, and R. J. Celotta, *Phys. Rev. A* **59**, 2476-2485 (1999)
- [10] R. E. Behringer, V. Natarajan, and G. Timp, *Appl. Surf. Sci.* **104/105**, 291-296 (1996)
- [11] E. Jurdík, Th. Rasing, H. van Kempen, C. C. Bradley, and J. J. McClelland, *Phys. Rev. B* **60**, 1543-1546 (1999)
- [12] R. M. Bradley, A. Eschmann, and S. A. Lee, *Journ. Appl. Phys.* **88**, 3316-3322 (2000)
- [13] A. Pimpinelli and J. Villain, *Physics of Crystal Growth*, Cambridge University Press, Cambridge (1998)
- [14] H. Brune, J. Wintterlin, R. J. Behm, and G. Ertl, *Phys. Rev. Lett.* **68**, 624-626 (1992)
- [15] R. X. Ynzunza, R. Denecke, F. J. Palomares, J. Morais, E. D. Tober, Z. Wang, F. J. García de Abajo, J. Liesegang, Z. Hussain, M. A. van Hove, and C. S. Fadley, *Surf. Sci.* **459**, 69-92 (2000)
- [16] A. C. Schindler, PhD thesis, Gerhard-Mercator-Universität, Duisburg (1999)
- [17] G. Gewinner, J. C. Peruchetti, A. Jaegle, and A. Kalt, *Surf. Sci.* **78**, 439-458 (1978)
- [18] J. E. Simpkins and P. Mioduszewski, *J. Vac. Sci. Tech.* **20**, 1321 (1982)
- [19] J. G. Amar and F. Family, *Thin Solid Films* **272**, 208-222 (1996)
- [20] R. Stumpf and M. Scheffler, *Phys. Rev. Lett.* **72**, 254-257 (1993)
- [21] S. J. Liu, H. Huang, and C. H. Woo, *Appl. Phys. Lett.*, **80**, 3295-3297 (2002); M. G. Lagally and Z. Zhang, *Nature*, **417**, 907-908 (2002)
- [22] J. J. McClelland, R. Gupta, Z. J. Jabbour, and R. J. Celotta, *Aust. J. Phys.*, **49** 555-565 (1996)

SUMMARY

Summary

Atom lithography is a technique in which a light field is used to pattern an atomic beam. This patterned flux is then deposited onto a substrate, resulting in a nanostructured thin film. The smallest structures that have been made thus far using this technique are around 30 nm wide. This thesis investigates the technique, expanding its possibilities.

The work-horse for the development of atom lithography has been Cr, as this transition metal atom has a closed transition in a wavelength range that is accessible to dye lasers. We extend the technique to Fe, the first ferromagnetic element to be used for atom lithography. The setup that was used to do this experiment is described, along with its critical design parameters.

We present nanostructures that are typically 50 nm wide, and up to 4 nm high. The spacing between the nanolines is 186.05 nm. The nanostructure profile is compared to that of a simulated deposition process, and found to match. To the authors' knowledge, this is the first demonstration of direct write atom lithography without laser cooling.

A preliminary incursion into the magnetic properties of the nanostructures deposited is presented. In addition to giving an overview of the general ferromagnetic properties that might be expected, a deeper investigation of the magnetic anisotropy of the nanostructures deposited in this experiment is given.

Novel resonant light masks are used in an experiment performed at the University of Konstanz (Germany). These light masks, using exactly instead of nearly resonant light, reveal some intriguing quantum mechanical effects. The most important of these features is the possibility to place structures closer together - at quarter wavelength spacings rather than half-wavelength intervals.

Finally, the influence of surface diffusion on the structures obtained in an atom lithography experiment is investigated using kinetic Monte Carlo simulations. Several diffusion limiting effects are investigated; the influence of small amounts of residual reactive background gas is found to describe the experimental observations.

Samenvatting

Atoomlithografie is een techniek waarbij een lichtveld wordt gebruikt om een patroon aan te brengen in een atoombundel. Deze gemoduleerde flux slaat vervolgens neer op een substraat; het resultaat is een genanostructureerde dunne film. De kleinste structuren die tot nu toe op deze wijze zijn gemaakt zijn lijntjes van 30 nm breed. In dit proefschrift wordt deze experimentele techniek onderzocht en haar mogelijkheden uitgebreid.

Het werkpaard in de ontwikkeling van de atoomlithografie is tot nu toe Cr geweest, een overgangsmetaal waarvan de atomen een gesloten overgang hebben in een golflengtebereik dat voor dye-lasers toegankelijk is. Wij breiden de techniek uit naar Fe, het eerste ferromagnetische element dat voor atoomlithografie gebruikt wordt. De opstelling die voor dit experiment is gebruikt wordt beschreven, met de kritieke ontwerp-parameters.

Als experimenteel resultaat worden nanolijnen getoond die typisch 50 nm breed zijn, en tot 4 nm hoog. De periode van de structuren is 186.05 nm. Het profiel van de structuren wordt vergeleken met dat wat voortkomt uit een simulatie van het depositieproces; beiden stemmen overeen. Voor zover op dit moment aan de auteur bekend is dit de eerste toepassing van depositie-atoomlithografie zonder laserkoeling.

Een eerste theoretische verkenning van de magnetische eigenschappen van de nanostructuren wordt gepresenteerd. Naast een overzicht van de algemene ferromagnetische eigenschappen die verwacht kunnen worden, wordt ook een dieper onderzoek naar de magnetische anisotropie van de nanostructuren uit dit experiment gegeven.

Vernieuwende lichtmaskers worden gebruikt in een experiment dat is uitgevoerd aan de Universiteit van Konstanz (Duitsland). Deze lichtmaskers, met exact resonant in plaats van bijna resonant licht, brengen enkele fascinerende quantummechanische effecten aan het licht. Het belangrijkste effect is dat het hierdoor mogelijk wordt structuren dichter bij elkaar te plaatsen – met een periode van een kwart golflengte in plaats van een halve golflengte.

Tenslotte wordt de invloed van oppervlaktediffusie op de structuren onderzocht met behulp van kinetische Monte Carlo simulaties. Verschillende diffusie-effecten worden onderzocht; de invloed van kleine hoeveelheden reactief achtergrondgas blijkt de experimentele observaties te beschrijven.

DANKWOORD

Dankwoord

Hoewel een proefschrift veel eenzame arbeid vereist, heb ik bij de totstandkoming ervan ook veel gehad aan anderen; hen wil ik hier graag bedanken.

In de eerste plaats natuurlijk mijn eerste promotor Ton van Leeuwen, voor ontelbare commentaren, tips en adviezen, en natuurlijk de ontdekking van Sambal Badjak. Daarnaast mijn tweede promotor Herman Beijerinck, zonder wie ik waarschijnlijk nooit aan dit project zou zijn begonnen, en zonder wiens noodgedwongen inzet ik misschien ook niet op tijd de eindstreep zou hebben gehaald.

In het lab ben ik mijn collega Bart Smeets veel dank verschuldigd; voor een belangrijk deel dankzij zijn soms haast magische verstandhouding met de laser bevat dit proefschrift ook experimentele resultaten. Ook afstudeerders Richard van der Stam en Rodolf Herfst zijn van grote waarde geweest. Met Roel Bosch heb ik in mijn eerste half jaar nog zeer prettig gewerkt aan een destijds zeer frustrerende opstelling. De technische ondersteuning van Louis van Moll en Jolanda van de Ven is vier jaar lang telkens weer van onschatbare waarde gebleken. Mijn collega's in de groep wil ik graag bedanken voor de goeie werksfeer.

I would also like to thank everybody I worked with at the University of Konstanz for a splendid time. Especially, I would like to thank Dirk Jürgens and Markus Oberthaler for a fruitful, interesting, and very friendly cooperation.

Tenslotte ben ik Sigrid erg dankbaar voor haar morele steun, warmte en hulpvaardigheid, vooral op onmogelijke en/of onverwachte tijdstippen.

DANKWOORD

Curriculum Vitae

- 3 september 1977 Geboren te Gouda
- 1988-1994 Gymnasium,
Lorentz Lyceum te Eindhoven
- 1994-2001 Studie Technische Natuurkunde,
Technische Universiteit Eindhoven,
doctoraal examen april 2001.
- 2001-2005 Assistent-In-Opleiding,
Experimentele Atoomfysica en Quantumelektronica,
Faculteit Technische Natuurkunde,
Technische Universiteit Eindhoven